AMRA CR 67-05(F)

INTERACTION OF PROJECTILES AND COMPOSITE ARMOR

FINAL REPORT

by

A. L. FLORENCE AND T. J. AHRENS

JANUARY 31, 1967

STANFORD RESEARCH INSTITUTE
MENLO PARK, CALIFORNIA 94025

CONTRACT DA-04-200-AMC-1381(X)

U. S. ARMY MATERIALS RESEARCH AGENCY
WATERTOWN, MASSACHUSETTS 02172

INTERACTION OF PROJECTILES AND COMPOSITE ARMOR

AMRA CR 67-05(F)

by

A. L. FLORENCE AND T. J. AHRENS

JANUARY 31, 1967

STANFORD RESEARCH INSTITUTE

MENLO PARK, CALIFORNIA 94025

SRI PROJECT FGU-5766

CONTRACT DA-04-200-AMC-1361(X)

D/A PROJECT 1C024401A110

AMCS CODE 5011-11-855

U. S. ARMY MATERIALS RESEARCH AGENCY
WATERTOWN, MASSACHUSETTS 02172

ACKNOWLEDGMENTS

The authors are indebted to K. Schreiner and W. A. Zietzke for helping to conceive the experimental program on impact and for performing the experiments, to J. T. Rosenberg for performing the experiments on dynamic properties of aluminum oxide, to P. S. DeCarli for contributing the work on the microscopic examination of fractured ceramic, to B. B. Bain for computer programming and for providing Figs. 37 through 47, and to G. R. Abrahamson for helpful advice and constructive criticism.

ABSTRACT

This report describes basic experimental and theoretical work on the interaction of projectiles and lightweight composite armor. The armor of interest consists of a very hard and inflexible facing plate (ceramic) bonded to a flexible backing plate (fiber glass). Attention has been focused on the mechanism of interaction between a facing plate and a hard projectile (steel).

Experimental results consist of high speed camera photographs of the projectile-armor interaction and observations of the final state of the projectile and armor. Theoretical analyses, based on the theory of elasticity, were used to establish stress fields in the facing plate during the initial stages of impact and to determine deflections and bending moments during the later stages. In addition to this work on the mechanics of projectile-armor interaction, exploratory experiments were undertaken with a view toward establishing the dynamic mechanical properties of aluminum oxide, an important facing material.

On the basis of these experimental observations and theoretical predictions, the following sequence of events occurs when a hard steel projectile strikes composite armor having a ceramic facing plate:

1. The tip of the projectile is shattered into many very small (1 mm) fragments. This occurs because, due to the proximity of the steel free surface, tensile stresses greatly exceeding the fracture stress are immediately set up at the tip. The remainder of the steel projectile fractures into a few pieces (the largest being the rear portion) which remain together during penetration of the facing plate.

2. Comminution and fine cracking of the ceramic facing material spreads from the impact zone due to an expanding hemispherical field of large tensile stresses; this field follows a compressive wave front and has a strong "hydrostatic" tensile behavior. Ceramic powder is ejected from the region around the bullet.

3. Cracking at the face opposite to the impact zone develops rapidly. This cracking is predominantly radial, because the expanding tensile stress field has large circumferential stress components leading other stress components.

4. Density of cracking decreases away from the impact zone, due to attenuation of the tensile stress field.

5. A membrane, or stretching action of the flexible backing plate restrains the central region of crushed ceramic and fragmented projectile.

General conclusions at this stage of the investigation are:

1. High speed photography can be used effectively to gain a qualitative understanding of the interaction of projectiles and composite armor.

2. Theoretical models based entirely on elastic response predict stress and bending moment distributions compatible with the fracture patterns observed in ceramic facing plates.

3. Aluminum oxide has a fracture stress which increases significantly with rate of strain and the material behaves elastically at stresses below the fracture stress.

Future research should provide for the determination of dynamic mechanical properties of ceramics and incorporation of these properties into a theoretical model. This information is needed because of the high sensitivity of the fracture stress to strain rate. Future research should also include a study of the interaction of the stress fields caused by fracture with the environmental stress fields. This interaction, not taken into account in the present work, may be significant.

CONTENTS

CONTENTS (Concluded)

ILLUSTRATIONS

ILLUSTRATIONS (Continued)

ILLUSTRATIONS (Continued)

ILLUSTRATIONS (Concluded)

TABLES

1. INTRODUCTION

Over the years the improvement of armor has been achieved primarily through standard empirical evaluation tests. Still lacking is an adequate understanding of the mechanics of projectile and armor interaction and their dependence on material and geometrical properties. The need for lightweight armor has led to evaluation of ceramic materials, such as alumina and boron carbide, for use as facing in composite armor. This unusual application creates a need for experimental work to determine the properties of ceramics at high pressures and high strain rates. These two main problem areas, mechanics of interaction and material properties, are interrelated but can be treated separately.

This report describes an experimental and theoretical investigation of the interaction of projectiles and lightweight composite armor consisting of a very hard, inflexible, facing plate of 0.34-inch-thick ceramic bonded to a flexible backing plate of 0.25-inch-thick fiber glass. The ultimate objectives of this investigation are to describe the mechanisms of the interaction and to determine their dependence on material and geometrical properties. Most of the work concerns the interaction of projectiles with facing plates only (without backing), but experiments are included which show the response of composites. Experiments to determine material properties at high pressures and high strain rates of a form of alumina are also included.

In the experimental program high-speed photography and terminal observations were used to study the projectile/armor interaction. Work has focussed on hard steel projectiles at low (120 ft/sec) and high (1800 ft/sec and 2400 ft/sec) velocities impacting facing plates of ceramic or glass with backing plates of fiber glass or Micarta. Glass was used because it is transparent and brittle; Micarta was used because it is flexible and readily available. Theoretical analyses based on elastic behavior were carried out to obtain the transient stress fields in the projectile and facing plate.

Section 2 discusses the stress waves and structural response concepts underlying the approach to the interaction problems. Impact experiments are described in Section 3 and the results and observations are contained in Section 4. The theoretical treatments are presented in Section 5 and numerical results corresponding to the experiments of Section 4 appear in Section 6. Section 7 contains a discussion and the conclusions that seem most reasonable at the present state of the investigation. Section 8 covers the experiments which describe the dynamic yielding of aluminum oxide. Finally, Section 9 contains remarks about the fracture of aluminum oxide based on a few petrographic observations.

2. MECHANICS CONCEPTS

The response of a facing material to projectile impact may be regarded in two ways. In the first, the facing material is considered as a layer through which axisymmetric stress waves emanating from the impact zone are traveling, with reflections occurring at the top and bottom surfaces (see Fig. 1). This "stress-wave response" concept is suitable for studying the early response of the armor and projectile (that is, for times less than about three or four transit times of the stress-wave front through the facing thickness).

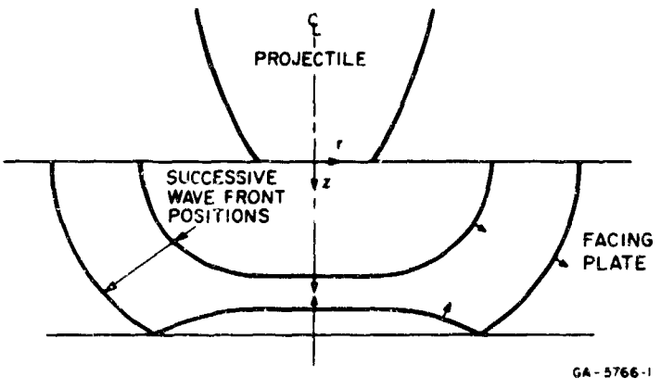

FIG. 1 STRESS-WAVE RESPONSE CONCEPT

The other concept is to consider that the facing material acts as a plate in which the stress field is represented by resultant shearing forces Q, and by resultant radial and circumferential components of bending moment M and N, as indicated in Fig. 2. This "structural response" concept is suitable for studying response after the stress-wave front has made many transits through the facing material.

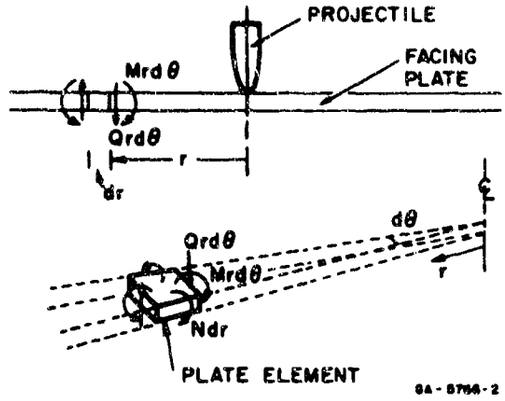

FIG. 2 STRUCTURAL RESPONSE CONCEPT

It is conceivable that, should the armor survive the initial stress-wave response, failure could occur by structural response. In general, both types of response are important for describing ways in which armor can fail. The stress-wave and structural response concepts form the bases of the two theoretical approaches described in Section 5. It is also helpful to keep the concepts in mind while examining the experimental results presented in Section 4.

3. DESCRIPTION OF IMPACT EXPERIMENTS

In the impact experiments, projectiles were launched at targets in a highly controlled manner and the impact event was recorded by high-speed photography. Impact velocities were either high (1500, 1800, or 2400 ft/sec) or low (less than 120 ft/sec); different projection techniques were used for these two velocity ranges. Table 1 lists the main experimental parameters.

A. Projection Techniques

1. High Impact Velocity

Figure 3 is a photograph of a typical experimental setup for providing a high impact velocity of a 0.458 caliber projectile with a target. The target in this case is a ceramic tile. The projectile is fired from the small, sturdy gun shown in the photograph. Except for the bore diameter of the gun, the experimental setup is exactly the same for 0.3 caliber projectiles.

Referring to Fig. 4, which shows the gun in more detail, the firing operation is as follows: the detonator (PL-II) is initiated and this in turn detonates the mild detonating fuze (MDF). When the detonation front reaches the end of the MDF inside the breech plug it thrusts a small steel ball against the cartridge cap; the ball thus acts as a firing pin. Upon initiation of the rifle powder the steel ball is thrown back and acts as a valve to prevent the release of pressure in the chamber.

This method of firing was devised to minimize the period from the start of the event (initiation of the PL-II) to the bullet-target impact. Also with this aim in mind, the barrel is short to reduce the length of bullet travel (with some sacrifice in velocity) and the breech block is thick to withstand high pressures. To improve reproducibility the cartridge cases were carefully hand-filled with a weighed quantity of rifle powder. This projection technique provides adequate reproducibility to allow synchronization of the event and the recording period of the high-speed framing camera.

Table 1

MAIN EXPERIMENTAL PARAMETERS

PROJECTILE					TARGET			Figure Numbers (Section 4)
Material	Caliber (inch)	Weight (gm)	Hardness (Knoop K_{100})	Velocity (ft/sec)	Material	Dimensions (inches)	Hardness (Knoop K_{100})	
Steel	0.458 AP	24.6	700	1800	Ceramic AD94	0.34 x 6.0 x 6.0	2000	7,8,9,10
					Ceramic AD94 Fiber glass (Doron)	0.34 x 6.0 x 6.0 0.25 x 9.0 x 9.0	2000	11,12
					Glass	1.25 x 5.875 x 5.875	600	15,16,17,18
Steel (Lead)	0.458 ball	32.5	200	1500	Glass	1.25 x 5.875 x 5.875	600	19
Steel (Copper-Lead)	0.3 AP	10.1	700	2400	Ceramic AD94	0.34 x 6.0 x 6.0	2000	20,21,22,23,24
					Ceramic AD94 Fiber glass (Doron)	0.34 x 6.0 x 6.0 0.25 x 9.0 x 9.0	2000	25,26,27
					Glass	1.25 x 5.875 x 5.875	600	28,29,30
Steel	0.5 ball	12.0	350	94	Glass	1.25 x 5.875 x 5.875		31,32
		23.2	350	80	Glass-Micarta	0.25 x 12 diameter		33
		23.2	350	54	Glass	0.25 x 12 diameter		34

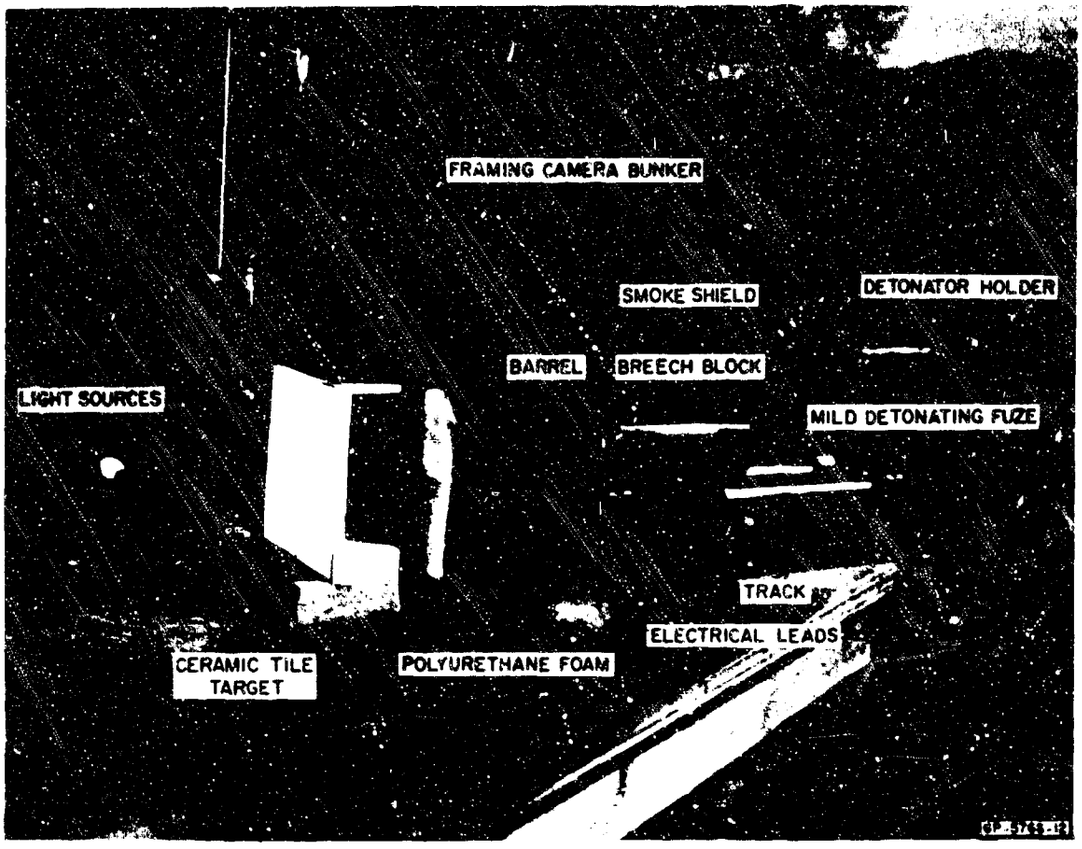

FIG. 3 EXPERIMENTAL ARRANGEMENT FOR HIGH VELOCITY IMPACTS

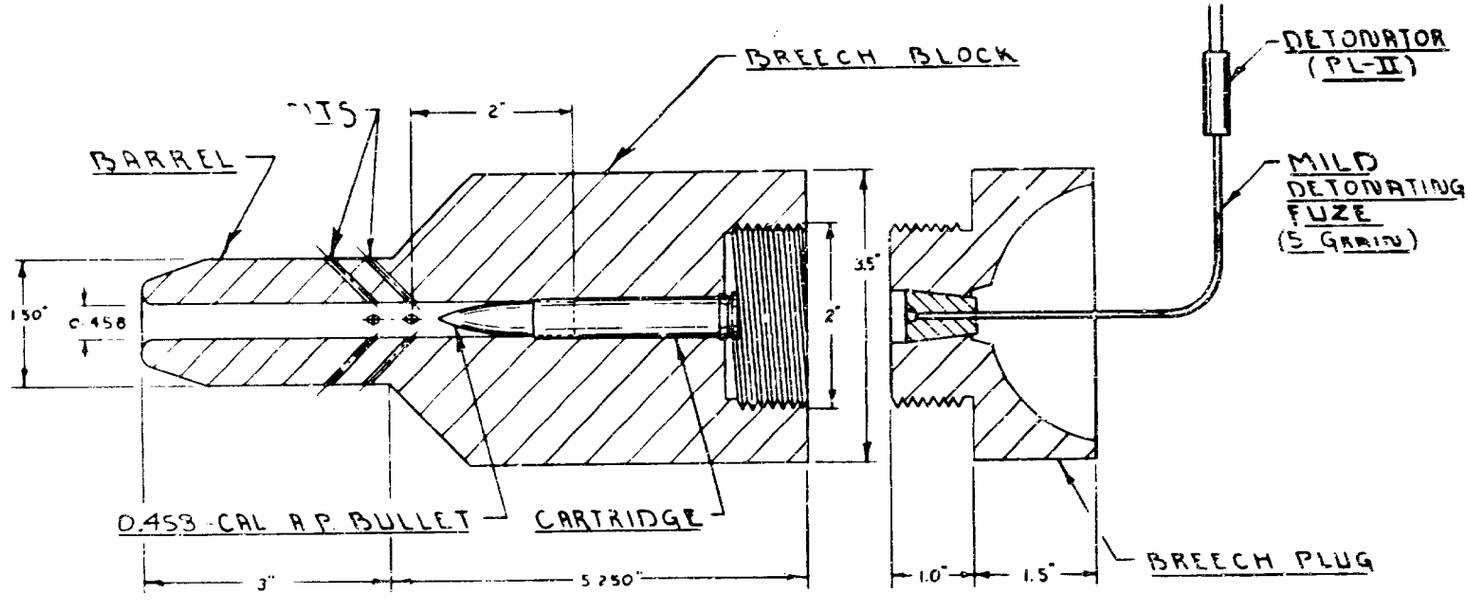

FIG. 4 0.458 CALIBER GUN

As a typical example, the time from detonation of the PL-II to impact was about 1000 μsec for a projectile weighing 24.6 gm that acquired a velocity of 1800 ft/sec when launched with a 3.2 gm of rifle powder.* Since the reproducibility turned out to be better than ±2%, the maximum variation in the time at impact was less than ±20 μsec. The recording time for the 25 frames of the camera was typically 100 μsec, so that it was always possible to obtain more than 60 μsec of good recording time, or about 15 frames.

2. Low Impact Velocity

The technique described above is not suitable for launching small projectiles at low velocities. Figure 5 shows a device (essentially the Hopkinson's bar) which is suitable provided sufficient care is taken in its construction and operation. It consists of a 1/2-inch-diameter steel rod, about 6 inches long, with a small steel ball-nosed extension or spall piece also 1/2 inch in diameter. Two ball-nosed spall pieces are shown in Fig. 5; the shorter piece is shown in its firing position. The interface between the rod and spall piece is ground and lapped, a very important operation to ensure reproducibility. A small amount of explosive at the free end of the rod provides a short compressive pulse which, upon reflection from the opposite end, becomes tensile and projects the spall piece. Velocities up to 120 ft/sec were obtained with the 12-gm projectile. To reduce timing errors, the time from detonation to impact was minimized by giving the projectile only 1/16 inch of travel before it struck the target. The apparatus has a reproducibility adequate for synchronization of the impact event with the recording period of the high speed framing camera.

B. Projectiles

Figure 6 shows the three types of projectiles used in the high impact velocity experiments. Additional details are given in Table 1. Most of the experiments with the 0.453 caliber projectiles were conducted

*DuPont S.R. 7625.

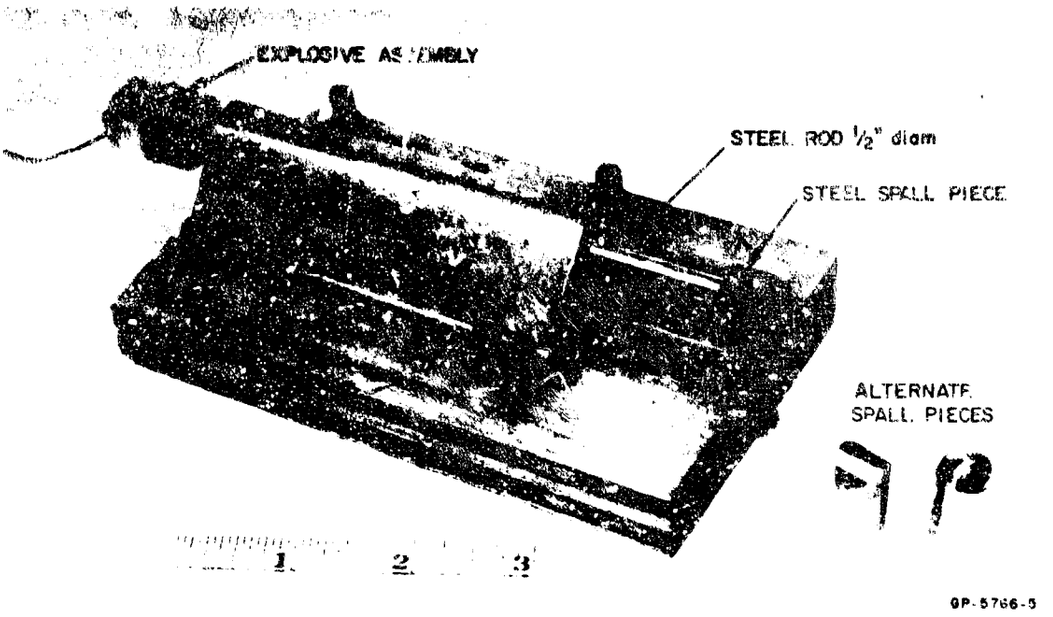

FIG. 5 HOPKINSON'S BAR FOR LOW IMPACT VELOCITIES

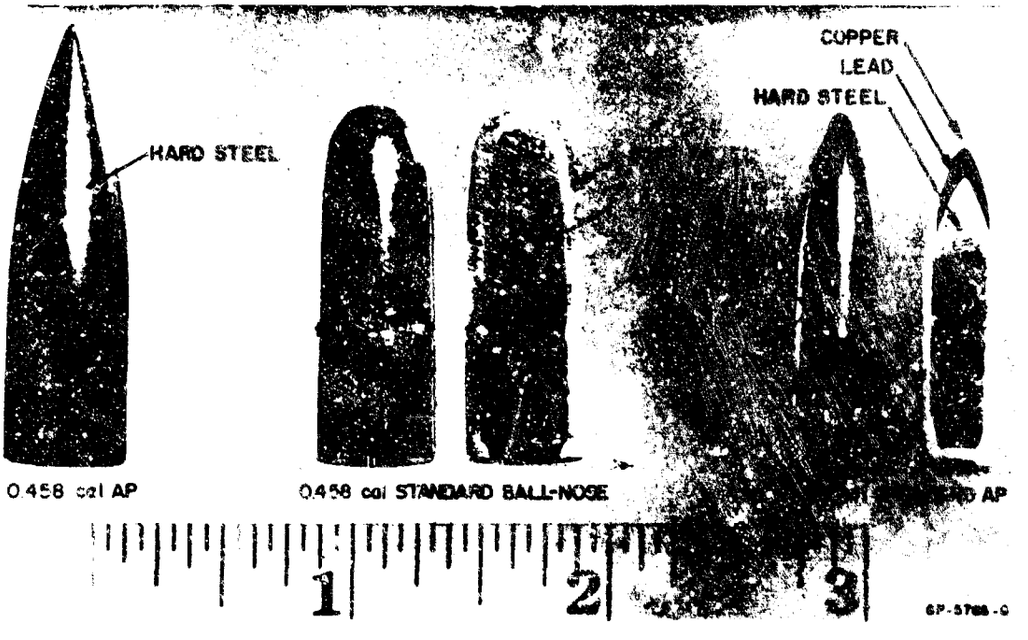

FIG. 6 TYPES OF PROJECTILES

with the armor-piercing (AP) type at a velocity of 1800 ft/sec. These bullets, weighing 24.6 gm, 1-11/16 inches long, and hardened* to 700 K_{100}, were specially manufactured without a jacket so that the behavior of hardened cores of standard AP bullets could be observed. A few experiments at impact velocities of 1500 ft/sec with standard ball-nosed 0.458 caliber bullets, weighing [illegible].5 gm and consisting of a soft steel shell filled with lead, were conducted for a general comparison of behavior of hard and soft bullets under impact. The third type of projectile used in the high impact velocity experiments is the 0.3 caliber standard AP bullet shown in Fig. 6. These bullets, weighing 10.1 gm, were fired at 2400 ft/sec and were included to allow realistic basic interactions to be compared with those of 0.458 caliber AP bullets.

The projectiles used for the low impact velocity experiments are the 1/2-inch-diameter steel ball-nosed spall pieces shown in Fig. 5. They are either 1/2 inch or 1 inch long, weighing 12.0 gm or 23.2 gm.

C. Targets

A summary description of the targets used is given in Table 1. The main types of target are:

1. Ceramic tiles† of isostatically pressed alumina (AD94) measuring 0.34 x 5-3/4 x 5-3/4 inches, of density 3.6 gm/cm^3 and hardness 2000 K_{100}.
2. Ceramic-fiber glass composites§ in which a ceramic facing plate of the kind described under Item 1 is bonded^Δ to a backing plate of fiber glass,# 0.25 inch thick.

---

*Hardness is given in terms of Knoop numbers. K_{100} means that a force of 100 gm is applied to the wedge-snaped diamond indent r.

†Manufactured by Coors Porcelain, Golden, Colorado.

§Supplied by AMRA, Watertown, Massachusetts.

^Δ With "Proseal," manufactured by Coast Proseal & Manufacture, Los Angeles, California.

#"Doron" manufactured by Russel Reinforced Plastics, Long Island, New York.

3. Glass blocks,* annealed and of high optical quality, measuring 1-1/4 x 5-7/8 x 5-7/8 inches (commonly used as protective windows), with a density of 2.49 gm/cm^3 and 600 K_{100} hardness.

4. Glass plates, 1/4-inch thick, 12 inches in diameter, glued† either to 1/2-inch-thick light polyurethane foam (5 lb/ft^3) or to 1/4-inch-thick Micarta plates.

Glass was introduced because, like the ceramic tiles, it is brittle, and unlike the ceramic, it has the advantageous property of transparency which makes it possible to observe the development of internal fracture fields by high speed photography. Micarta was used as a flexible backup plate for the glass facing plates because it is similar to fiber glass and was readily available. Experiments show that this composite is suitable for low impact velocity experiments.

D. Observation Methods

The impacts were observed by a Beckman and Whitley 189 high speed framing camera. The recording times most commonly used were 50, 100, and 200 μsec, which give 2.08, 4.17, and 8.33 μsec between each of the 25 frames. Terminal observations were always made.

*Obtained from Bienen and Field Glass Corporation, 1525 West 25th Street, Chicago, Illinois.

†RTV-102 Adhesive Sealant, manufactured by General Electric, Silicone Product Dept., Waterford, New York.

4. EXPERIMENTAL RESULTS AND OBSERVATIONS

Table 1 gives the principal experimental parameters of each experiment and the figure numbers of the corresponding records. The experiments are described below in the order given in Table 1.

A. 0.458 Caliber AP Bullet Impacting Ceramic Tile

Figure 7 shows a profile view of the sequence of events during an impact at 1800 ft/sec of a steel AP bullet of 700 K_{100} hardness with a ceramic tile (AD94) of 2000 K_{100} hardness. Initially, the sharp nose of the bullet shatters and steel particles up to 1 mm average diameter are sprayed radially across the surface of the ceramic tile at about double the bullet impact velocity (that is, at about 3600 ft/sec). The particles from the shattered tip were caught in styrofoam traps placed around the tile. Measurements of lengths in subsequent frames of Fig. 7 indicate that the bullet, originally 1-11/16 inches long, is shortened by at least 1/8 inch in less than 25 μsec from the start of impact. Little change in velocity of the rear of the bullet occurs until 25 μsec have elapsed. The first observable sign of tile break-up occurs 21 μsec after impact, long enough for the elastic dilatational wave front in the ceramic to travel 7.6 inches, or about 22 plate thicknesses. The break-up region at the rear face of the tile is confined to a circular area with a diameter about four times the full diameter of the bullet (that is, about 1-7/8 inches or about 5-1/2 times the tile thickness).

Figure 8 is an oblique view of the front face of a ceramic tile during an impact in an experiment which was a repeat of that shown in Fig. 7. The radial scattering of steel particles which form the bullet tip can be seen, followed by ejection of the crushed ceramic adjacent to the bullet.

Figure 9 is an oblique view of the rear surface of a ceramic tile during an impact in an experiment which was a repeat of those described by Figs. 7 and 8. The first observable signs of fracture occur as several radial cracks and one circumferential crack with a diameter about

four times the full diameter of the bullet, or about 1-7/8 inches. The record goes on to show breakup into some 12 pie-shaped pieces, or sectors, or ceramic which rotate about the circular crack, each sector ultimately breaking up into many small pieces. From the time of the initial breakup (Frame 4) finely crushed ceramic is present.

Figure 10 shows the bullet fragments retrieved from a sand trap located behind the ceramic tiles in four experiments of the kind depicted in Figs. 7, 8, and 9. Apart from nose shattering, this fragmentation cannot be seen in Fig. 7 and similar records; therefore the bullet, although considerably fractured, penetrates the tile essentially as one piece.

B. 0.458 Caliber AP Bullet Impacting Ceramic-Fiber Glass Composite

Figure 11 gives a profile view of the impact at 1800 ft/sec of a steel AP bullet with a specimen of composite armor consisting of a ceramic (AD94) facing tile 0.34 inch thick, backed by a 1/4-inch-thick plate of fiber glass (Doron). The early deformation of the flexible backing plate (after Frame 3) is localized to a circular area corresponding in size to the initial circular break-up region of the ceramic tiles shown in Figs. 7 and 9. The fiber glass plate restrains the ceramic by membrane action, as exhibited by its conical shape. The circular restraining region of the back-up plate spreads because the plate is sheared from the back surface of the facing plate. That this shearing action occurs can be deduced by comparing Fig. 11 with Figs. 7 and 9. Furthermore, terminal observations in experiments corresponding to that illustrated in Fig. 11 indicate that the plane of weakest shear resistance is usually not at the bond but at the layer of weaving adjacent to the bond.

Figure 12 shows the fracture pattern in the ceramic tile in the specimen of Fig. 11. The top surface has 10 radial vertical cracks which penetrate the entire thickness, and a circular crack 3 inches in diameter. Some of the relatively large pie-shaped pieces between this circular crack and a circle about 1 inch in diameter remain in place. At the bottom surface, in a central circular region about 2 inches in

diameter, there are over twice as many radial cracks as at the top surface. Also in this region is a tiered structure of ceramic with fracture surfaces sloping towards the impact point.

Figures 13 and 14 are front and rear surface views of another ceramic tile after impact. It was glued to a layer of low density, flexible polyurethane foam, 1/2-inch thick, which itself was glued to a Lucite plate. These experiments were designed to retain as many pieces of ceramic as possible in order to show the general fracture pattern. The top surface of the tile has 12 radial vertical cracks which penetrate the entire thickness and a circular crack 3 inches in diameter. The rear surface view, taken after removal of the foam and all small pieces of ceramic, shows the region of severe fracture.

C. 0.458 Caliber AP Bullet Impacting a Glass Block

Figure 15 shows the development of the fracture field in an annealed glass block measuring 1-1/4 x 5-7/8 x 5-7/8 inches and of hardness 600 K_{100} during impact at 1800 ft/sec with a 0.458 caliber bullet of hardness 700 K_{100}. The observable fracture field occupies an expanding hemispherical region with its front moving at 5200 ft/sec, about 0.3 times the dilatational velocity for the glass (taken as 19,000 ft/sec). In Frame 10, a reflected fracture field can be seen forming at the rear surface of the glass block at about 19 μsec after impact. This reflected field coalesces with the incident fracture field and together they spread throughout the block.

A repeat of this experiment, but with double the camera speed and different lighting, produced the records of Fig. 16. Again the velocity of the observable fracture front is 5200 ft/sec. The record shows a dark hemispherical region with a radius about one-half that of the fracture front. This dark region is interpreted as an expanding volume of pulverized glass.

Figure 17 is a framing camera record from a similar experiment in which the impact event was viewed through the rear surface of the glass block. The fracture field appears as an expanding area roughly circular in shape. This record, taken with those of Figs. 15 and 16, helps to form a three-dimensional mental picture of the fracture field.

Figure 18 shows the overall deformation or breakup of the glass block in an experiment similar to those in Figs. 15, 16, and 17. No appreciable displacement of the rear surface occurs until 42 μsec after impact (Frame 10). The dilatational wave front at this time has traveled about 2-1/2 inches and the estimated position of the bullet tip is 0.8 inch from the front surface. The bullet emerges from the glass block at a velocity of 1400 ft/sec.

In these experiments the bullet is always retrieved intact.

D. 0.458 Caliber Standard Ball-Nosed Bullet Impacting a Glass Block

Figure 19 shows the development of the fracture field in an annealed glass block measuring 1-1/4 x 5-7/8 x 5-7/8 inches and of hardness 600 K_{100} during impact at 1500 ft/sec with a standard 0.458 caliber ball-nosed bullet weighing 32.5 gm. Unlike the fracture field of Fig. 15 or 16 for the AP bullet, this fracture field is comprised of two distinct parts, a quarter sphere expanding into the glass, and an expanding disk at the impact surface. The observable front of the quarter sphere penetrates at an average velocity which is about one-third of the dilatational velocity for the glass. A reflected fracture field forms about 12 μsec after impact (see Frame 4 of Fig. 19). This reflected field coalesces with the incident field and together they spread throughout the glass block. The bullet, being but a thin shell of soft steel (200 K_{100} and about 1/10 inch thick) filled with lead, "splashes" into the glass to form the disk-shaped portion of the fracture field. Unlike the AP bullet, the ball-nosed bullet does not completely penetrate the glass block even though the entire block is shattered.

E. 0.3 Caliber Standard AP Bullet Impacting a Ceramic Tile

Figure 20 shows a profile view of the impact at 2400 ft/sec of a standard 0.3 caliber AP bullet (see Fig. 6) with a ceramic tile (AD94) 0.34 inch thick. Initially, copper from the jacket and the lead tip of the bullet are spread rapidly across the front surface of the ceramic tile. The first observable sign of tile break-up occurs in Frame 7 at about 16 μsec after impact, long enough for the elastic dilatational wave front in the ceramic to travel 6 inches, or 18 plate thicknesses. The break-up region seen at the rear face of the tile is initially confined to a circular region with a diameter about four times the plate thickness, later increasing to about seven times the plate thickness (5-1/2 and 9-1/2 times the bullet core diameter of 0.25 inch, 4-1/2 and 8 times the bullet diameter of 0.3 inch). After 25 μsec the rear portion of the core becomes exposed. Throughout break-up, much comminution of the ceramic occurs.

Figure 21 is an oblique view of the front face of a ceramic tile during an impact in an experiment which was a repeat of that shown in Fig. 20. The radial scattering of the front portion of the copper jacket and of the lead tip can be seen, followed by ejection of crushed ceramic adjacent to the bullet. At later times the rear portion of the bullet core becomes exposed. During the recording time the front surface of the tile beyond the radial flow of the bullet jacket and tip does not appear to have cracked.

Figure 22 is an oblique view of the rear surface of a ceramic tile during an impact experiment which was a repeat of those described by Figs. 20 and 21. The first observable signs of fracture (Frame 4) occur as several radial cracks and one circumferential crack. The record goes on to show a failure pattern consisting of some 14 sectors of ceramic which rotate about the circular crack. Up to this stage, the pattern is similar to that in the tile impacted by an 0.458 caliber projectile at 1800 ft/sec, as shown in Fig. 9. From about 25 μsec onwards these sectors extend to rotate about a larger, somewhat circular, crack. This spreading to another "circular" crack is very noticeable in these experiments, unlike the behavior in the experiments with the 0.458 caliber projectiles.

Each sector ultimately breaks up into many small pieces, and from the start of break-up, finely crushed ceramic powder is present.

Figure 23 shows two 0.3 caliber AP bullets (one with the jacket partially removed), two major and several minor core fragments, and two major jacket fragments. The two pieces from the rear of the core represent the largest fragments usually retrieved. Figure 24 is an enlargement of one of the core fragments showing its fracture surfaces.

F. 0.3 Caliber Standard AP Bullet Impacting Ceramic-Fiber Glass Composite

Figure 25 gives a profile view of the impact at 2400 ft/sec of a standard 0.3 caliber AP bullet with a composite armor specimen consisting of a ceramic (AD94) facing tile 0.34 inch thick, backed by a 1/4-inch-thick plate of fiber glass (Doron). The early deformation of the flexible backing plate (after Frame 6) is localized to a circular area corresponding in size to the initial circular break-up region of the ceramic tiles shown in Figs. 20 and 22. The fiber glass plate tries to contain the ceramic by membrane action, as exhibited by its conical shape. The effective circular restraining region of the back-up plate eventually begins to spread rapidly, because the plate is being sheared from the back surface of the facing plate. Terminal observations indicate that the plane of weakest shear resistance is usually not at the bond but at the layer of weave adjacent to the bond.

Figure 26 shows the ceramic-fiber glass composite of Fig. 25 after the impact event. A comparison of Figs. 25 and 26 illustrates the considerable recovery of the flexible back-up plate and the rebound position of the remaining top portion of the facing plate.

Figure 27 shows the fracture pattern in a ceramic tile after an impact experiment identical with that of Fig. 25. The top surface has 10 radial vertical cracks which penetrate the entire thickness, and a circular crack about 3 inches in diameter. Some of the relatively large pie-shaped pieces between this circular crack and a circle about 1 inch in diameter remain in place. At the bottom surface, in a central region about 2 inches in diameter, there are over twice as many radial cracks as

at the top surface. Also in this region is a tiered structure of ceramic with fracture surfaces sloping towards the impact zone. The fracture pattern is identical with those obtained in similar experiments with 0.458 caliber AP projectiles (compare Figs. 12 and 27).

G. 0.3 Caliber Standard AP Bullet Impacting a Glass Block

Figure 28 shows the development of the fracture field in an annealed glass block measuring 1-1/4 x 5-7/8 x 5-7/8 inches and of hardness 600 K_{100} during impact at 2400 ft/sec with a standard 0.3 caliber AP bullet. The observable fracture field occupies an expanding hemispherical region with its front moving at 5200 ft/sec, about 0.3 times the dilatational velocity for the glass (taken as 19,000 ft/sec). This is the same velocity as that of the fracture front in a glass block whem impacted by a 0.458 caliber projectile at 1800 ft/sec (see Section 4C and Figs. 15 and 16). In Frame 6 of Fig. 28, a reflected fracture field can be seen forming at the rear surface of the glass block at about 14 μsec after impact. This field coalesces with the incident fracture field and together they spread throughout the block.

Figure 29 shows the fracture field in a similar experiment but now the impact event is viewed through the rear surface of the glass block. As the bullet approaches, the fracture field appears as an expanding area roughly circular in shape. This record, used in conjunction with Fig. 28, helps to form a three-dimensional mental picture of the fracture field.

Figure 30 shows the overall deformation or break-up of the glass block in an experiment similar to those of Figs. 28 and 29. No appreciable displacement of the rear surface occurs until 42 μsec after the impact (Frame 8). The dilatational wave front at this time has traveled about 2-1/2 inches and the estimated position of the bullet tip is 0.9 inch from the front surface. The bullet emerges from the glass block with a velocity of 1900 ft/sec.

In these experiments the bullet core is always retrieved intact, but the copper jacket is always stripped off and does not get through the glass.

H. 0.5-Inch-Diameter Spall Piece Impacting Glass Block

Figure 31 shows the formation of a smooth conoidal fracture surface in an annealed glass block measuring 1-1/4 x 5-7/8 x 5-7/8 inches during impact at 94 ft/sec with a ball-nosed hardened steel spall piece, 0.5 inch in diameter, 0.5 inch long, weighing 11.2 gm. The velocity of the observable fracture front is about 5200 ft/sec, or about 0.3 times the dilatational velocity for the glass. Figure 32 shows the glass block after impact. The conoid has been removed and positioned so that its profile can be clearly seen.

I. 0.5-Inch-Diameter Spall Piece Impacting Glass-Micarta Composite

Figure 33 shows the formation of fractures in a glass plate 1/4-inch thick, glued to a 1/4-inch-thick Micarta plate, during impact at 80 ft/sec with a hardened steel spall piece 0.5 inch in diameter, 1 inch long, weighing 23.5 gm. Many vertical radial cracks form on the underside of the glass plate, emanating from a point just below the point of impact. Each crack has its own variable velocity of propagation. Other records covering a larger time interval in similar experiments show the development of circumferential cracks. The final crack patterns are similar to that of Fig. 34, which is for a similar glass plate without the Micarta backing plate. During the formation of the inner crack circle in Fig. 34, the progress of the radial cracks is arrested. Upon completion of large arcs of the inner crack circle, the nearby radial cracks continue to propagate. Lagging behind the propagating radial cracks is a fracture surface almost parallel to the plate surfaces. As it increases in area it gradually curves down to intersect the lower plate surface in a circle. In Fig. 34 this circle is about 2-3/4 inches in diameter (about 11 plate thicknesses or 5 spall piece diameters).

J. 0.5-Inch-Diameter Spall Piece Impacting Glass Plate

Figure 34 shows the final crack pattern in a 1/4-inch-thick glass plate after impact at 54 ft/sec with a steel spall piece 0.5 inch in diameter, 1.0 inch long, weighing 23.5 gm. The glass plate is glued to a 1/2-inch-thick layer of flexible polyurethane foam (5 lb/ft^3). The

fracture field is centered around the impact point. The fracture pattern consists of a central zone in which the glass is crushed into a coarse powder, surrounded by a general pattern of radial and circumferential cracks. The plate was struck off center to separate out the effect of the plate boundary. The innermost circular crack has the impact point at its center and is therefore essentially unaffected by the plate boundary.

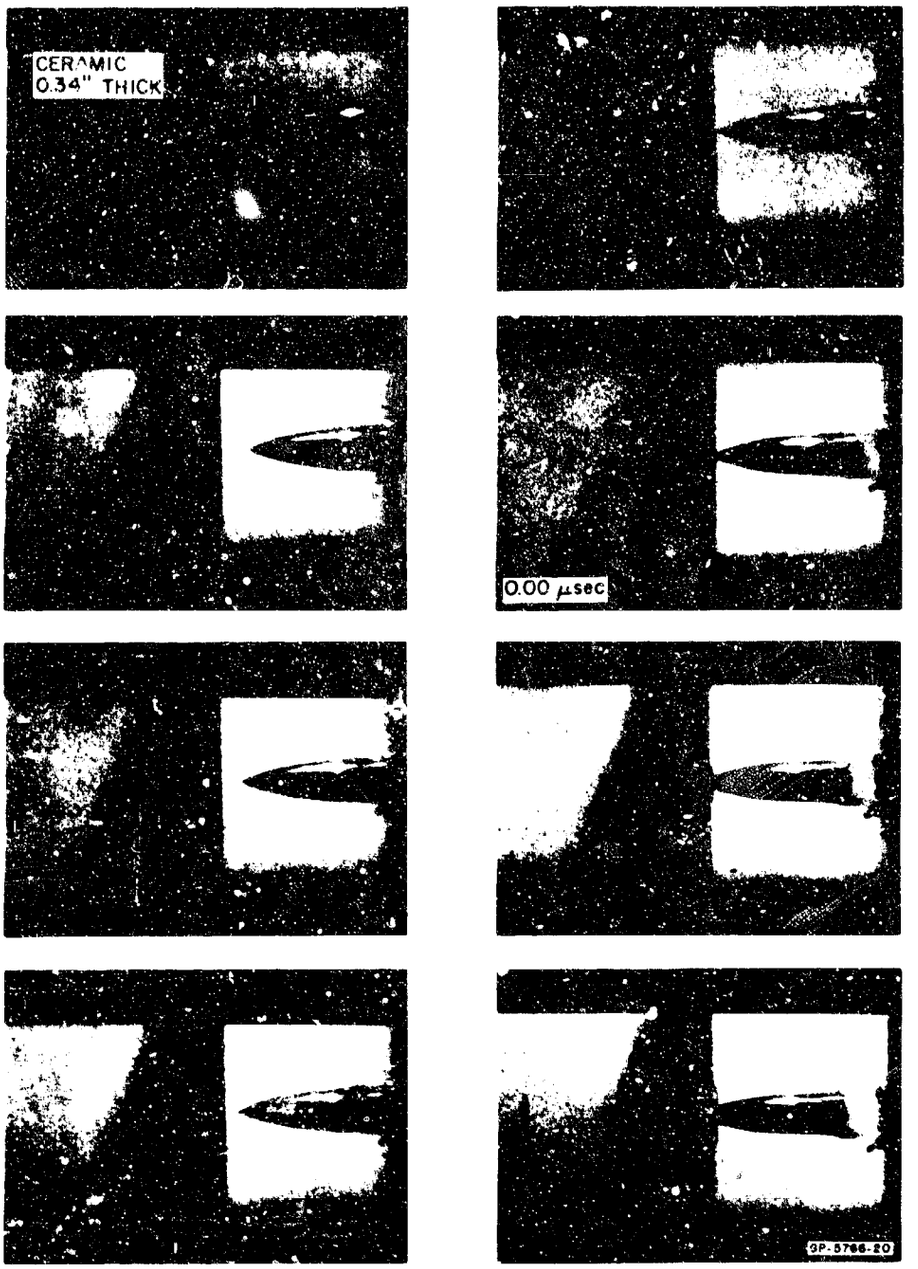

FIG. 7 PROFILE VIEW OF 0.458 CALIBER AP BULLET — CERAMIC TILE IMPACT AT 1800 ft/sec (4.17 μsec between frames)

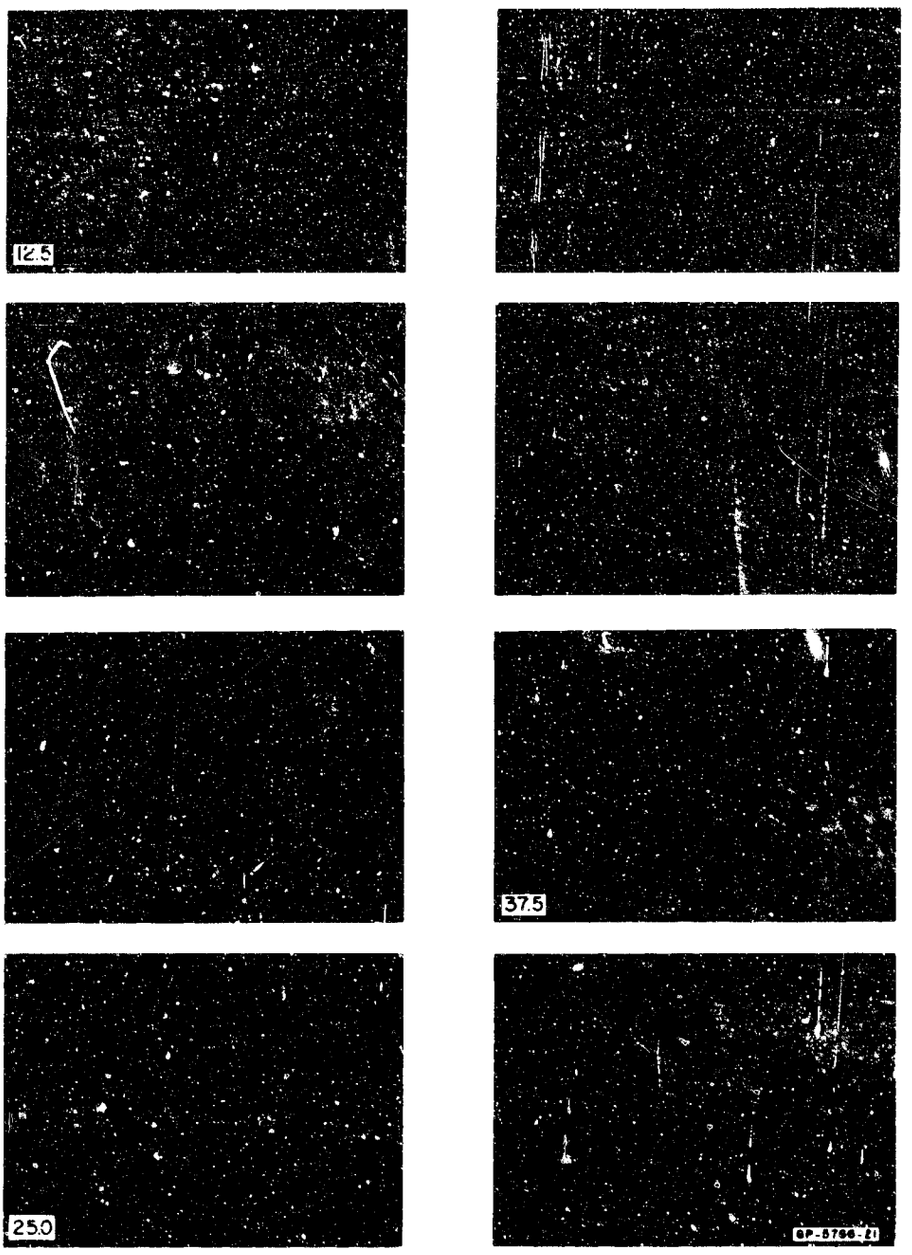

FIG. 7 (Continued)

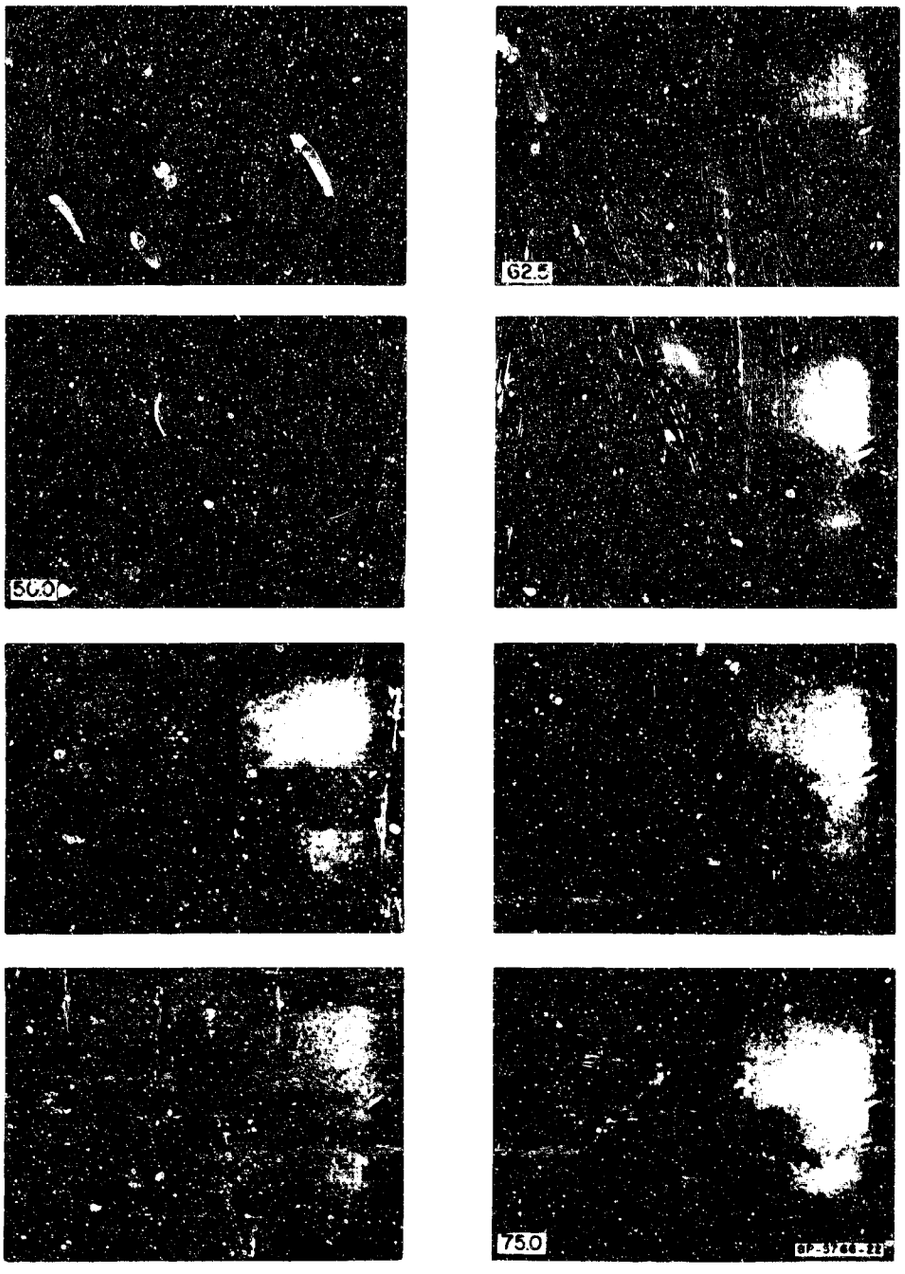

FIG. 7 (Concluded)

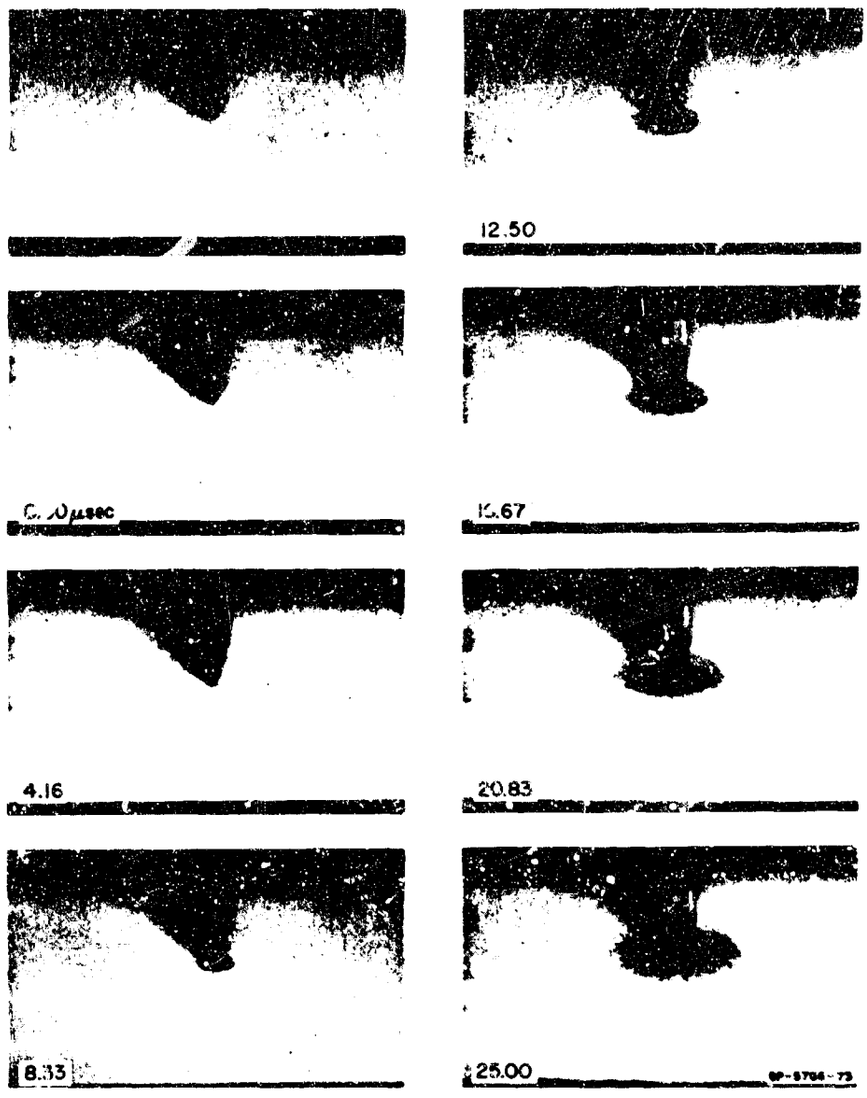

FIG. 8 OBLIQUE FRONT VIEW OF 0.458 CALIBER AP BULLET — CERAMIC TILE IMPACT AT 1800 ft/sec (8.33 μsec between frames)

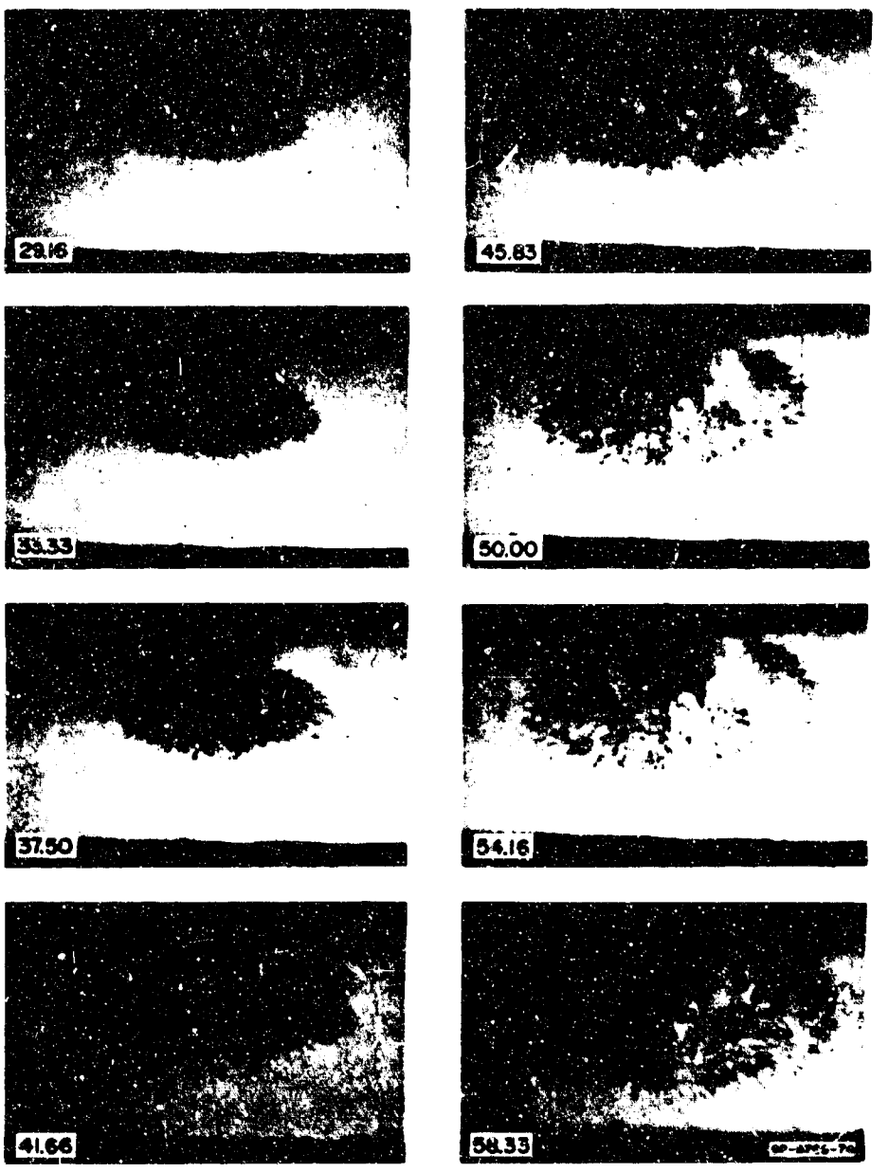

FIG. 8 (Concluded)

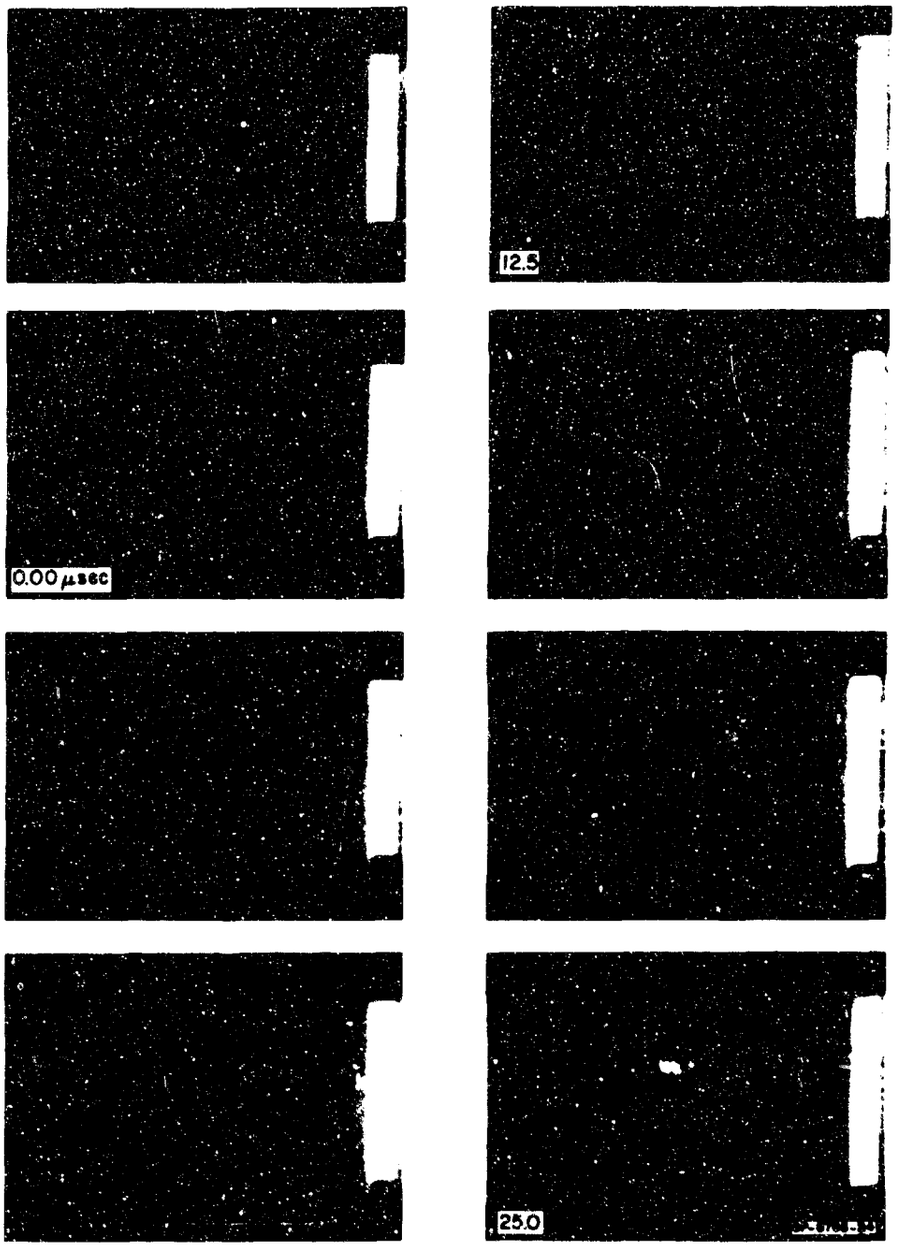

FIG. 9 OBLIQUE REAR VIEW OF 0.458 CALIBER AP BULLET — CERAMIC TILE IMPACT AT 1800 ft/sec (4.17 μsec between frames)

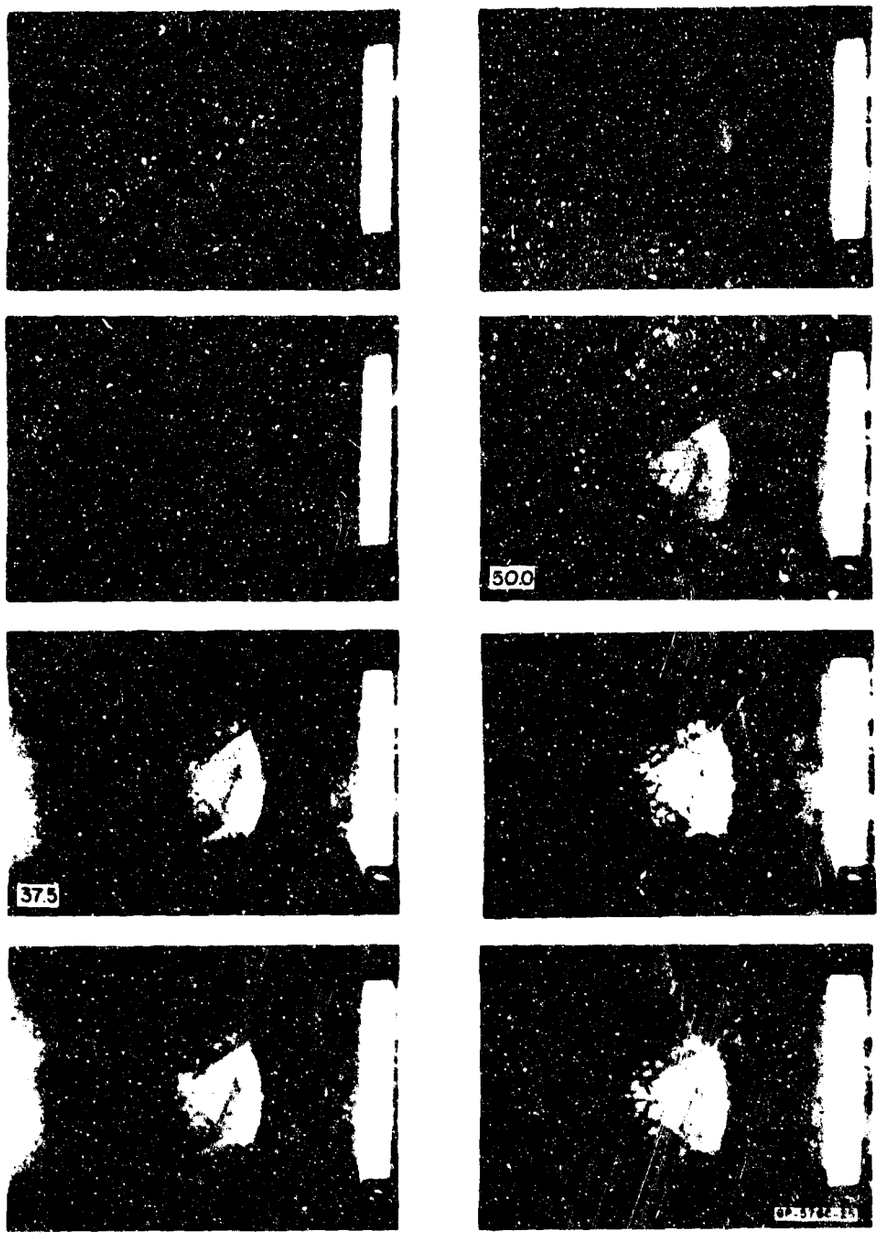

FIG. 9 (Continued)

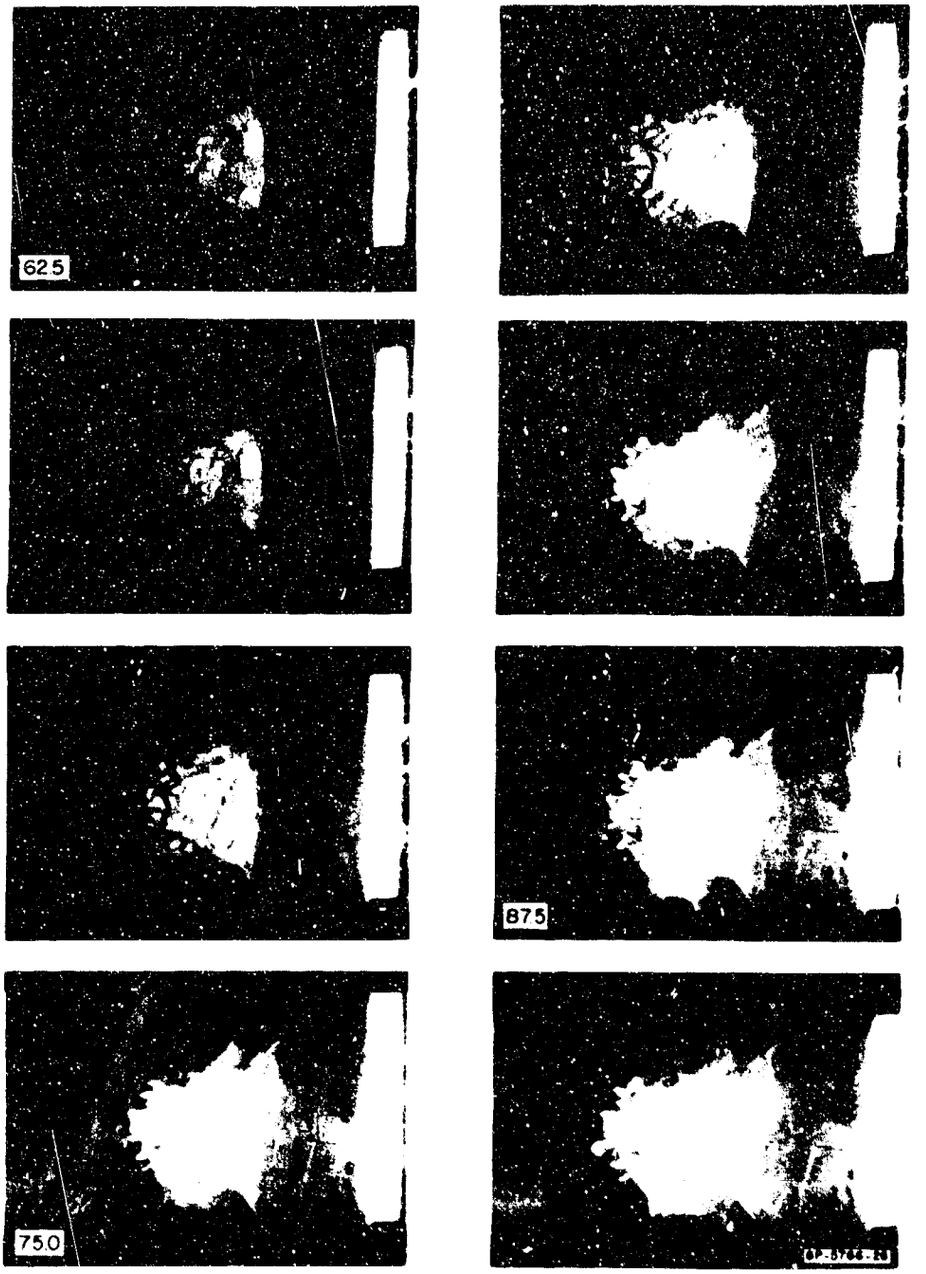

FIG. 9 (Concluded)

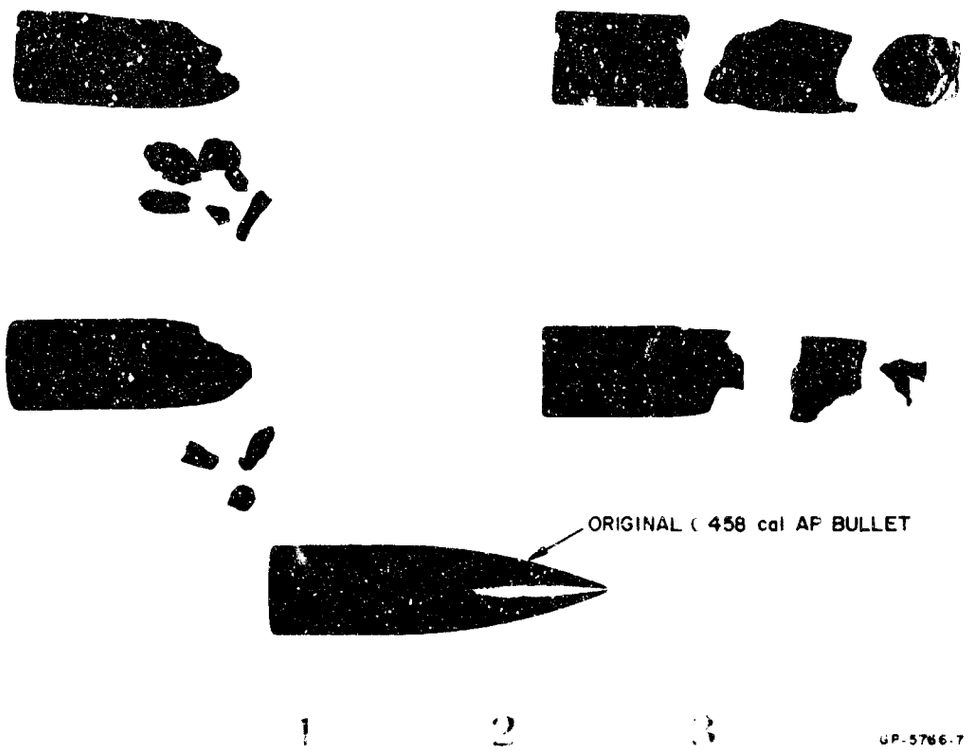

FIG. 10 FRAGMENTS OF 0.458 CALIBER AP BULLETS AFTER IMPACT AT 1800 ft sec WITH CERAMIC TILE

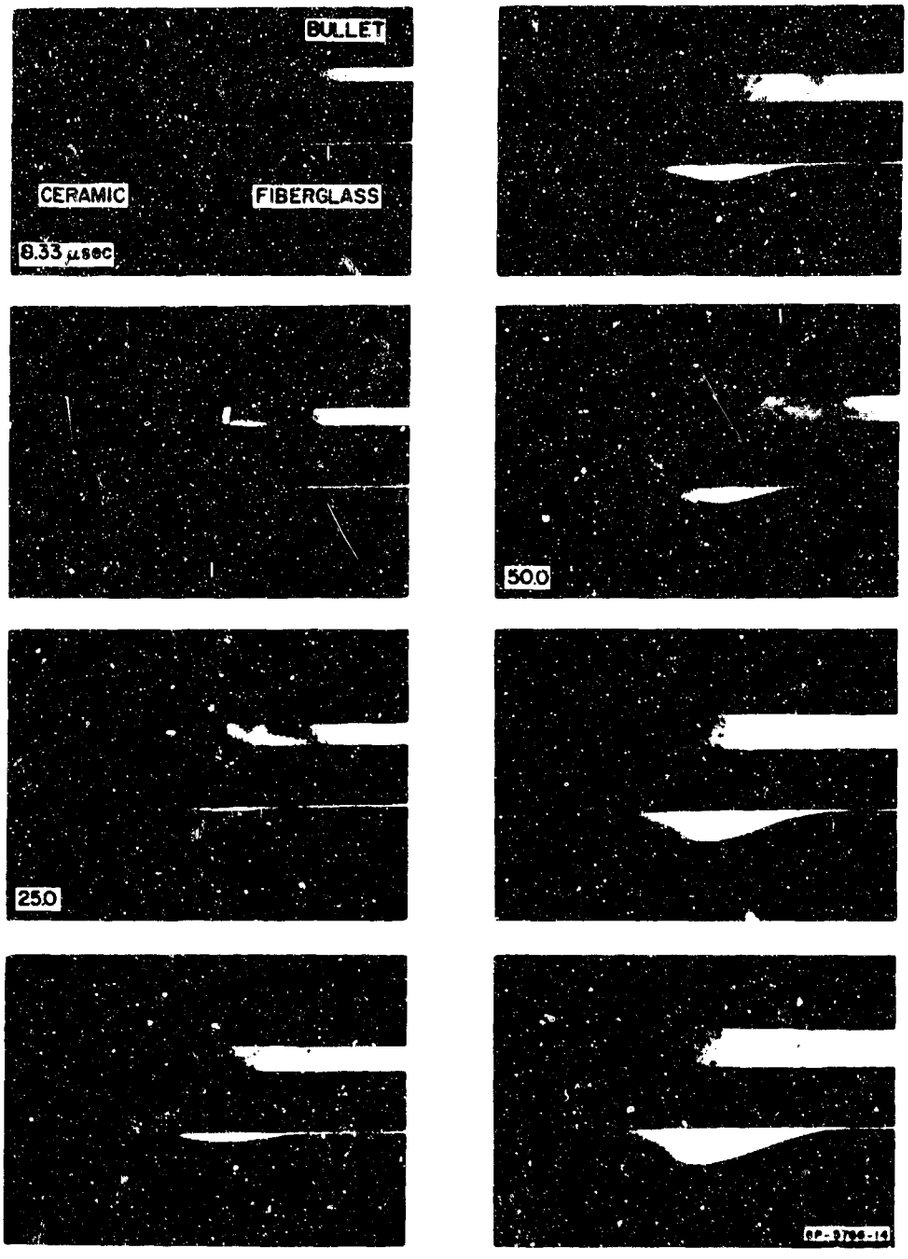

FIG. 11 PROFILE VIEW OF IMPACT OF 0.458 CALIBER AP BULLET WITH CERAMIC-FIBER GLASS COMPOSITE AT 1600 ft sec (8.33 μsec between frames)

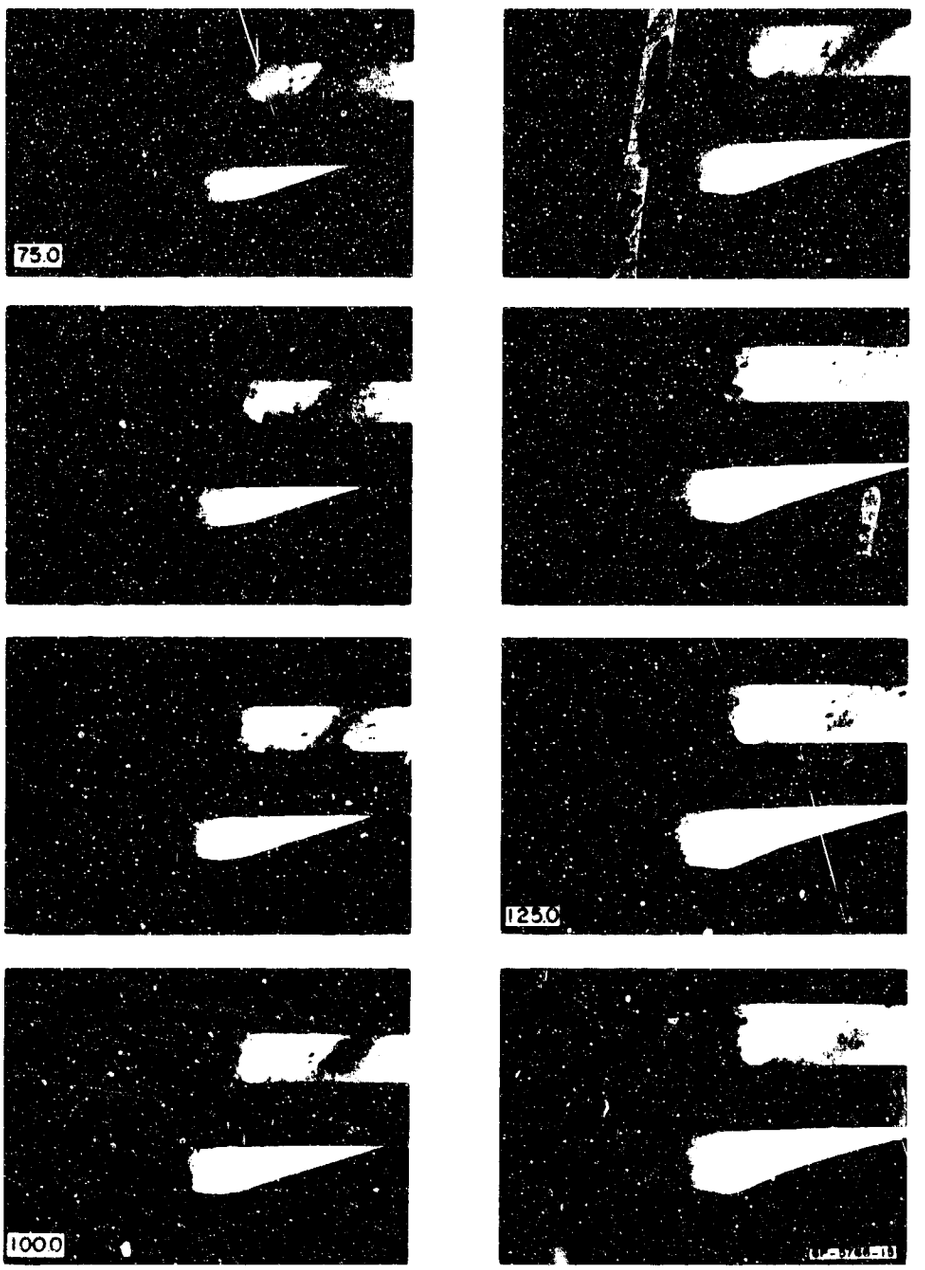

FIG. 11 (Continued)

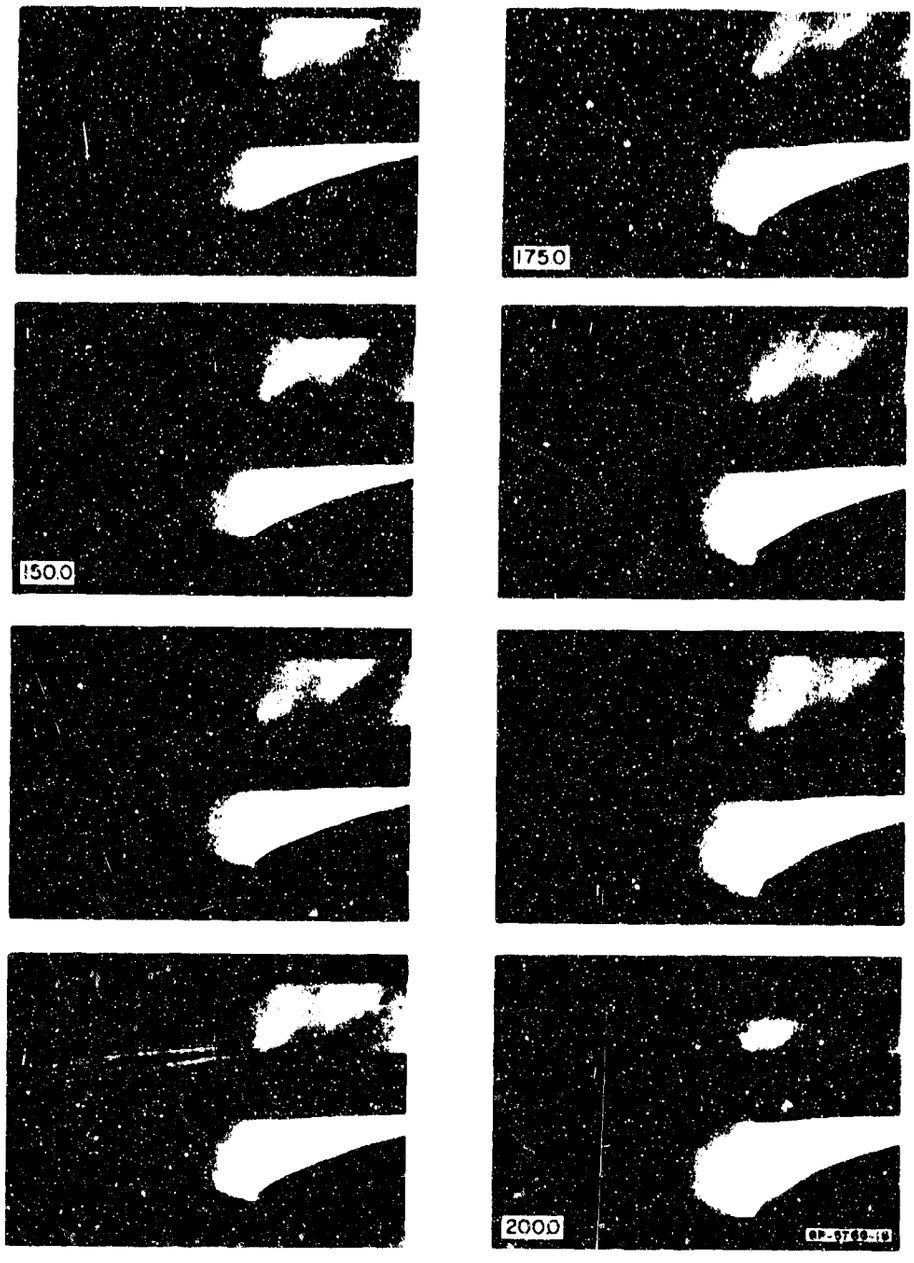

FIG. 11 (Concluded)

FIG. 12 CERAMIC-FIBER GLASS COMPOSITE AFTER IMPACT AT 1800 ft sec WITH 0.458 CALIBER AP BULLET

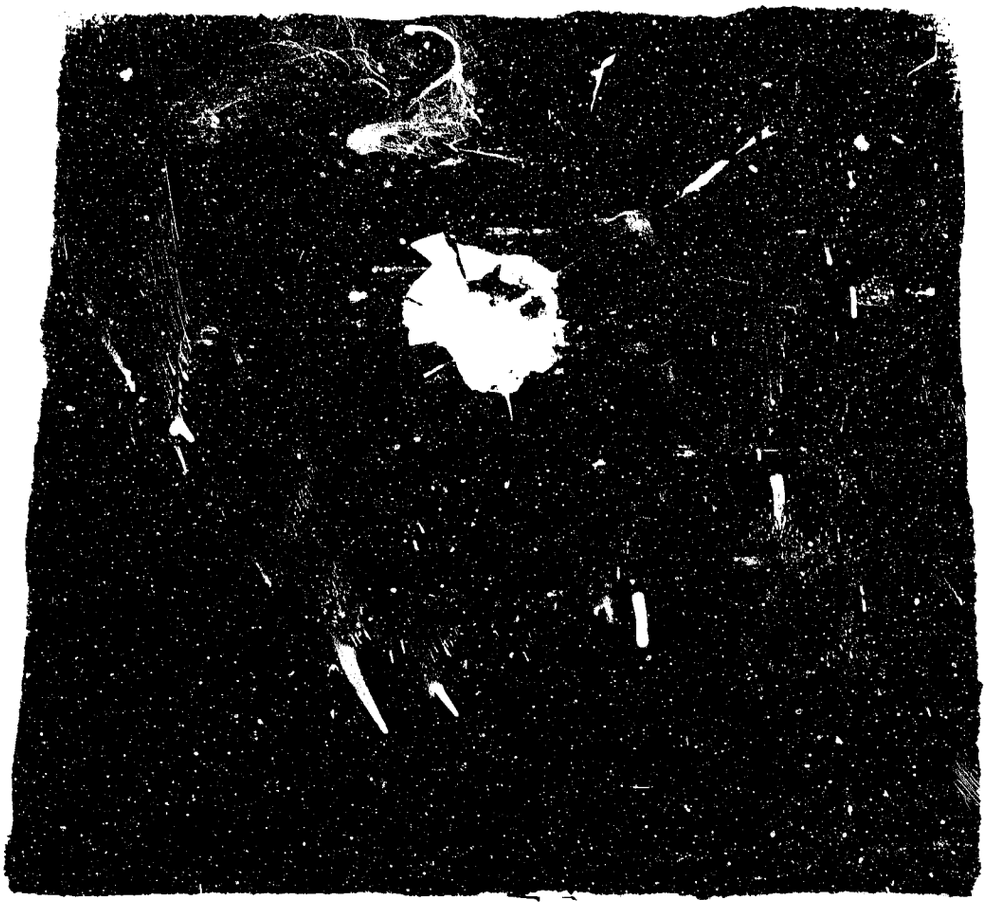

1 2 3 6P-8786-30

FIG. 13 FRONT VIEW OF CERAMIC TILE ON POLYURETHANE FOAM AFTER IMPACT AT 1800 ft/sec WITH 0.458 CALIBER AP BULLET

FIG. 14 REAR VIEW OF CERAMIC TILE OF FIG. 13

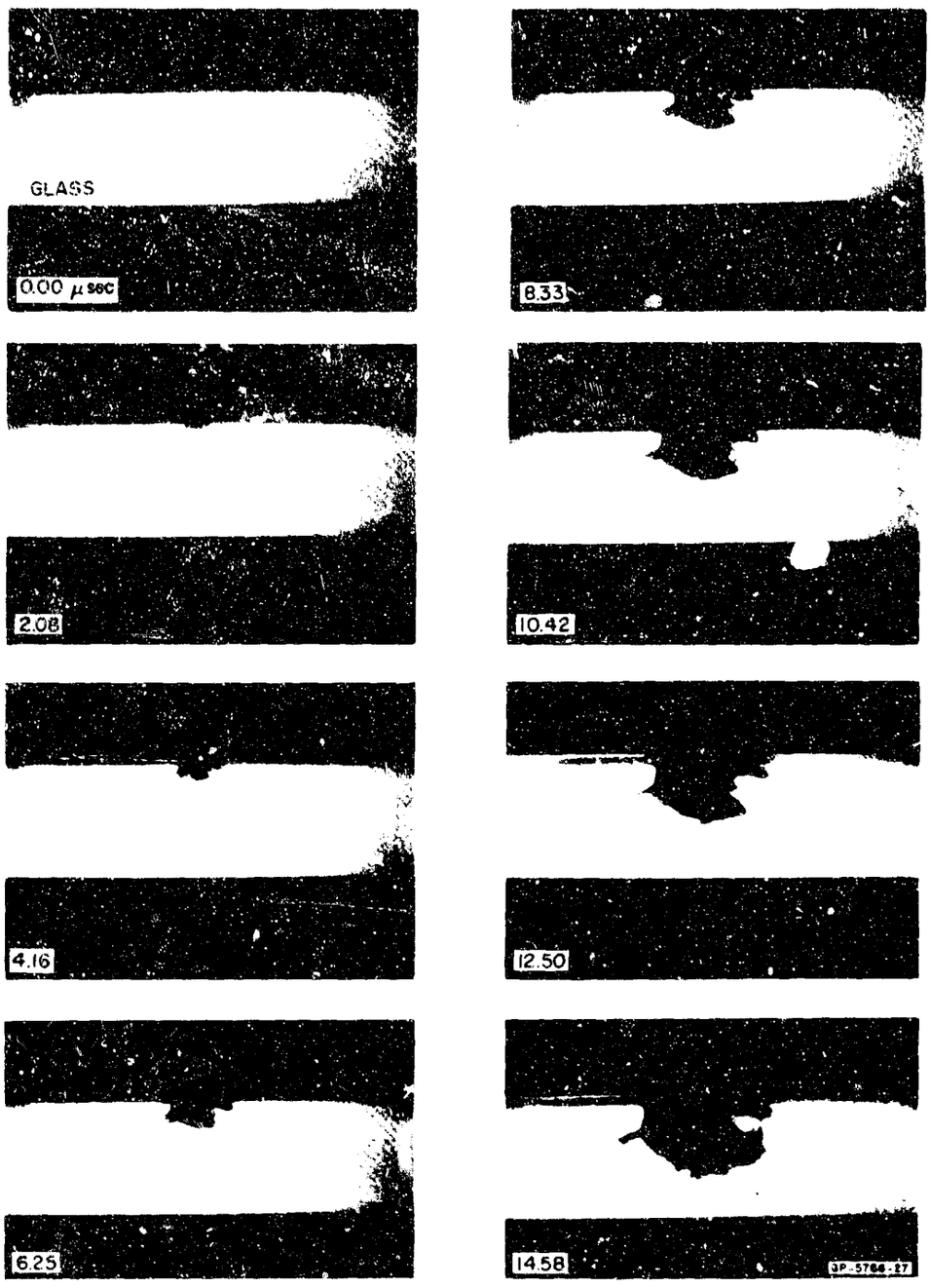

FIG. 15 INTERNAL PROFILE VIEW OF 0.458 CALIBER AP BULLET — GLASS BLOCK IMPACT AT 1800 ft/sec (2.08 μsec between frames)

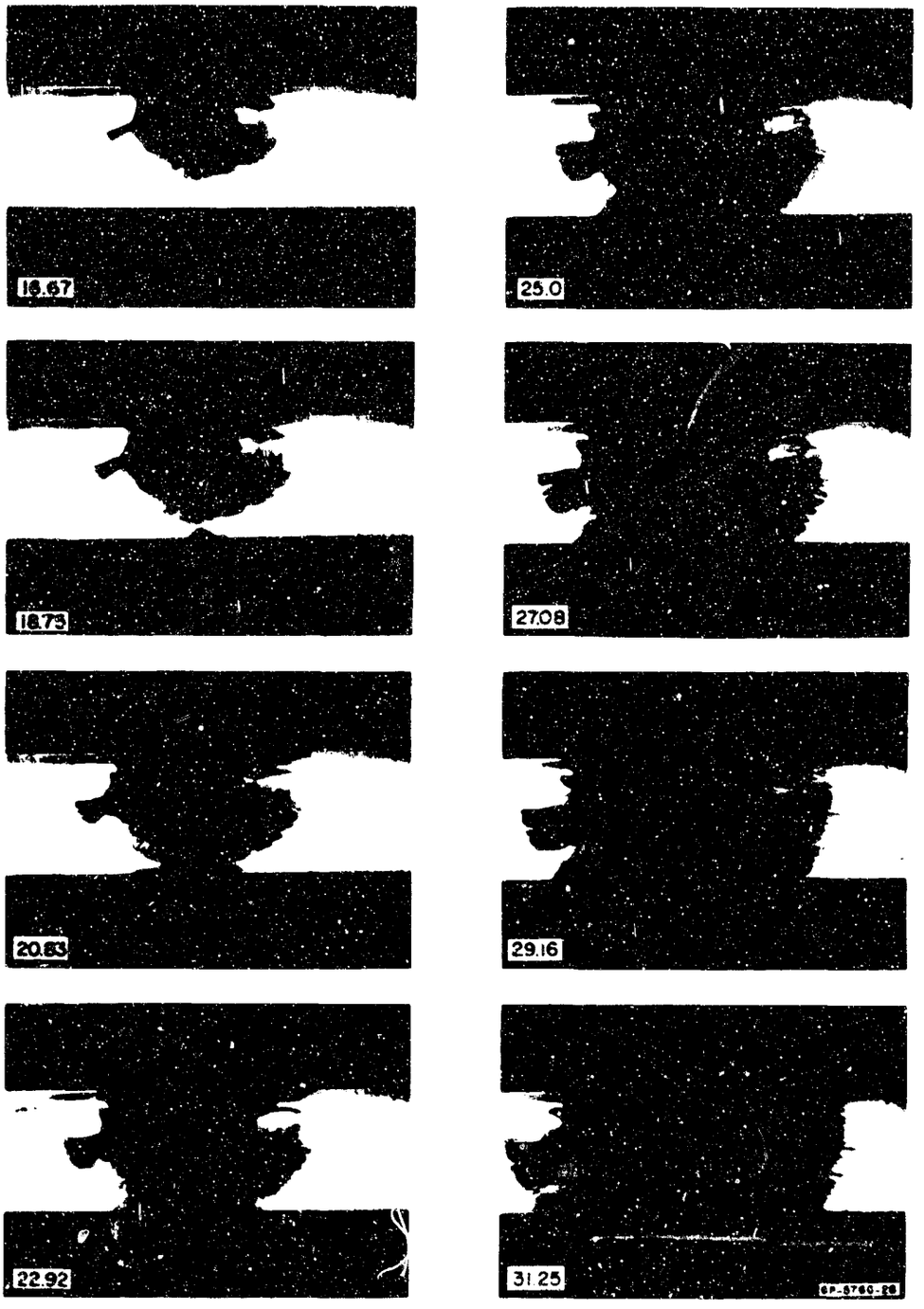

FIG. 15 (Concluded)

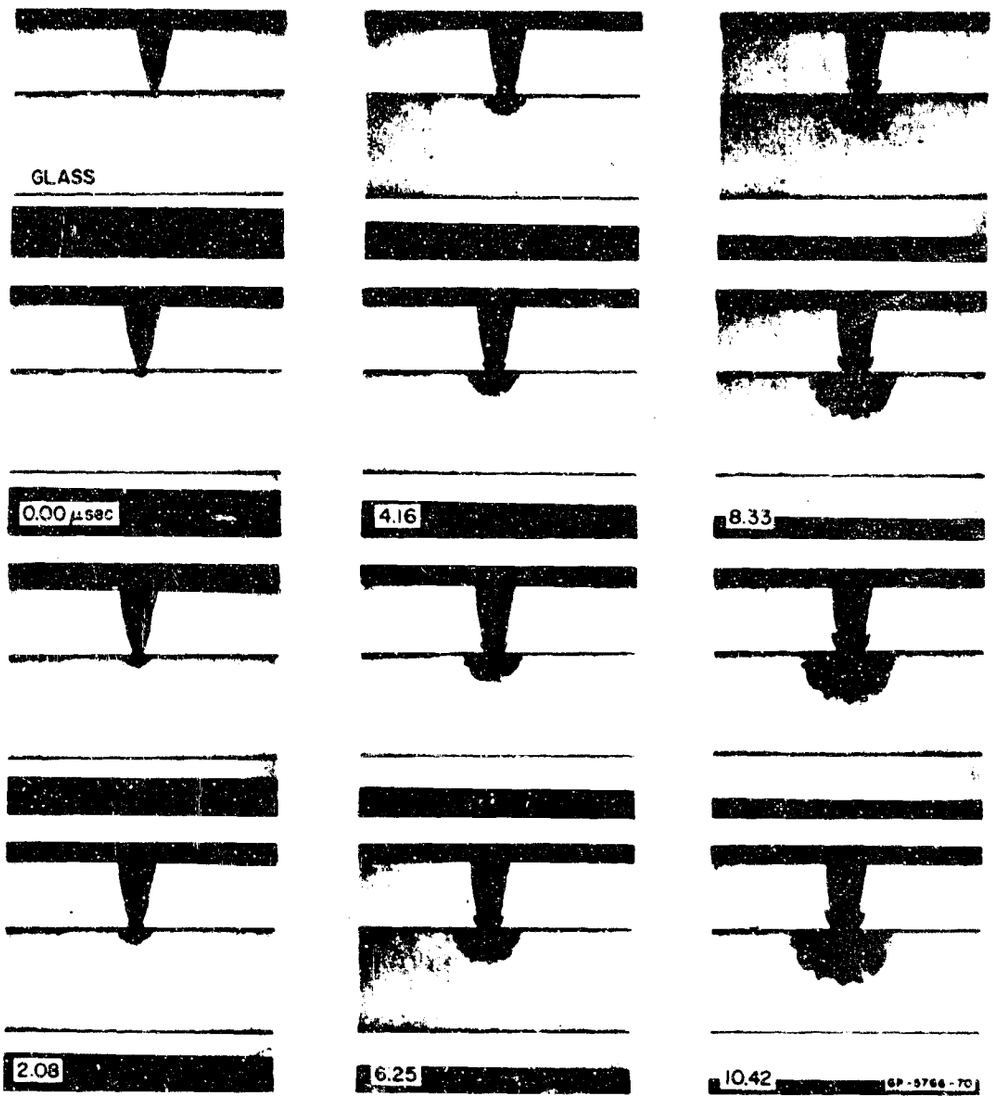

FIG. 16 INTERNAL PROFILE VIEW OF 0.458 CALIBER AP BULLET — GLASS BLOCK IMPACT AT 1800 ft/sec (1.04 μsec between frames)

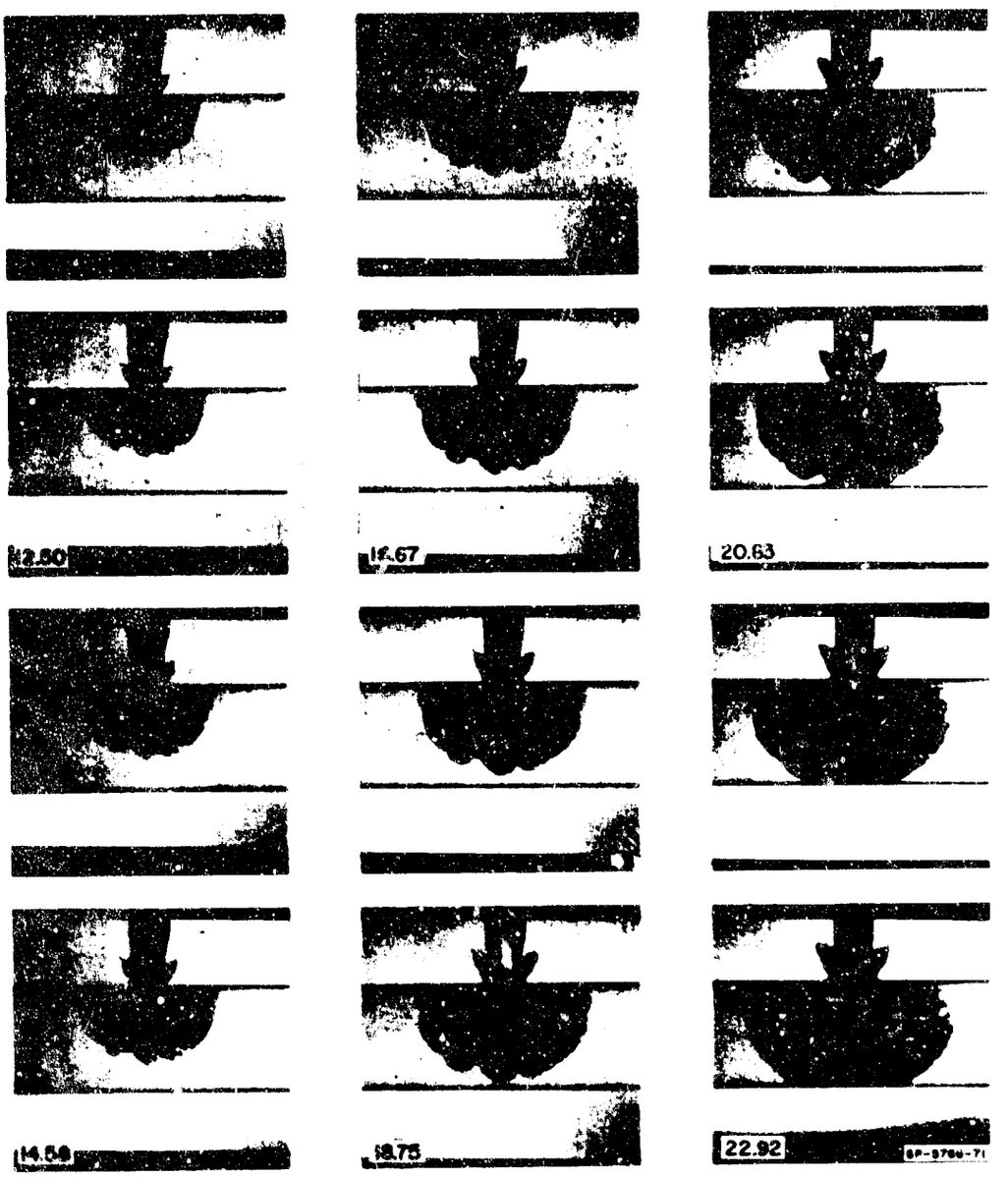

FIG. 16 (Concluded)

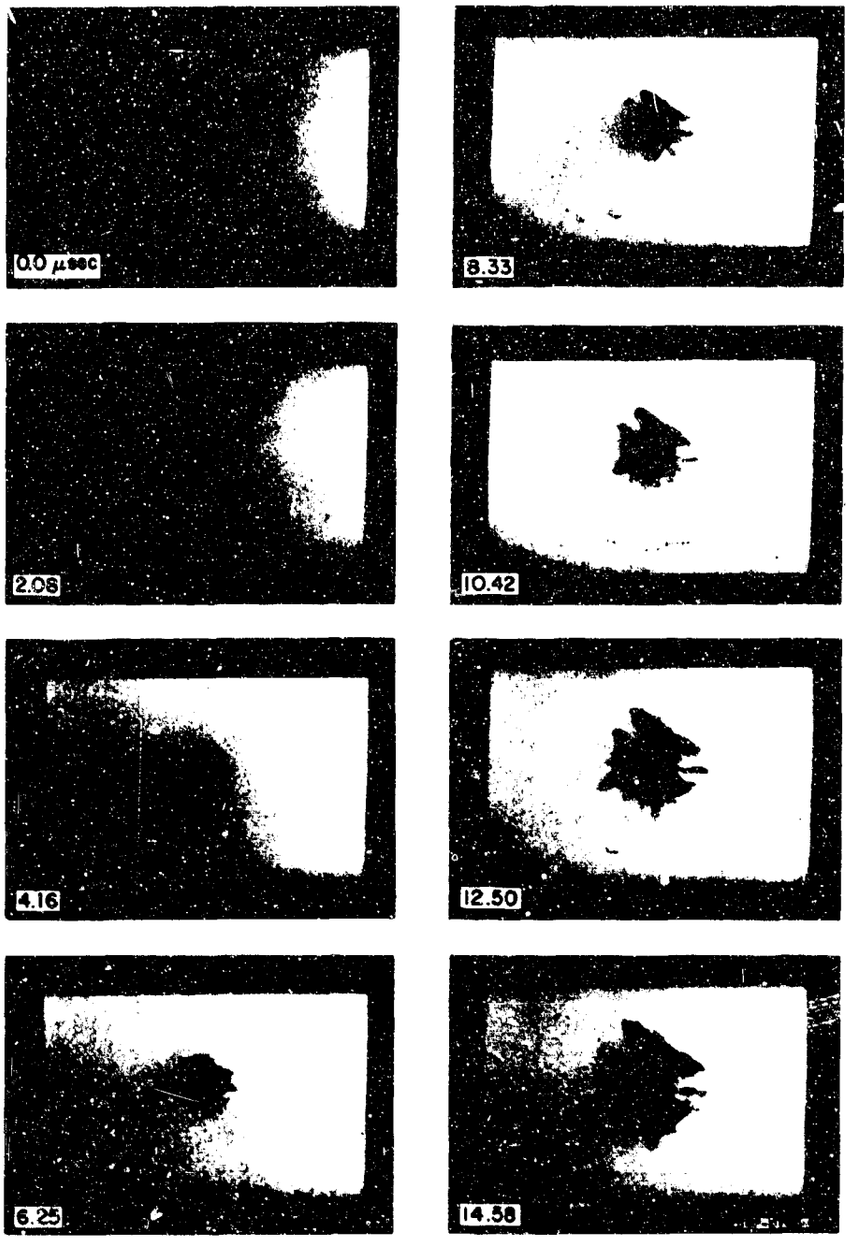

FIG. 17 HEAD-ON VIEW OF 0.458 CALIBER AP BULLET — GLASS BLOCK IMPACT AT 1800 ft sec (2.08 μsec between frames)

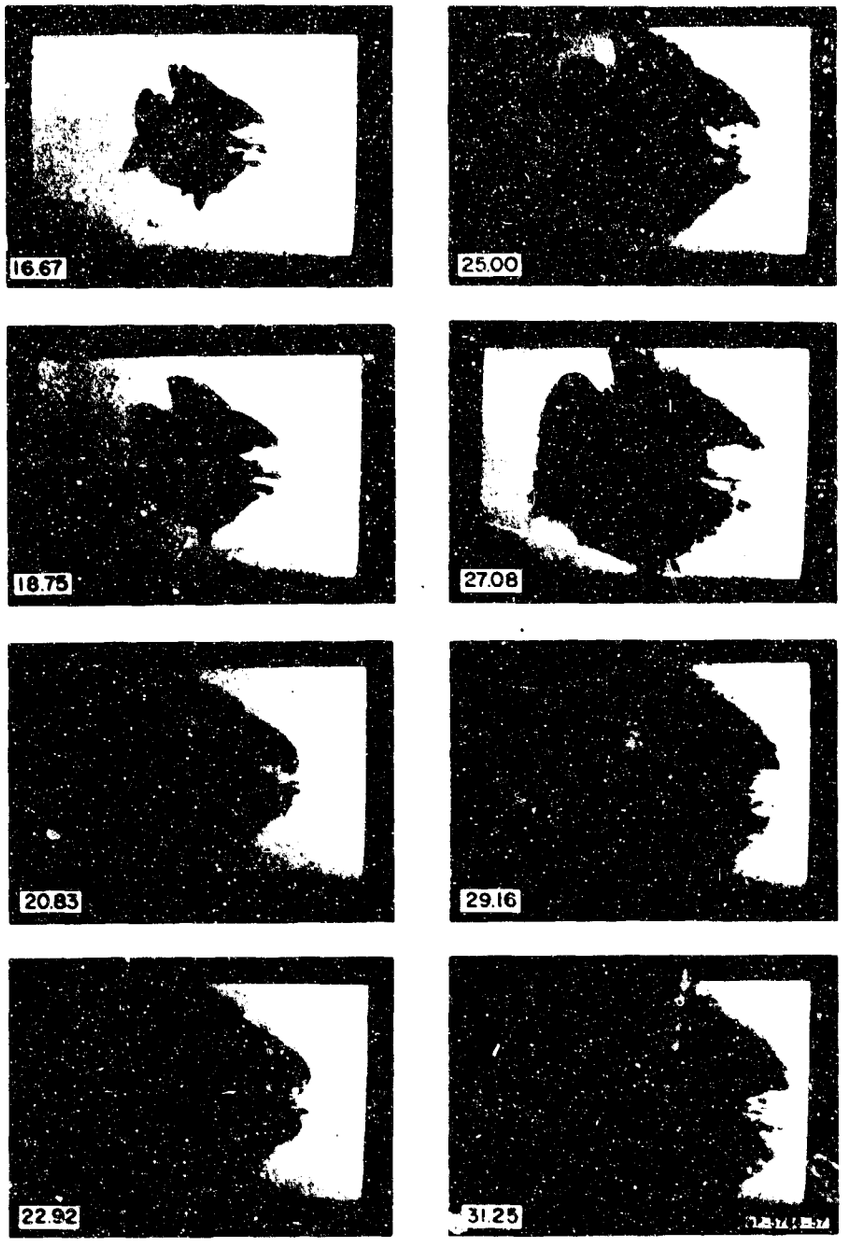

FIG. 17 (Concluded)

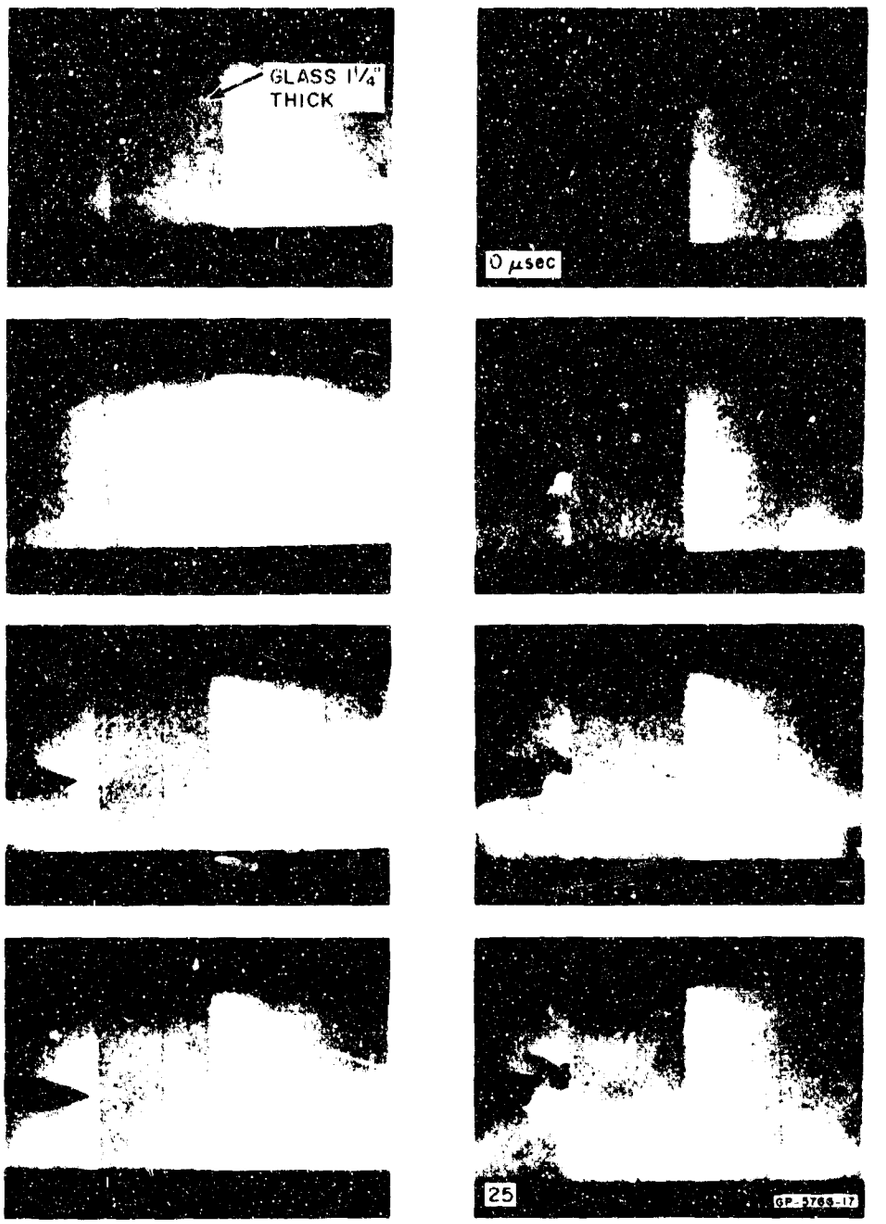

FIG. 18 EXTERNAL PROFILE VIEW OF 0.458 CALIBER AP BULLET — GLASS BLOCK IMPACT AT 1800 ft sec (8.33 μsec between frames)

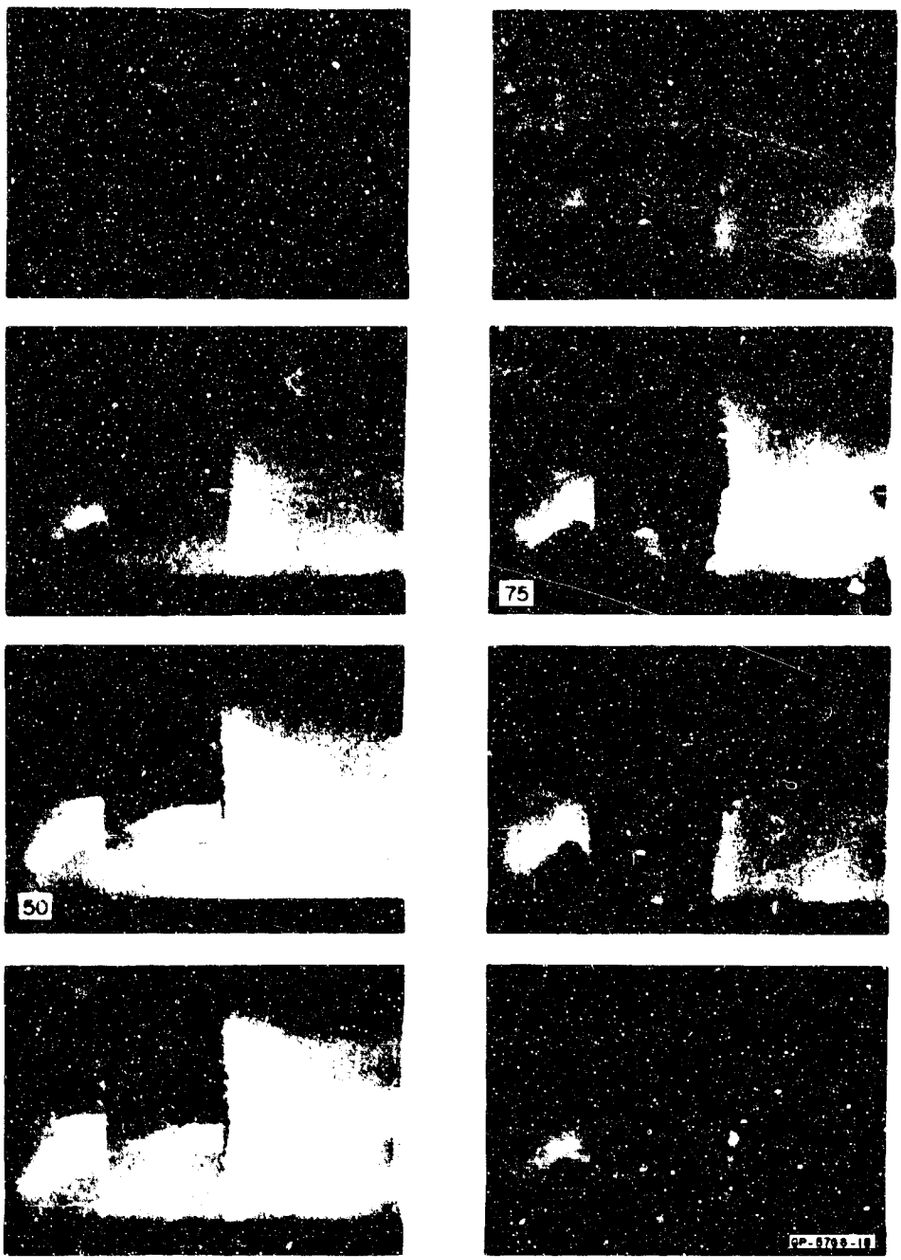

FIG. 18 (Continued)

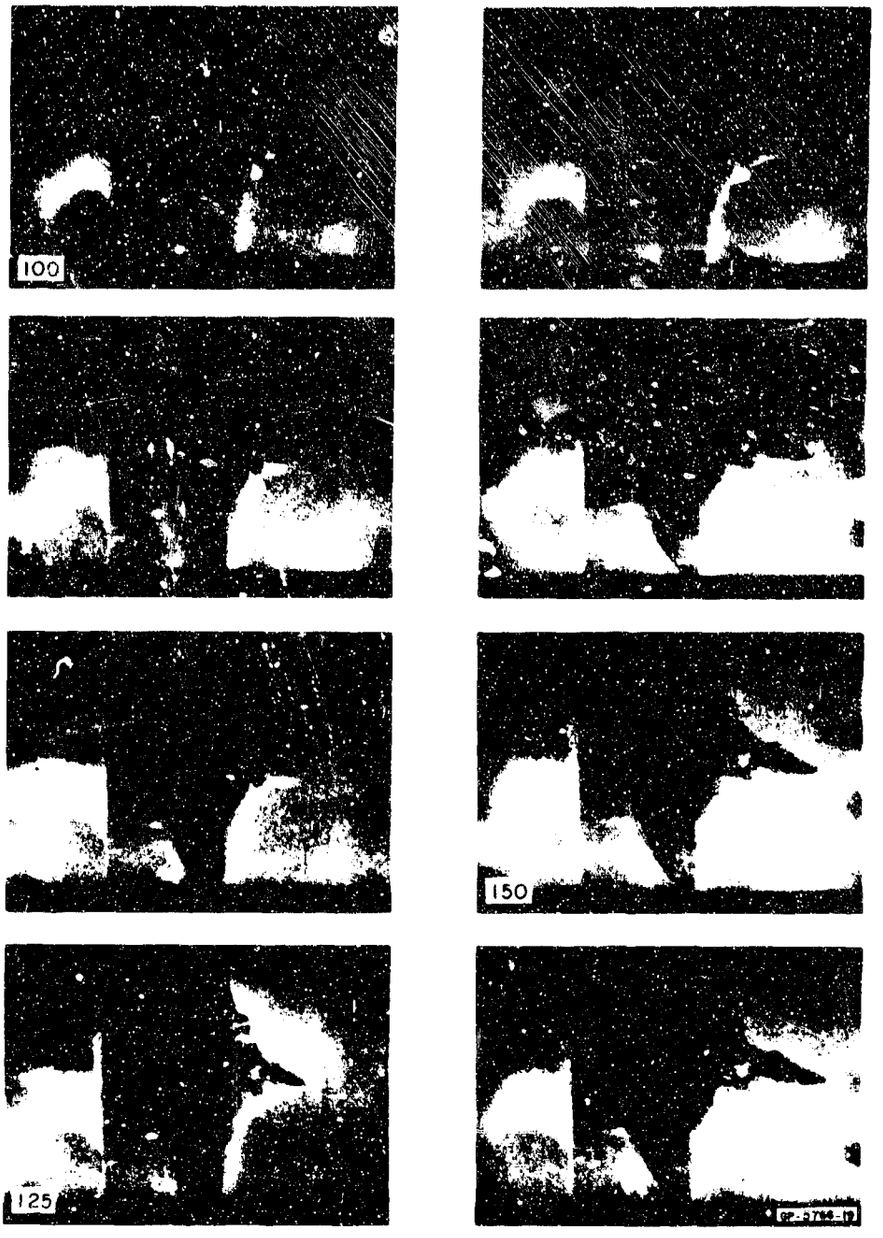

FIG. 18 (Concluded)

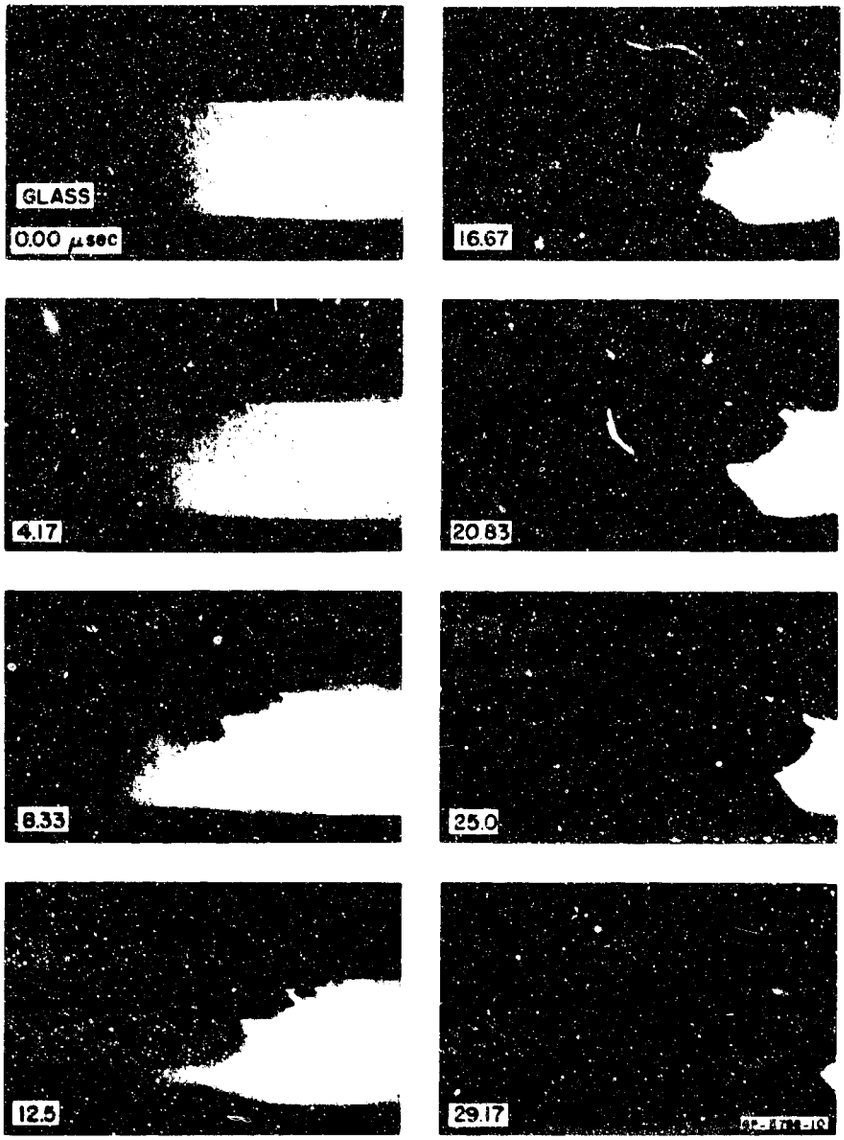

FIG. 19 INTERNAL PROFILE VIEW OF STANDARD 0.458 CALIBER BALL-NOSED BULLET — GLASS BLOCK IMPACT AT 1800 ft/sec (4.17 μsec between frames)

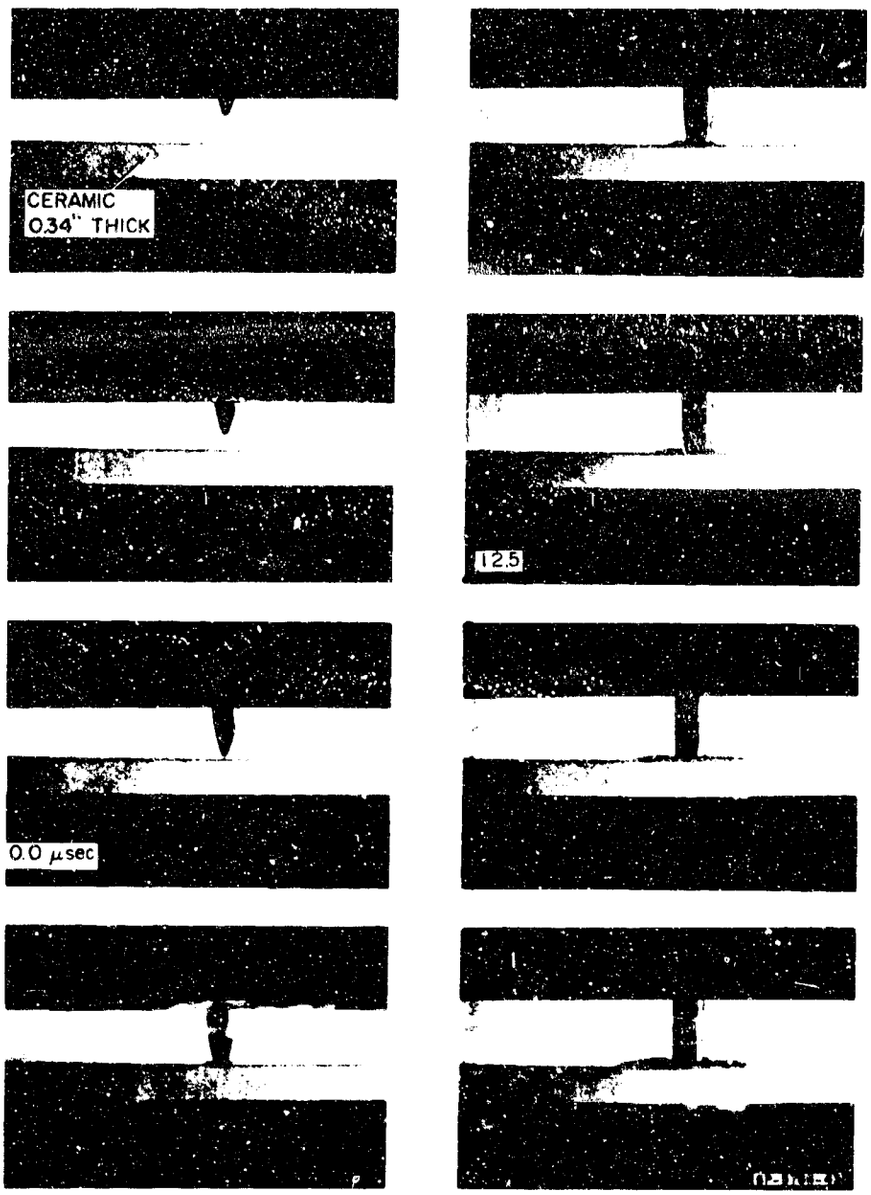

FIG. 20 PROFILE VIEW OF 0.3 CALIBER STANDARD AP BULLET — CERAMIC TILE IMPACT AT 2400 ft sec (4.17 μsec between frames)

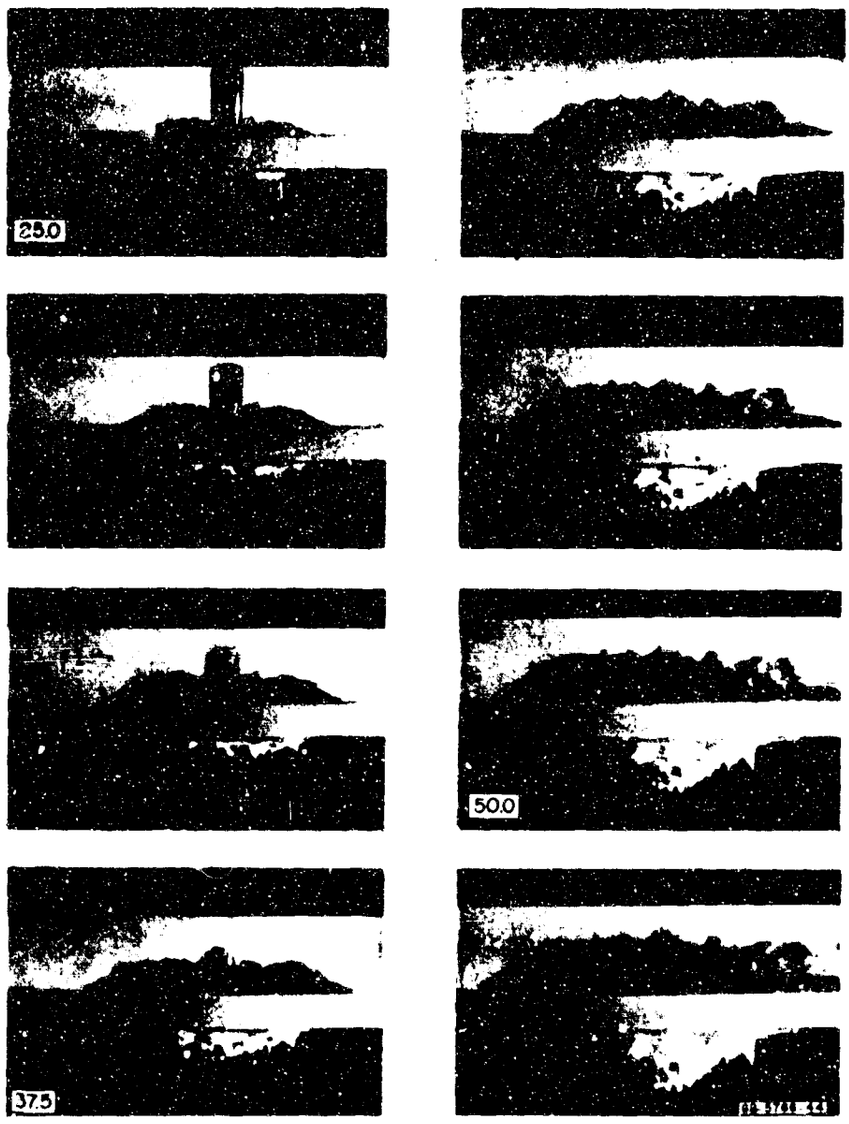

FIG. 20 (Continued)

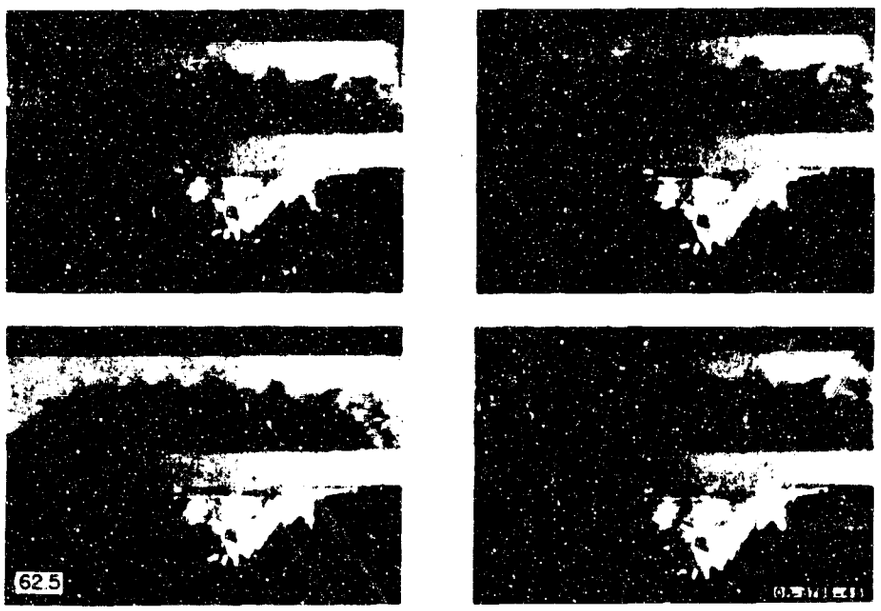

FIG. 20 (Concluded)

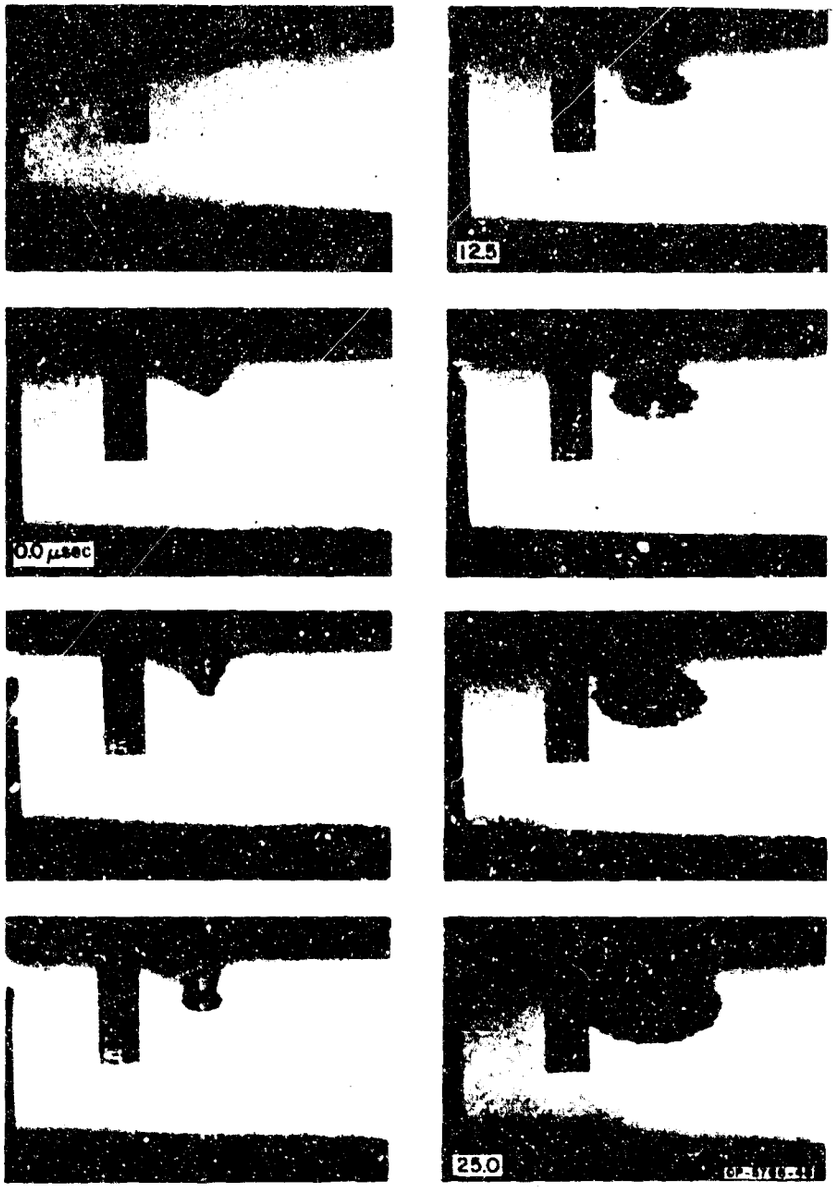

FIG. 21 OBLIQUE FRONT VIEW OF 0.3 CALIBER STANDARD AP BULLET — CERAMIC TILE IMPACT AT 2400 ft sec (4.17 μsec between frames)

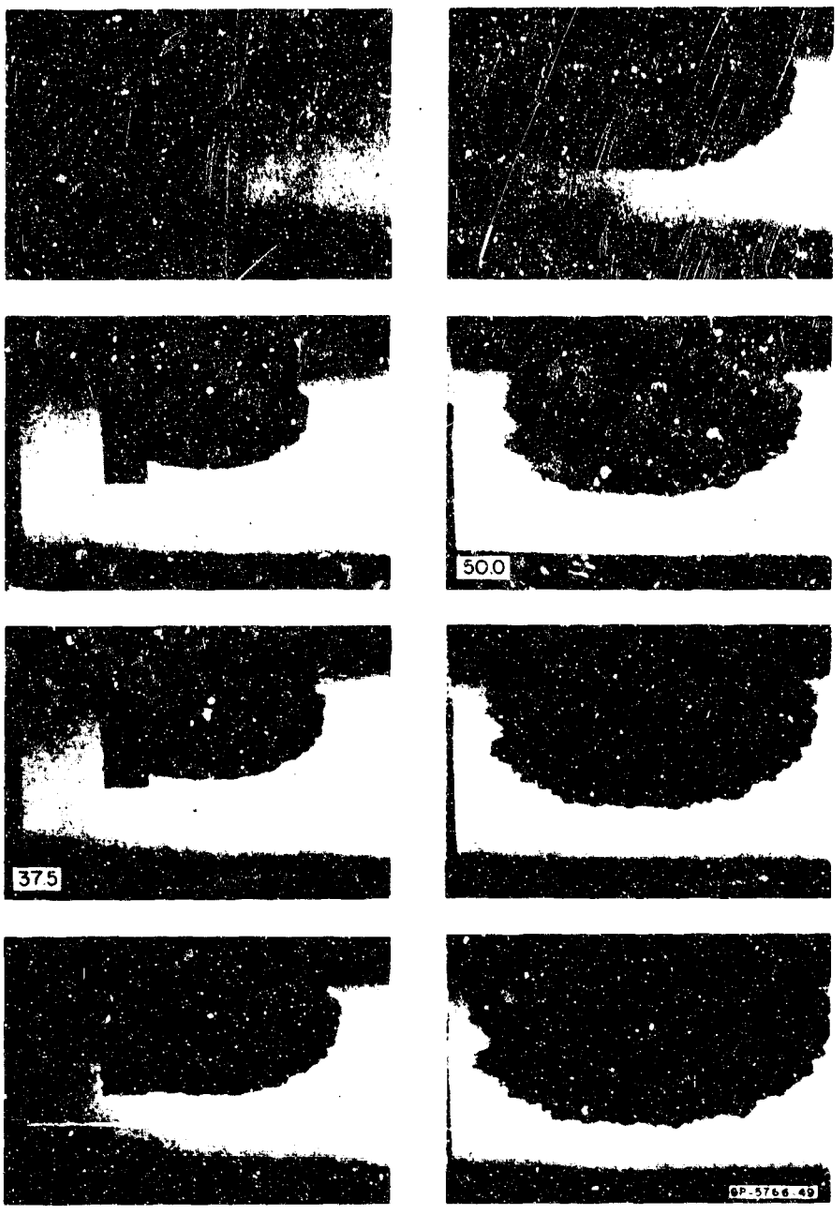

FIG. 21 (Concluded)

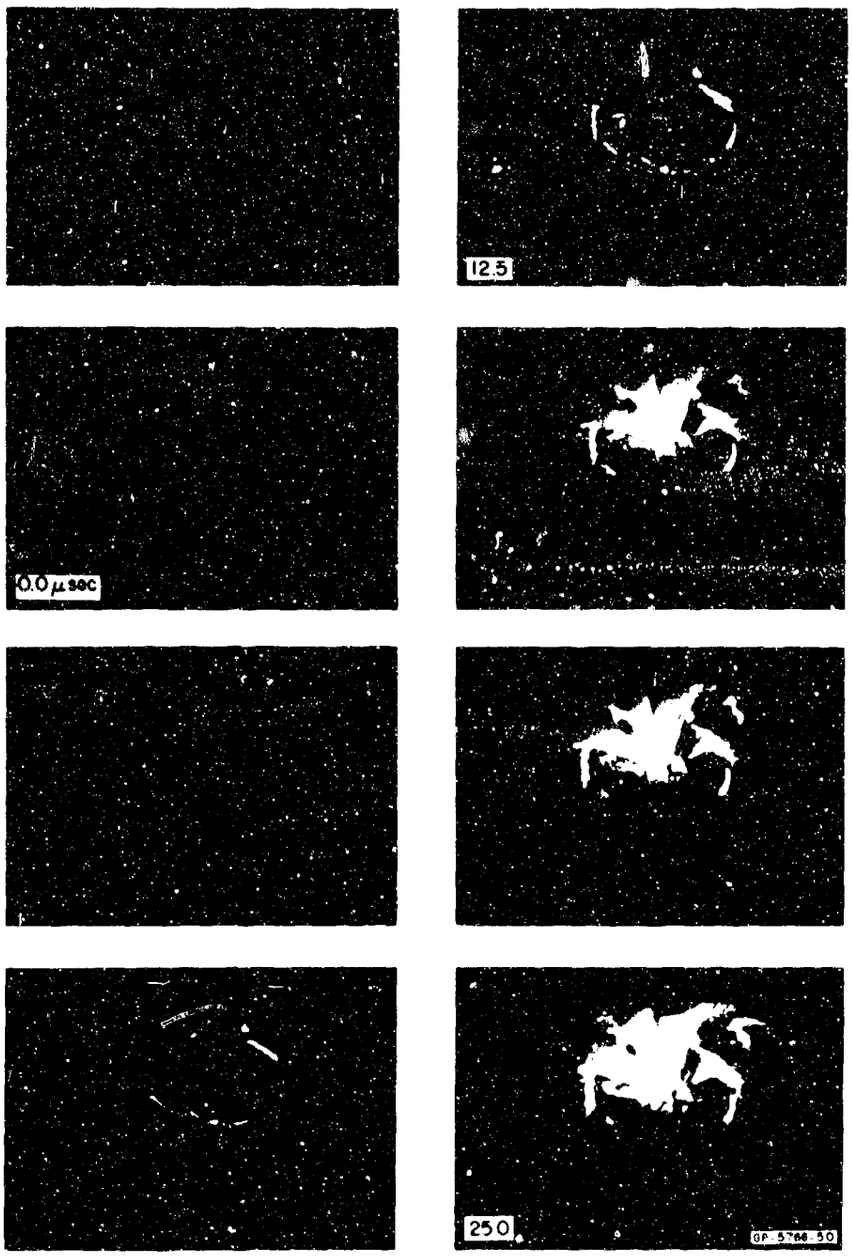

FIG. 22 OBLIQUE REAR VIEW OF 0.3 CALIBER STANDARD AP BULLET — CERAMIC TILE IMPACT AT 2400 ft sec (4.17 μsec between frames)

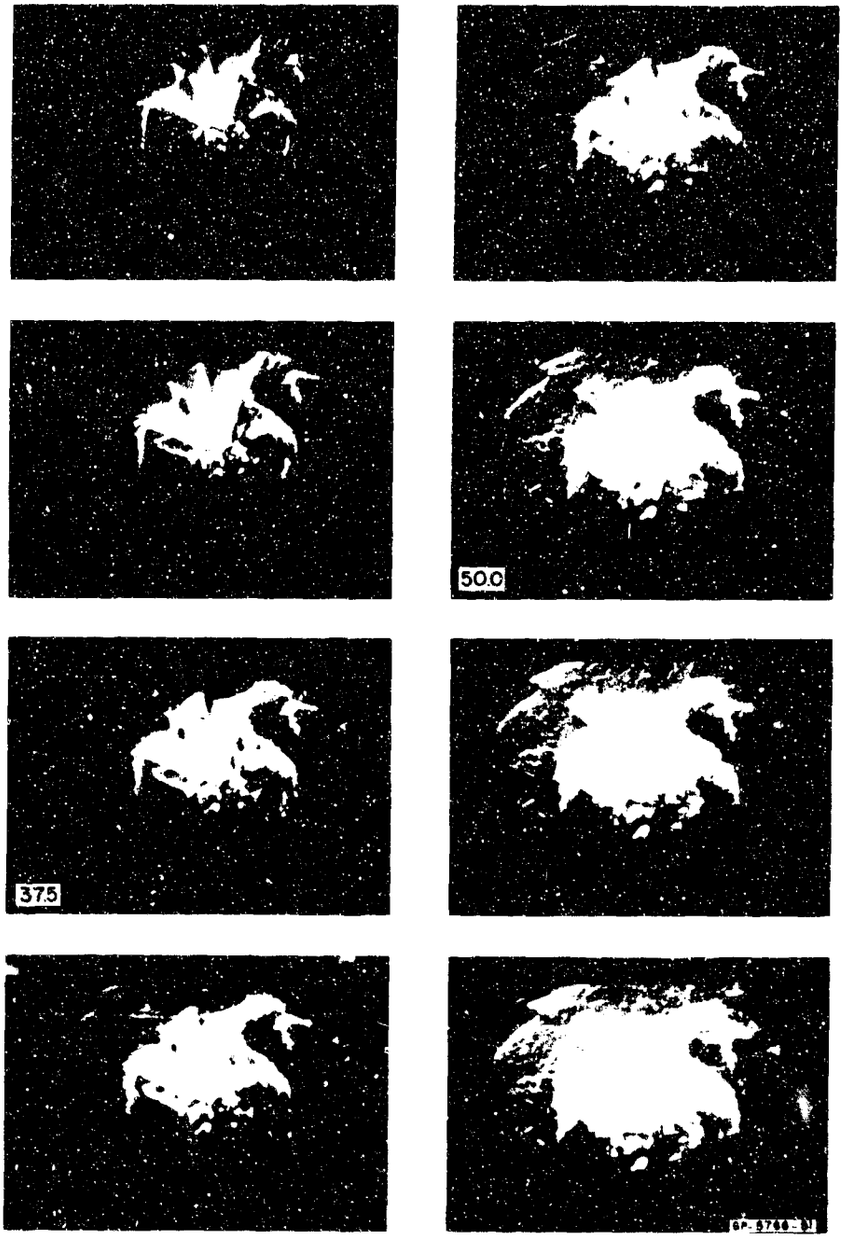

FIG. 22 (Continued)

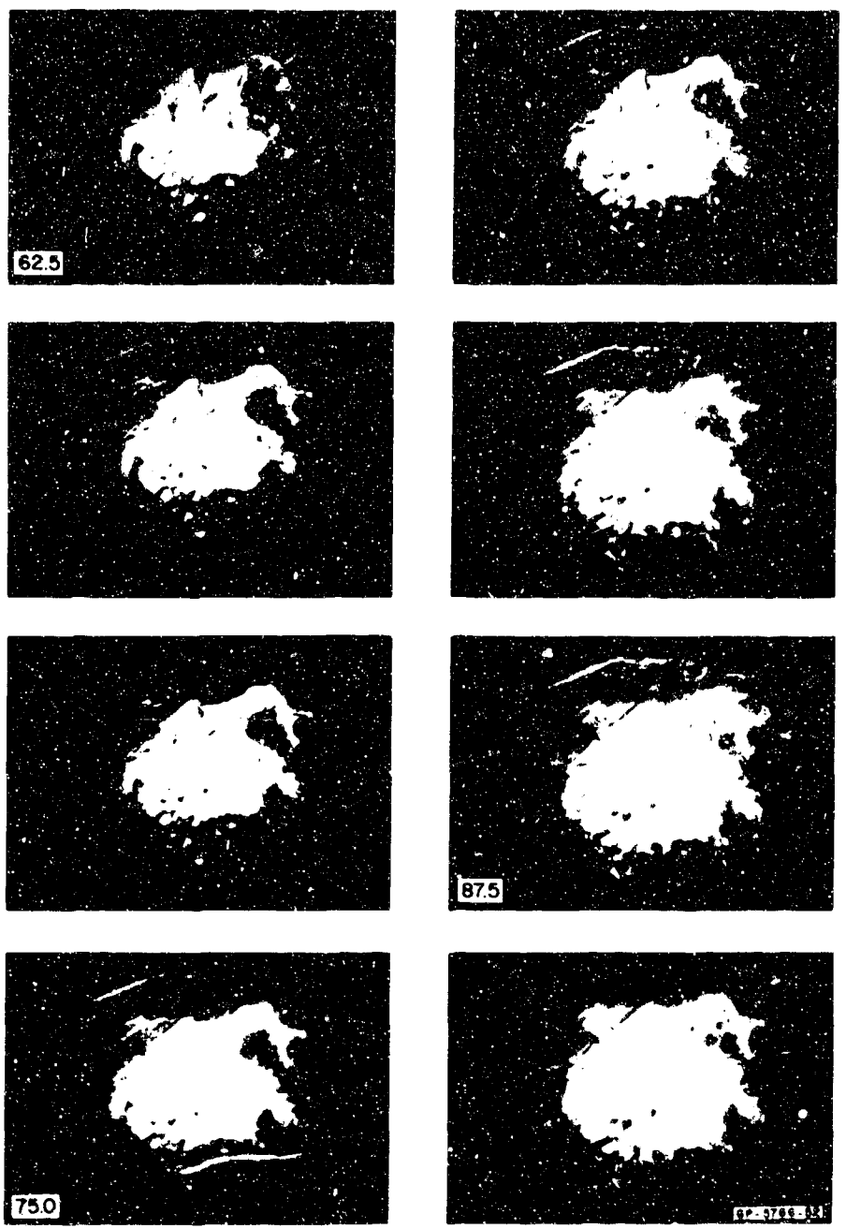

FIG. 22 (Concluded)

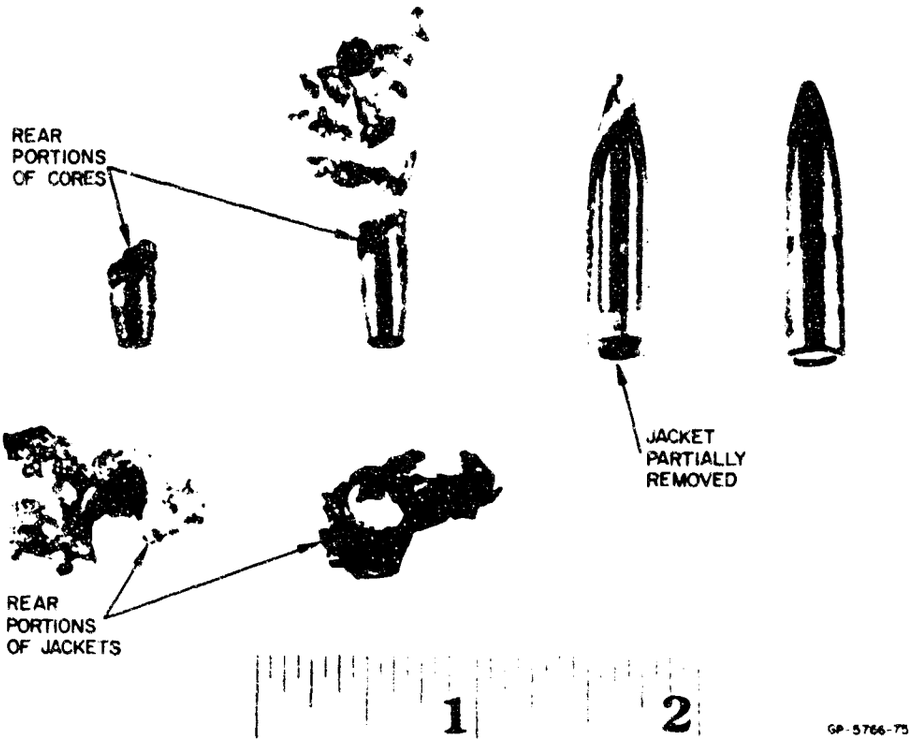

FIG. 23 FRAGMENTS OF 0.3 CALIBER STANDARD AP BULLET AFTER IMPACT AT 2400 ft/sec WITH CERAMIC TILE

GP-8766-76

FIG. 24 DETAIL OF REAR PORTION OF CORE OF 0.3 CALIBER STANDARD AP BULLET SHOWING FRACTURE AND FRACTURE SURFACES

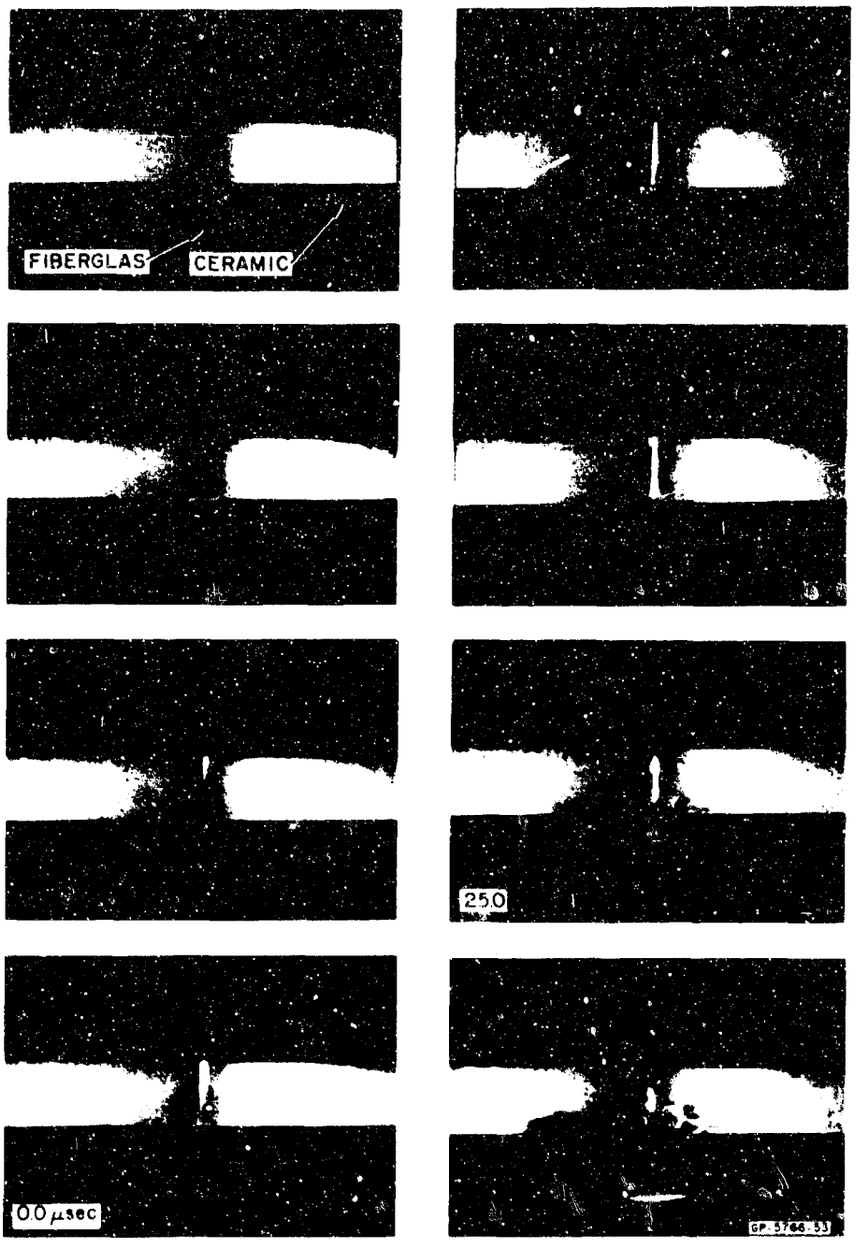

FIG. 25 PROFILE VIEW OF IMPACT OF 0.3 CALIBER STANDARD AP BULLET WITH CERAMIC-FIBER GLASS COMPOSITE AT 2400 ft sec (8.33 μsec between frames)

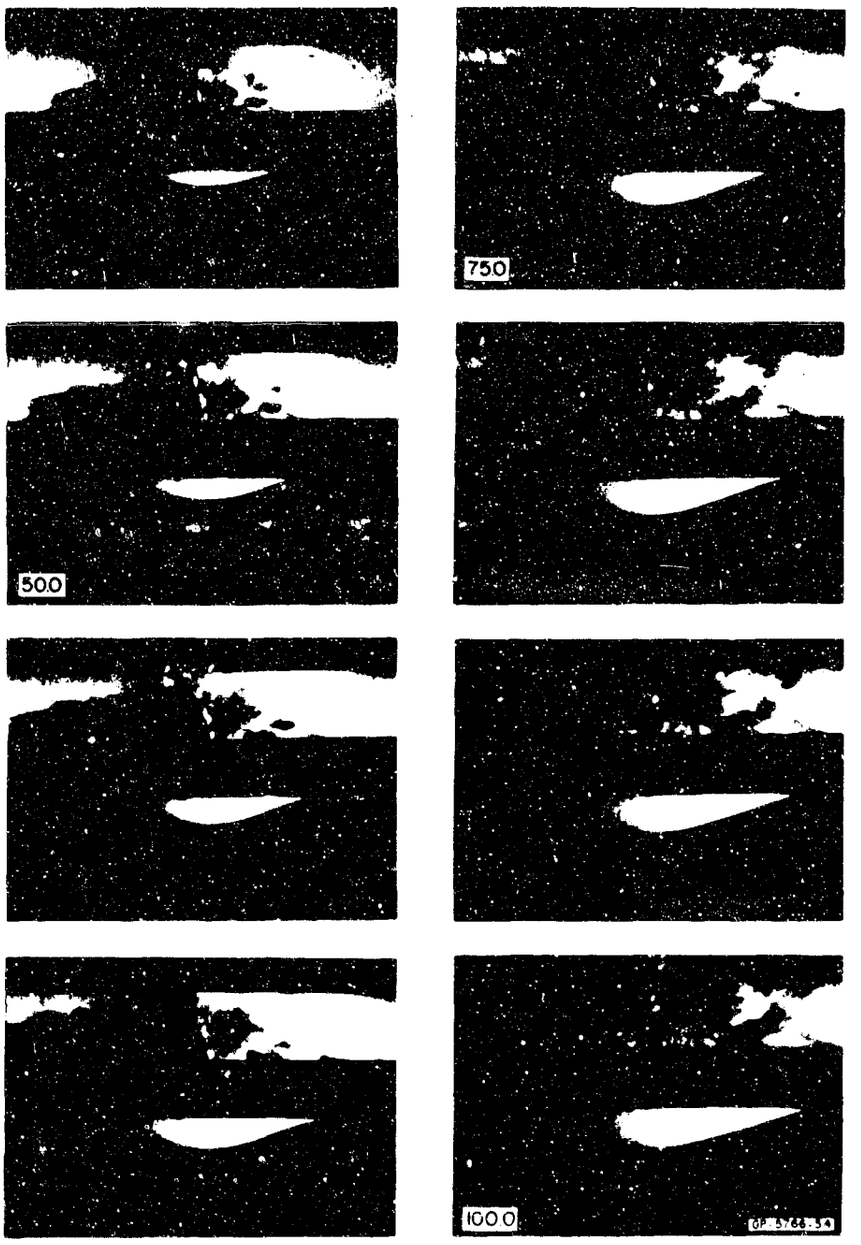

FIG. 25 (Continued)

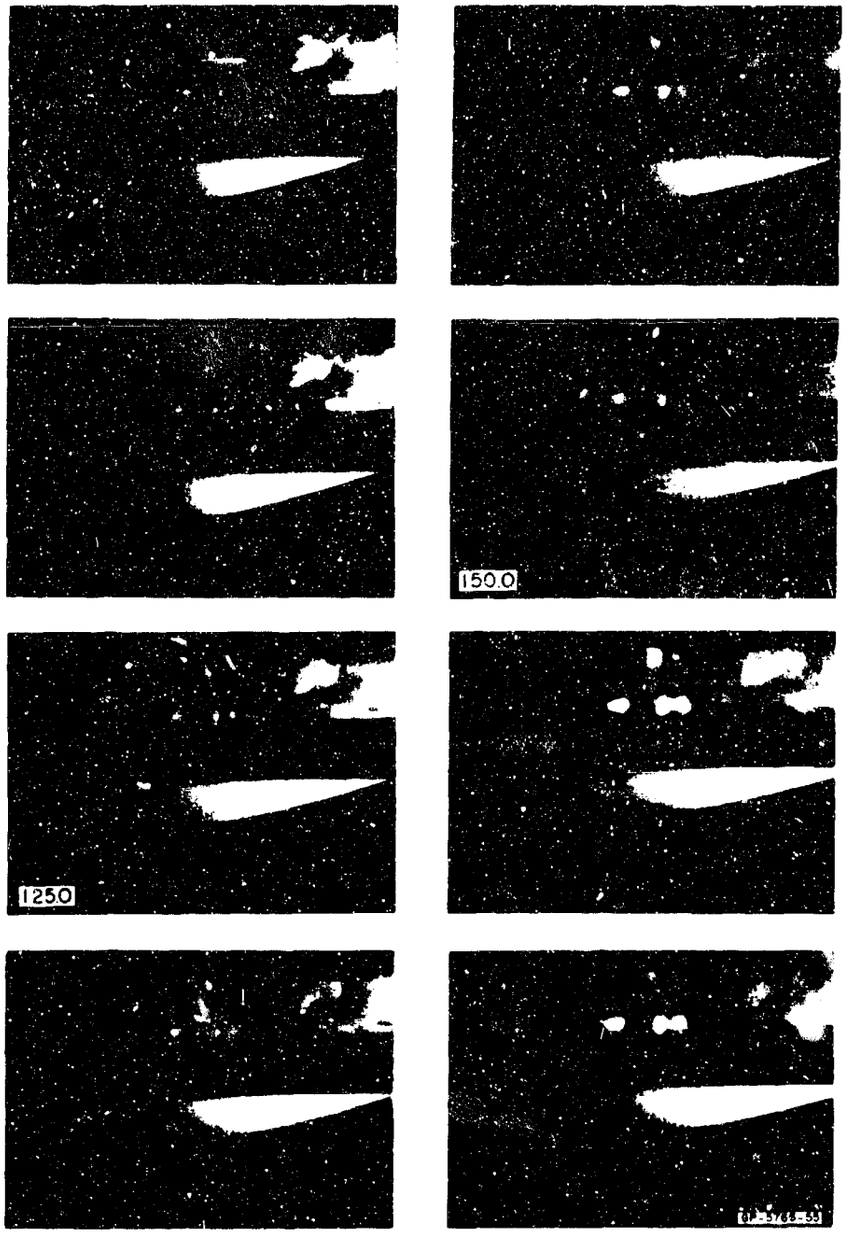

FIG. 25 (Concluded)

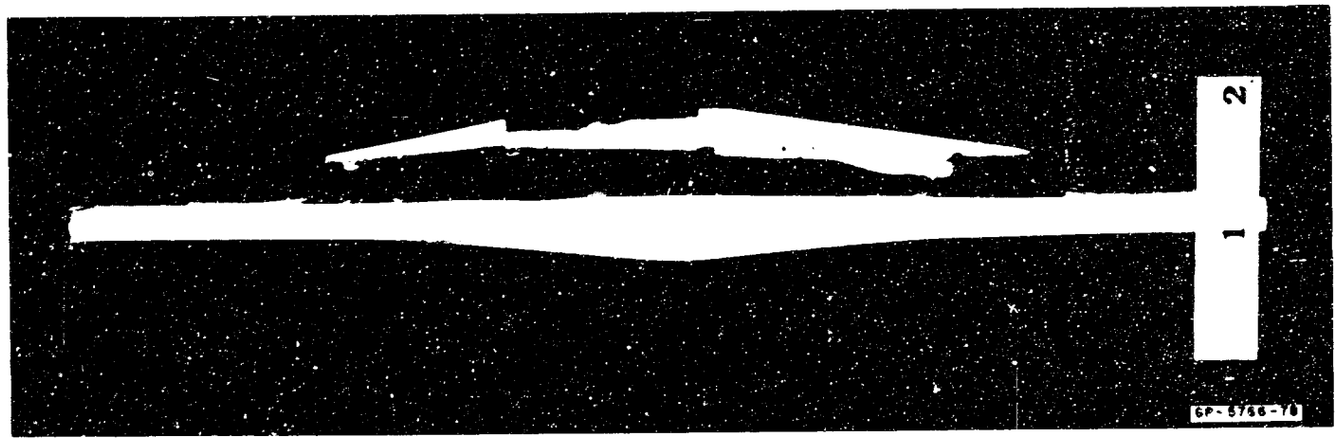

FIG. 26 PROFILE OF CERAMIC-FIBER GLASS COMPOSITE AFTER IMPACT AT 2400 ft/sec WITH 0.3 CALIBER STANDARD AP BULLET

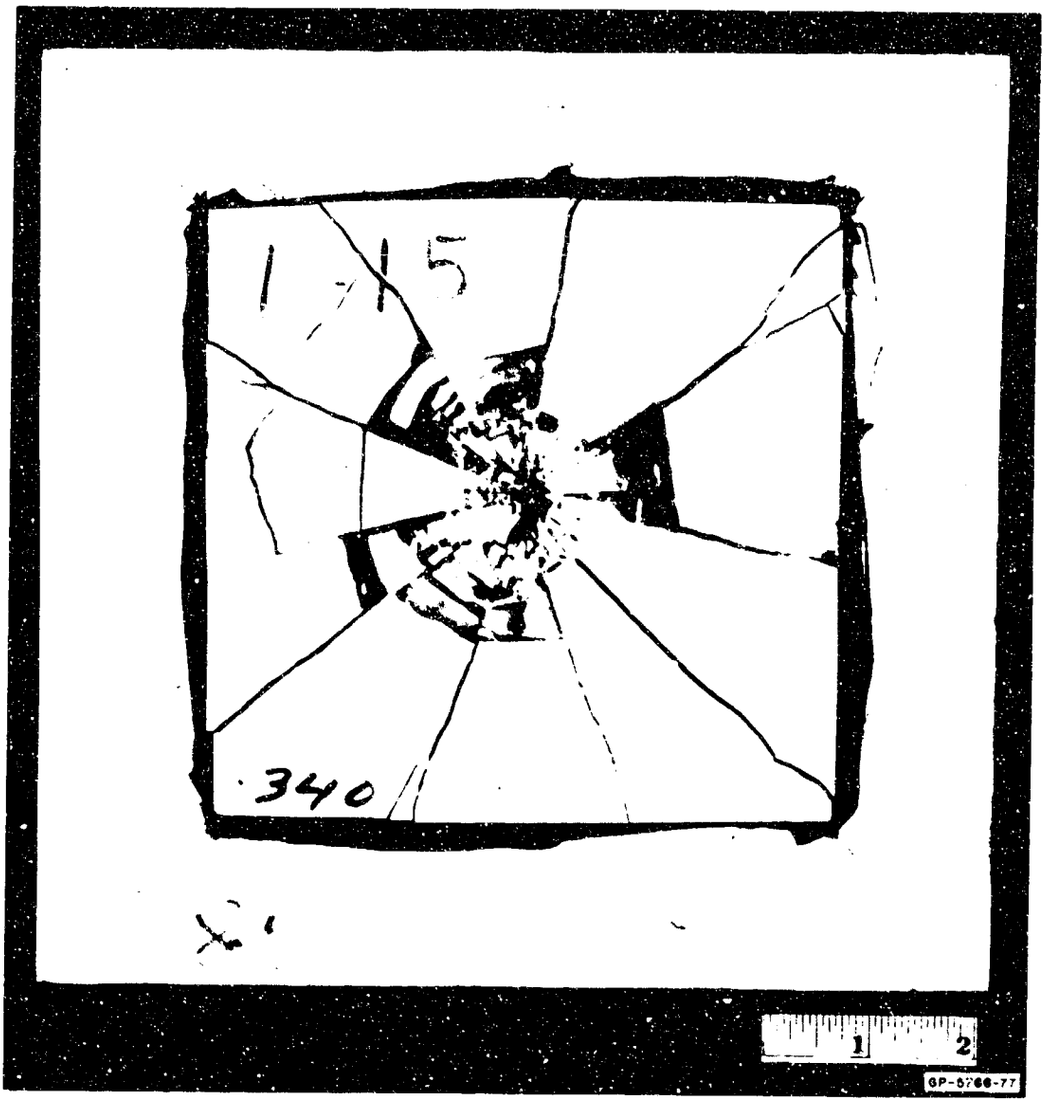

FIG. 27 CERAMIC-FIBER GLASS COMPOSITE AFTER IMPACT AT 2400 ft/sec WITH 0.3 CALIBER STANDARD AP BULLET

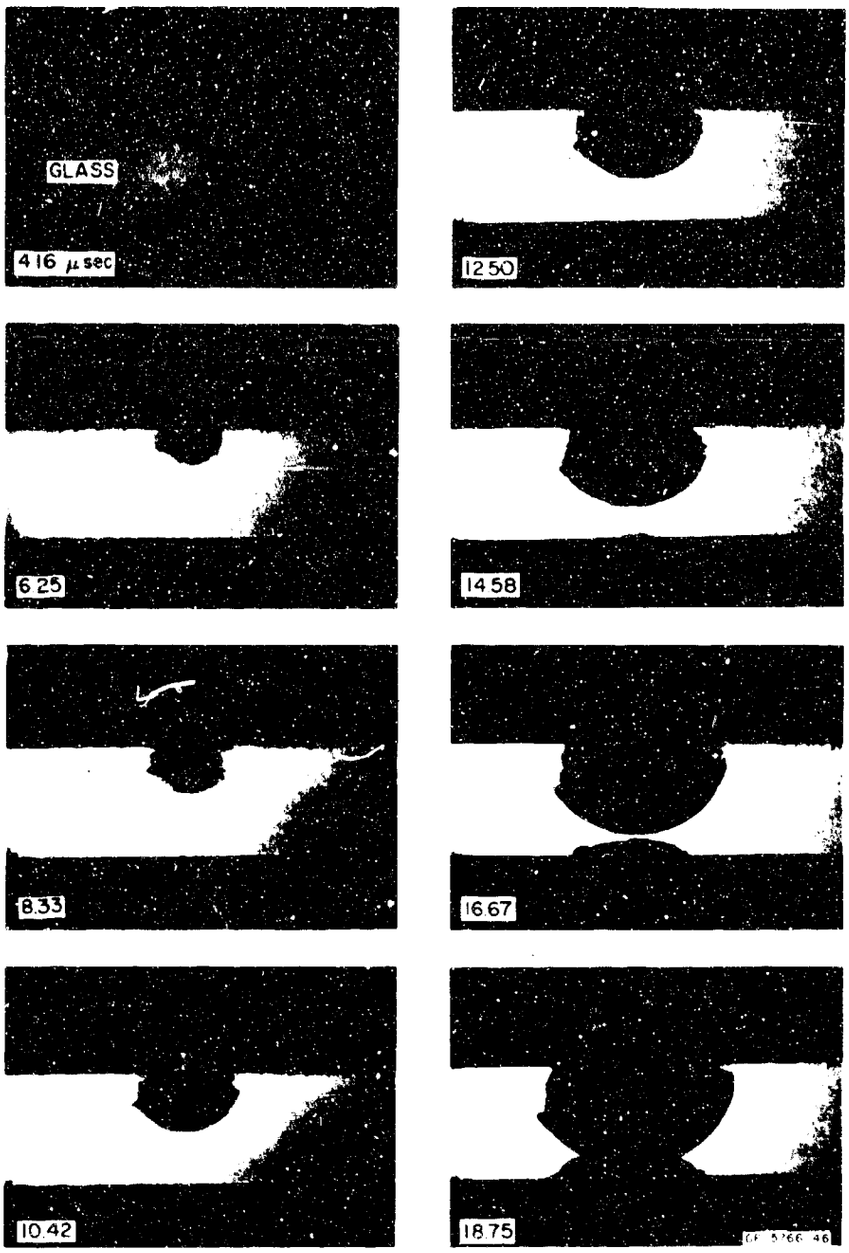

FIG. 28 INTERNAL PROFILE VIEW OF 0.3 CALIBER STANDARD AP BULLET — GLASS BLOCK IMPACT AT 2400 ft sec (2.08 μsec between frames)

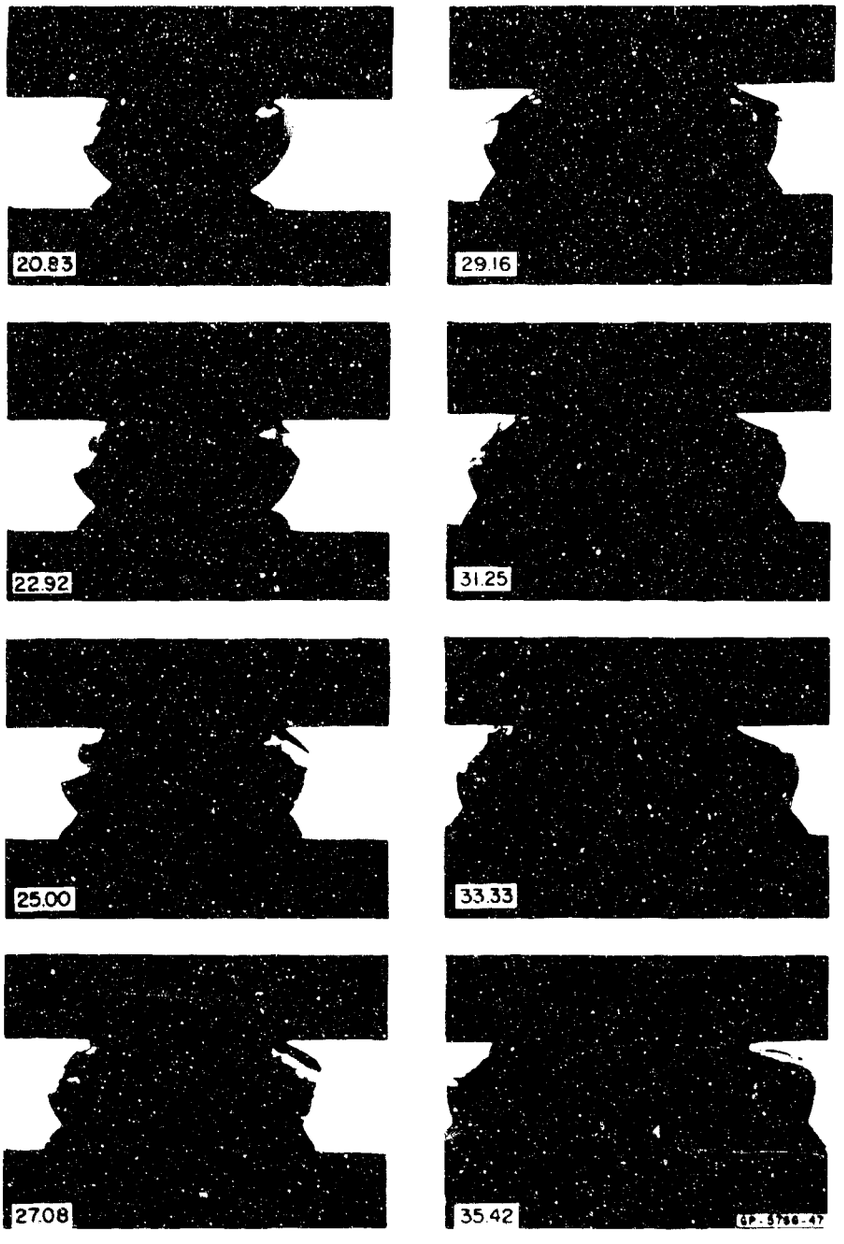

FIG. 28 (Concluded)

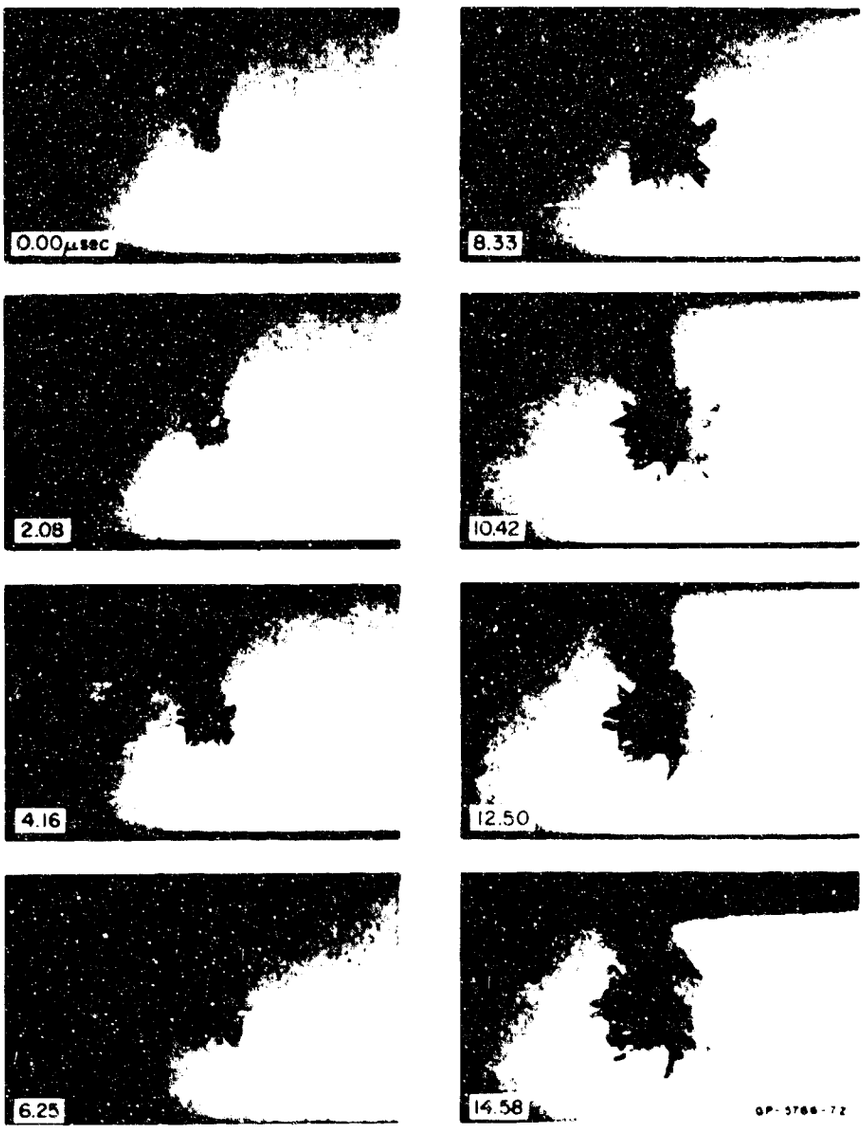

FIG. 29 HEAD-ON VIEW OF 0.3 CALIBER STANDARD AP BULLET — GLASS BLOCK IMPACT AT 2400 ft sec (2.08 μsec between frames)

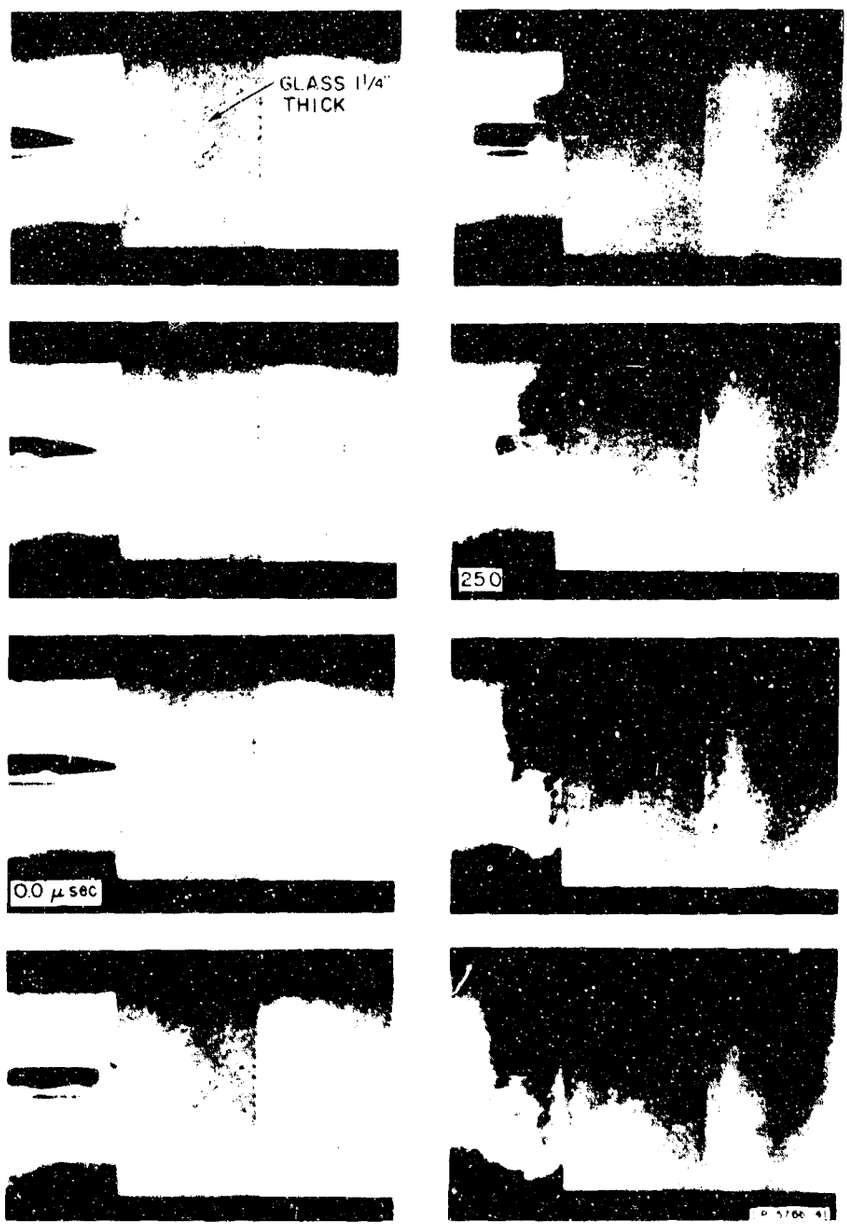

FIG. 30 EXTERNAL VIEW OF 0.3 CALIBER STANDARD AP BULLET — GLASS BLOCK IMPACT AT 2400 ft/sec (8.33 μsec between frames)

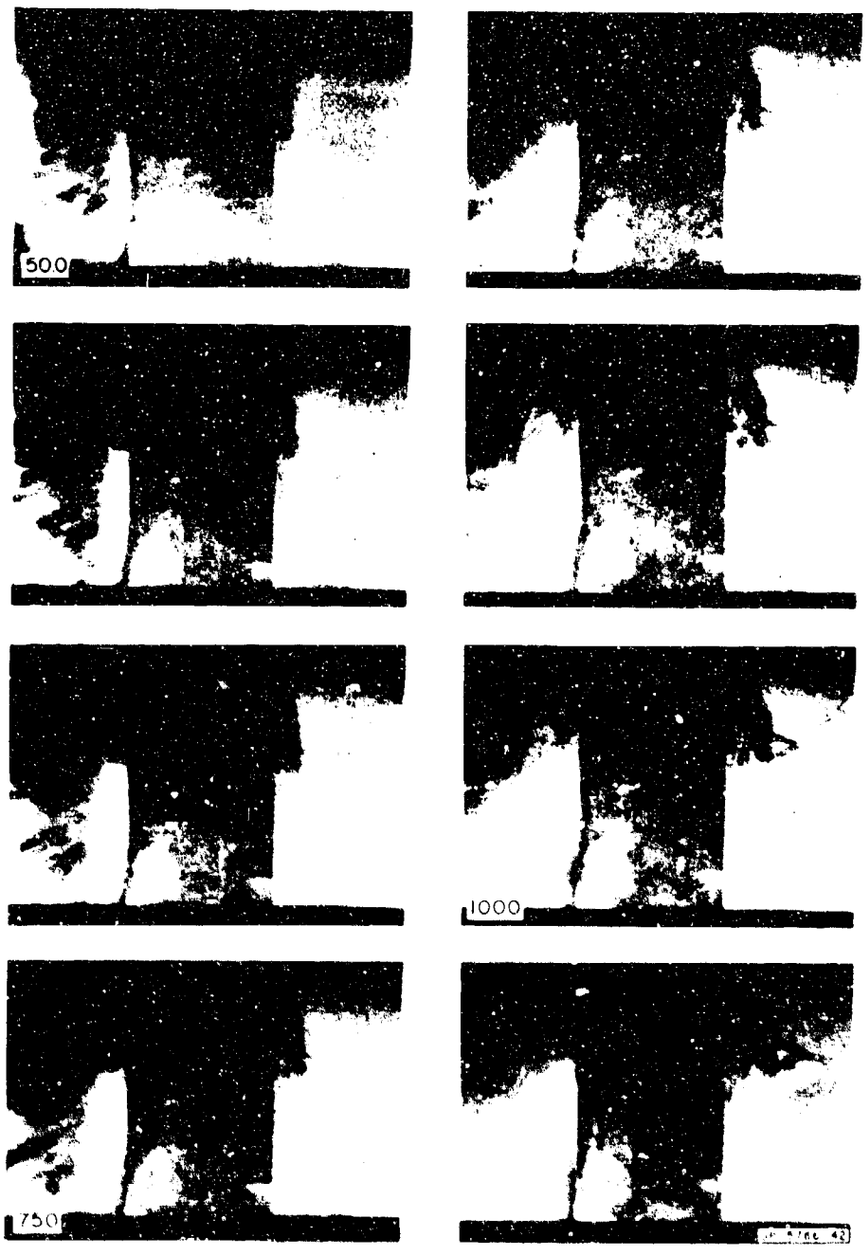

FIG. 30 (Concluded)

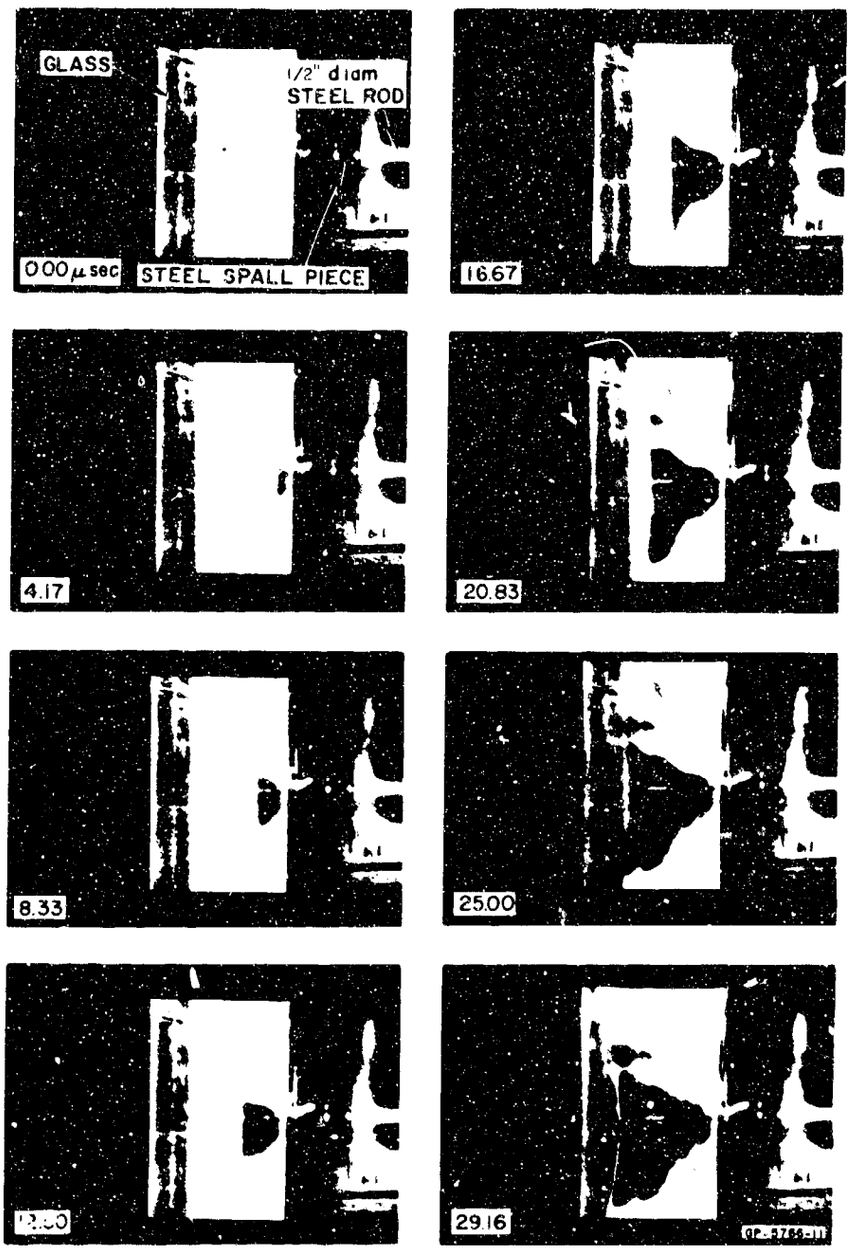

FIG. 31 INTERNAL PROFILE VIEW OF IMPACT OF 0.5-INCH-DIAMETER SPALL PIECE WITH GLASS BLOCK AT 94 ft sec (4.17 μsec between frames)

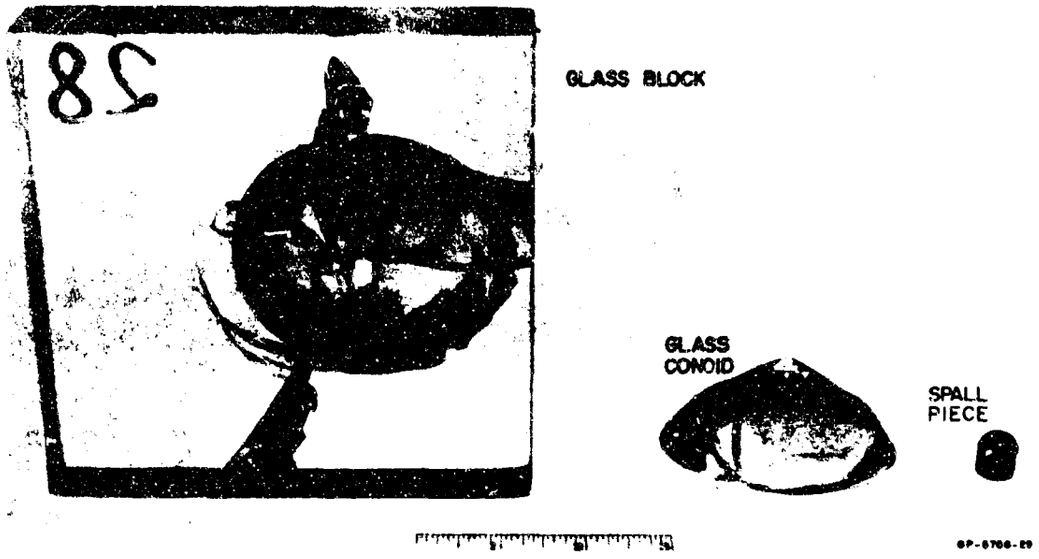

FIG. 32 GLASS BLOCK AFTER IMPACT AT 94 ft/sec WITH A 0.5-INCH-DIAMETER SPALL PIECE

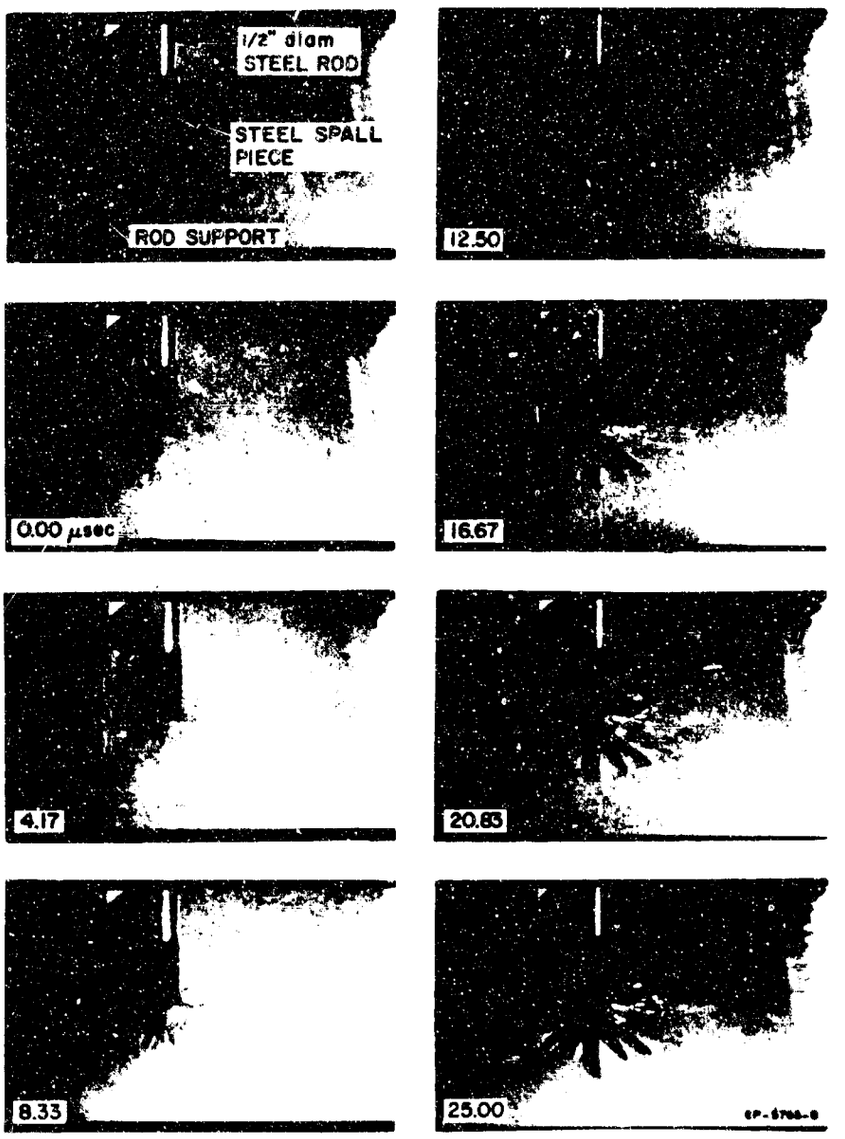

FIG. 33 OBLIQUE FRONT VIEW OF IMPACT OF 0.5-INCH-DIAMETER SPALL PIECE WITH GLASS-MICARTA COMPOSITE (4.17 μsec between frames)

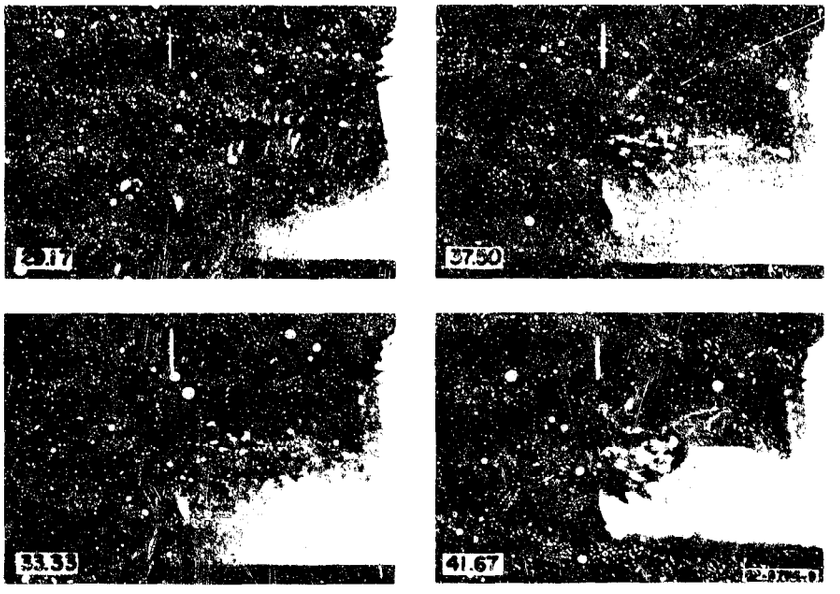

FIG. 33 (Concluded)

FIG. 34 FRACTURE PATTERN IN GLASS PLATE AFTER IMPACT AT 54 ft/sec WITH 0.5-INCH-DIAMETER SPALL PIECE (plate 1/4 inch thick supported on 1/2-inch-thick polyurethane foam)

5. THEORETICAL ANALYSES

A. Introduction

The analyses corresponding to the stress-wave response and structural response concepts (see Section 2) are discussed in this section. It will be recalled that he approach to stress-wave response is to determine the stress waves generated in the facing material considered as a layer, whereas the approach to structural response is to determine the bending moments in the facing material considered as a plate.

To study the stress-wave response, the simplest possible approach is adopted; this is to treat the bullet and the armor facing as if they behave elastically during the impact. Section 8 contains a description of the experimental determination of the elastic limit of a certain form of aluminum oxide under extremely rapid loading. This dynamic elastic limit is as high as 180,000 lb/in^2 and, since the static value is about 30,000 lb/in^2, the assumption of an elastic model is reasonable. To further simplify the model, the bullet is replaced by a cylindrical rod. The appropriate linear equations of elasticity are solved by finite difference technique using Lagrange coordinates [1].

For the study of structural response, the armor is treated as a plate, again assuming elastic behavior. The theory leading to the governing equations is called here the Timoshenko plate theory [2]. It takes into account shear deformation and rotary inertia of plate elements (these are omitted in the Germain-Kirchhoff theory of plates); also, the governing equations are of the hyperbolic type. The problem solved is the response of a plate to a pressure uniformly distributed over a small circular area but varying with time. This pressure should be that at the interface of the bullet and plate, but to obtain an initial description of the plate response a ramp-plateau pressure-time relation is used. Information from the stress-wave response solutions indicates that for early times this pressure input is reasonable.

B. Elasticity Theory

With the notation of Fig. 35 the equations of motion of an element in cylindrical Lagrange coordinates are

$$\frac{\partial \sigma_z}{\partial z} + \frac{\partial \tau_{rz}}{\partial r} + \frac{\tau_{rz}}{r} = \rho \ddot{z} \tag{1}$$

$$\frac{\partial \tau_{rz}}{\partial z} + \frac{\partial \sigma_r}{\partial r} + \frac{\sigma_r - \sigma_\theta}{r} = \rho \ddot{r} \tag{2}$$

where dots refer to time differentiation.

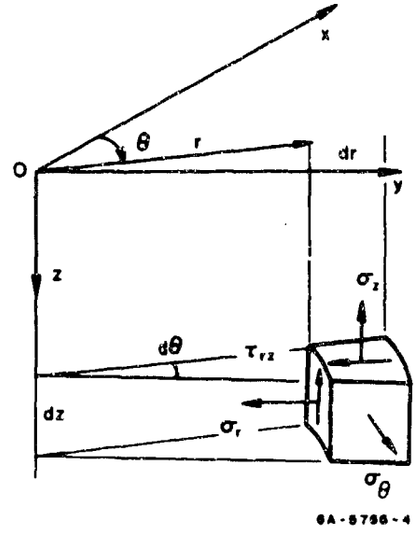

FIG. 35 NOTATION FOR ELASTICITY THEORY

Hooke's law relates the stresses in (1) and (2) to the strains in the following linear manner:

$$\sigma_r = \lambda \Delta + 2\mu \epsilon_r \tag{3}$$

$$\sigma_z = \lambda \Delta + 2\mu \epsilon_z \tag{4}$$

$$\sigma_\theta = \lambda\Delta + 2\mu\epsilon_\theta \qquad (5)$$

$$\tau_{rz} = \mu\gamma_{rz} \qquad (6)$$

In (3) to (6), λ and μ are Lame's material constants and $\Delta = \epsilon_r + \epsilon_z + \epsilon_\theta$ is the dilatation.

Finally, the strains in (3) to (6) are expressible in the following velocity forms:

$$\dot{\epsilon}_r = \frac{\partial \dot{r}}{\partial r} \qquad \dot{\epsilon}_z = \frac{\partial \dot{z}}{\partial z} \qquad \dot{\epsilon}_\theta = \frac{\dot{r}}{r} \qquad \gamma_{rz} = \frac{\partial \dot{r}}{\partial z} + \frac{\partial \dot{z}}{\partial r} \qquad (7)$$

Relations (1) through (7) are used to formulate the problem in finite differences [1] using a mesh in the (r,z) plane.

C. Timoshenko Plate Theory

Figure 36 shows an element of a plate of thickness h acted upon by shearing forces Q, radial and circumferential bending moments M and N, and a pressure p per unit area. (Q, M, and N are values per unit arc length.) The inertia force and couple indicated at the center of the

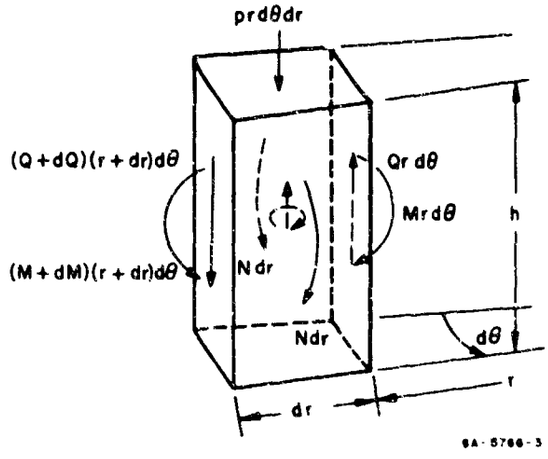

FIG. 36 NOTATION FOR PLATE THEORY

element have magnitudes $\rho h w_{tt}$ and $\rho I \psi_{tt}$ per unit area of plate, where ρ is the material mass density, $I = h^3/12$ is the second moment of area per unit arc length, and w is the element deflection in the direction of the pressure. Throughout this section, the subscripts denote partial differentiation. In plate theory, plane sections are assumed to remain plane, and the plane surface in Fig. 36 at radius r, forming one side of the element, rotates about its intersection with the midsurface of the plate through an angle ψ, which, by convention, is taken positive when its top edge moves outwards.

The equations of motion, moment-curvature relations (from plane sections assumption and Hooke's law), and the shear-deformation relation are

$$(Mr)_r + Qr - N = \rho r I \psi_{tt} \tag{8}$$

$$(Qr)_r + pr = \rho r h w_{tt} \tag{9}$$

$$M = D(\psi_r + \nu\psi/r) \tag{10}$$

$$N = D(\psi/r + \nu\psi_r) \tag{11}$$

$$Q = k'hG(w_r - \psi) \tag{12}$$

where ν is Poisson's ratio, G is the modulus of rigidity, $D = EI/(1 - \nu^2)$ the flexural rigidity (where E = Young's modulus), and $k' = 0.76 + 0.3\nu$ is a constant.

Differentiating (10), (11), and (12) with respect to time and introducing the linear and angular velocities of the element, $v = w_t$ and $\omega = \psi_t$, allows the system (8) through (12) to be written, with matrix notation, in the standard form

$$U_t + AU_r = b \tag{13}$$

where

$$U = \begin{pmatrix} M \\ Q \\ \omega \\ V \\ N \end{pmatrix} \quad A = -\begin{pmatrix} . & . & D & . & . \\ . & . & . & k'Gh & . \\ 1/\rho I & . & . & . & . \\ . & 1/\rho h & . & . & . \\ . & . & \nu D & . & . \end{pmatrix} \quad b = \begin{pmatrix} \nu D\omega/r \\ -k'Gh\omega \\ (M + Qr - N)/\rho Ir \\ (Q + pr)/\rho hr \\ D\omega/r \end{pmatrix}$$

The matrix equation (13) represents a linear system of first-order hyperbolic partial differential equations having the characteristic condition $|A - \lambda_i I| = 0$ where $\lambda = dr/dt$ and I is the identity matrix. This condition yields the values $\lambda = 0, \pm c_p, \pm c_s$ where $c_p^2 = E/\rho(1 - \nu^2)$ and $c_s^2 = k'G/\rho$.

To transform (13) into the normal form (differentiation along the characteristics), which is the form required for computations, the left-hand null vector $\ell_{(i)}$ for each λ_i is found from the set of homogeneous algebraic equations $\ell_i(A - \lambda_i I) = 0$. Then, the required transformation matrix T is that matrix having as its rows the vectors $\ell_{(i)}$. In (13), set $U = T^{-1}V$, $(V = TU)$ and post multiply by T to give the desired normal form

$$V_t + DV_x = Tb \tag{14}$$

where the matrix D is diagonal with elements λ_i, that is, $D = TAT^{-1}$ $= \text{diag}\,(\lambda_1, \lambda_2, \ldots \lambda_n)$.

The normal system (14) may also be written as

$$(\partial/\partial t + \lambda_i \partial/\partial x)V_i = \ell_{(i)} b \tag{15}$$

where the V_i are elements of the column vector V.

For the present problem, in terms of the dimensionless variables defined below, the system (15) is

$$\left(\frac{\partial}{\partial\tau} + \frac{\partial}{\partial\xi}\right)(\bar{M} - \bar{\omega}) = \frac{\nu}{\xi}\bar{\omega} - \frac{1}{\xi}(\bar{M} - \bar{N}) - \bar{Q} \qquad \text{along } \frac{d\tau}{d\xi} = 1$$

$$\left(\frac{\partial}{\partial\tau} - \frac{\partial}{\partial\xi}\right)(\bar{M} + \bar{\omega}) = \frac{\nu}{\xi}\bar{\omega} + \frac{1}{\xi}(\bar{M} - \bar{N}) + \bar{Q} \qquad \text{along } \frac{d\tau}{d\xi} = -1$$

$$\left(\frac{\partial}{\partial\tau} + \frac{\partial}{\beta\partial\xi}\right)(\bar{Q} - \bar{V}) = -\frac{12}{\beta^2}\bar{\omega} - \frac{\bar{Q}}{\beta\xi} - \frac{\bar{p}}{\beta} \qquad \text{along } \frac{d\tau}{d\xi} = \frac{1}{\beta}$$

$$\left(\frac{\partial}{\partial\tau} - \frac{\partial}{\beta\partial\xi}\right)(\bar{Q} + \bar{V}) = -\frac{12}{\beta^2}\bar{\omega} + \frac{\bar{Q}}{\beta\xi} + \frac{\bar{p}}{\beta} \qquad \text{along } \frac{d\tau}{d\xi} = -\frac{1}{\beta}$$

$$\frac{\partial}{\partial\tau}\left(\bar{M} - \frac{\bar{N}}{\nu}\right) = -\frac{1 - \nu^2}{\nu\xi}\bar{\omega} \qquad \text{along } \frac{d\tau}{d\xi} = \infty$$

where

$$\xi = r/h \qquad \tau = c_p t/h \qquad \bar{M} = Mh/D \qquad \bar{Q} = Qh^2/D \qquad \bar{\omega} = h\omega/c_p$$

$$\bar{V} = 12c_s V/c_p^2 \qquad \bar{N} = Nh/D \qquad \bar{p} = ph^3/D \qquad \beta = c_p/c_s$$

Each of these five equations is put into finite difference form and the usual numerical scheme for advancing along the characteristics in the ξ, τ plane is carried out. At a normal point this involved solving five algebraic equations for the five unknowns $\bar{M}$, $\bar{Q}$, $\bar{\omega}$, $\bar{V}$, $\bar{N}$.

6. THEORETICAL RESULTS AND OBSERVATIONS

A. Introduction

In this section are presented some of the results that have been obtained from the elasticity and plate theories of Section 5. Only those theoretical results leading to observations which bear directly on the experimental observations are included.

B. Elasticity Theory

Stress fields have been obtained numerically for the following two cases:

1. A steel cylindrical rod of 0.25-inch diameter striking a glass layer 1-1/4 inches thick at 94 ft/sec.
2. A steel cylindrical rod of 0.2-inch diameter striking a ceramic layer 0.3 inch thick at 1750 ft/sec.

Case 1: For the four times indicated, Fig. 37 shows the fields of tensile hoop stress σ_θ in a glass block in the form of a distribution of dots. Each dot is located in the r,z plane at the center of each member or cell of a mesh whenever the tensile hoop stress exceeds 2000 lb/in^2. In its original unstressed state each cell is a square, 0.025 inch to a side (Physically, each cell is a cross section of a ring of material with its center on the axis of symmetry.) If the glass fractures whenever the hoop stress exceeds 2000 lb/in^2, the fracture field will occupy the dotted region provided the waves caused by the formation of fracture are not strong enough to greatly disturb the tensile hoop stress field at its expanding front.

For the same four times, Fig. 38 shows the fields of the tensile principal stresses, denoted by σ, in the form of short lines, one or two for each cell. The principal stresses act in the r,z plane perpendicular to the lines, each of which represents an elemental surface of revolution about the r axis. Lines are shown whenever the tensile stress exceeds 2000 lb/in^2; they indicate the most likely fracture surfaces of revolution.

By comparing Figs. 37 and 38 it can be seen that the two tensile stress fields occupy almost the same space at each time; this space grows with time and its front or outer boundary lags farther and farther behind the elastic wave front (shown dashed in the figures). Numerical results reveal that the stress field just behind the stress wave front is compressive, with stress magnitudes which decrease as the front expands into the glass. This means that at any point in the material, a stress environment conducive to fracture will not exist until some time after the wave front has passed that point. This phenomenon, together with the usual delay before fractures become apparent, corresponds to experimental observations of fracture fronts moving at about 0.3 times the dilatational wave velocity for glass (see Sections 4C, D, G, and H).

The rapid development of a tensile stress field with at least two orthogonal principal components greatly exceeding the fracture stress is conducive to comminution. At the front surface of the glass block, the field of the tensile principal stress component σ (Fig. 38) is more extensive than the field of the tensile hoop stress σ_θ (Fig. 37). Also σ is considerably greater than σ_θ there. Thus the tendency is to form more circular cracks than radial cracks at the front surface in the vicinity of the impact zone.

Figures 39 and 40 show the effect of raising the assumed dynamic fracture stress from 2000 lb/in^2 to 4000 lb/in^2. By comparing these figures with Figs. 37 and 38, it can be seen that the tensile stress fields are smaller at a given time. Also, the front of the tensile stress field moves more slowly. At the front surface of the glass, the tensile stress field consists primarily of the principal stress σ, which is responsible for circular cracks.

Case 2: For the times indicated, Figs. 41 and 42 show the fields of tensile hoop stress σ_θ and tensile principal stresses σ in a ceramic layer. They are depicted in a manner similar to that for the glass block, except that dots and short lines are shown whenever σ_θ and σ

are greater than 50,000 lb/in^2. Wave reflections from the back surface occur after time $t = 0.81$ μsec, and the diagrams at times $t = 0.91$ and 1.09 μsec indicate that the wave front and the following tension field range from the top to the bottom surfaces as they expand.

Many of the observations made for Case 1 also hold for Case 2. This is expected, because, apart from the regions of large deformations around the edge of the impact zone, the mathematical model is essentially linear-elastic. Figures 41 and 42 show that the two tensile stress fields of σ_θ and σ occupy almost the same space at each instant. This space grows with time in such a manner that its outer boundary lags farther and farther behind the elastic wave front. Again numerical results reveal that the stress field immediately behind the elastic wave front is compressive with stress magnitudes which decrease as the front expands. Thus, a stress environment conducive to fracture will not exist at a point in the ceramic until some time after the wave front has passed that point. This phenomenon, together with the delay before fracture occurs and becomes visible, accounts qualitatively for the fractures being observed in experiments only after the elastic wave front has traveled some considerable distance (see Sections 4C, D, G, and H).

As in Case 1, a tensile stress field with at least two orthogonal principal stress components greatly exceeding the fracture stress is conducive to comminution. At the rear surface of the ceramic, Figs. 41 and 42 depict the tensile hoop stress σ_θ spreading radially ahead of the tensile principal stress σ, thereby indicating a preference for radial cracking during the initial stages of breakup, as is indeed observed experimentally in Figs. 9 and 22. At the front surface near the impact zone there are regions where the three principal tensile stress components are large and so approximate a state of hydrostatic tension. This state is conducive to ejection of ceramic around the projectile, as observed experimentally in Figs. 7, 8, 20, and 21.

Figures 43 and 44 show the effect of doubling the assumed dynamic fracture stress. By comparing these figures with Figs. 41 and 42, it can be seen that the tensile stress fields are smaller at any given time. Also, the front of the tensile stress field moves more slowly. At the front surface of the ceramic, the field consists primarily of the principal stress σ, which is responsible for circular cracks.

The dynamic fracture stress of ceramic is unknown, but the chosen values serve adequately for a qualitative account of the response of a ceramic facing plate. It is known that the elastic limit is dependent upon strain rate [3], and to obtain the sensitivity to strain rates of the magnitude encountered under impact conditions, the work of Section 8 was carried out.

C. Timoshenko Plate Theory

Results are presented in the forms of Figs. 45, 46, and 47 to show qualitatively how the deflections and bending moments vary while an infinite plate is subjected to a ramp-plateau pressure-time pulse uniformly distributed over a small circular area.

All physical quantities are referred to in terms of the dimensionless quantities listed at the end of Section 5C. In the numerical example from which Figs. 45-47 stem, the rise time or ramp duration is $\tau = \tau_o = 2.0$ and the radius of the loaded circle is $\xi = \xi_o = 0.4$. The former value means that the bending wave front, moving at a velocity c_p (the so-called plate velocity), traverses a distance equal to two plate thicknesses while the pressure rises to its full value. The latter value means that the radius of the loading circle is 4/10 of the plate thickness. The plateau pressure, for numerical convenience only, is taken as $\bar{p} = 1.0$ and Poisson's ratio, which is the only physical parameter on which the dimensionless results depend, is taken to be $\nu = 0.25$, a value corresponding to those for glass and ceramic.

Figure 45 shows the plate deflection $\bar{y} = y/h$ at five equally spaced times. The central deflection grows rapidly and there is an expanding annular region in which the deflection is actually in the opposite direction to the applied pressure.

Figure 46 shows the radial bending moment $\bar{M}$ at the same five times. Note the rapid increases of bending moment magnitudes in a circular region at the plate center and in an expanding annular region which itself moves away from the center. The moments in these two regions are opposite in sign. Figure 47 shows a similar behavior for the circumferential bending moment $\bar{N}$, except that in the annular region the moments are much smaller in magnitude than $\bar{M}$ (at $\tau = 10$, $\bar{M} \approx 6\bar{N}$). At the plate center $\bar{M} = \bar{N}$ and the magnitude of $\bar{N}$ decreases less slowly than that of M as ξ increases. This last observation means that, should the fracture stress or fracture bending moment be exceeded at the plate center, the stress or moment environment would require vertical radial cracks at the bottom surface where the stresses are tensile. If the fracture moment is exceeded in the expanding annular region, only a circumferential crack appears since $\bar{M}$ is considerably greater than $\bar{N}$. These predictions of fracture locations are in agreement with the final crack pattern in impact experiments on thin glass plates as illustrated by Fig. 34.

One difference must be noted between these qualitative predictions of fracture locations and experimental observations. High speed photography often shows the formation and growth of the central radial cracks before the formation of a circumferential crack (see Fig. 33). This points up the need for further analysis to describe the phenomenon more accurately. However, it can be stated that a weakening of the plate at the center serves to encourage formation of a circumferential crack. This is an important mechanism because once the circumferential crack has formed the outer portion of the plate no longer participates in containing the applied pressure.

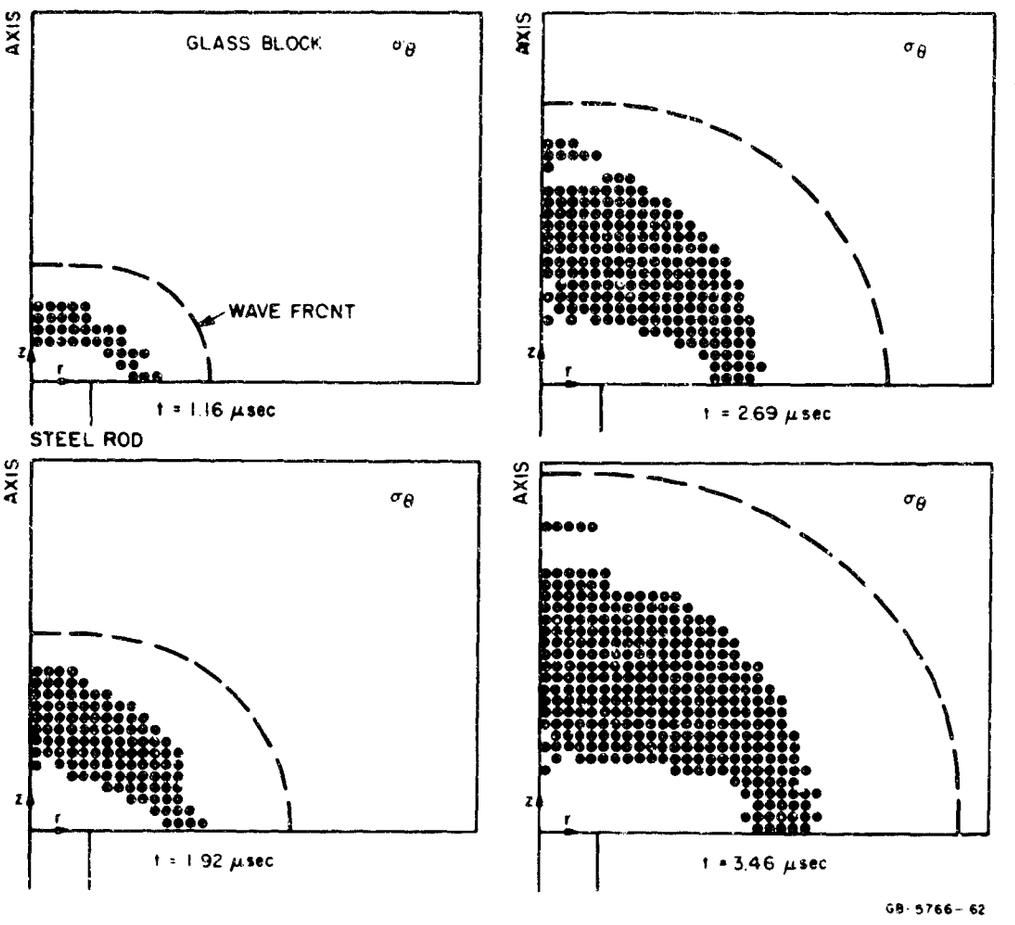

FIG. 37 FIELDS OF TENSILE HOOP STRESS IN A GLASS BLOCK
(σ_θ = 2000 lb in^2 – impact velocity 94 ft sec)

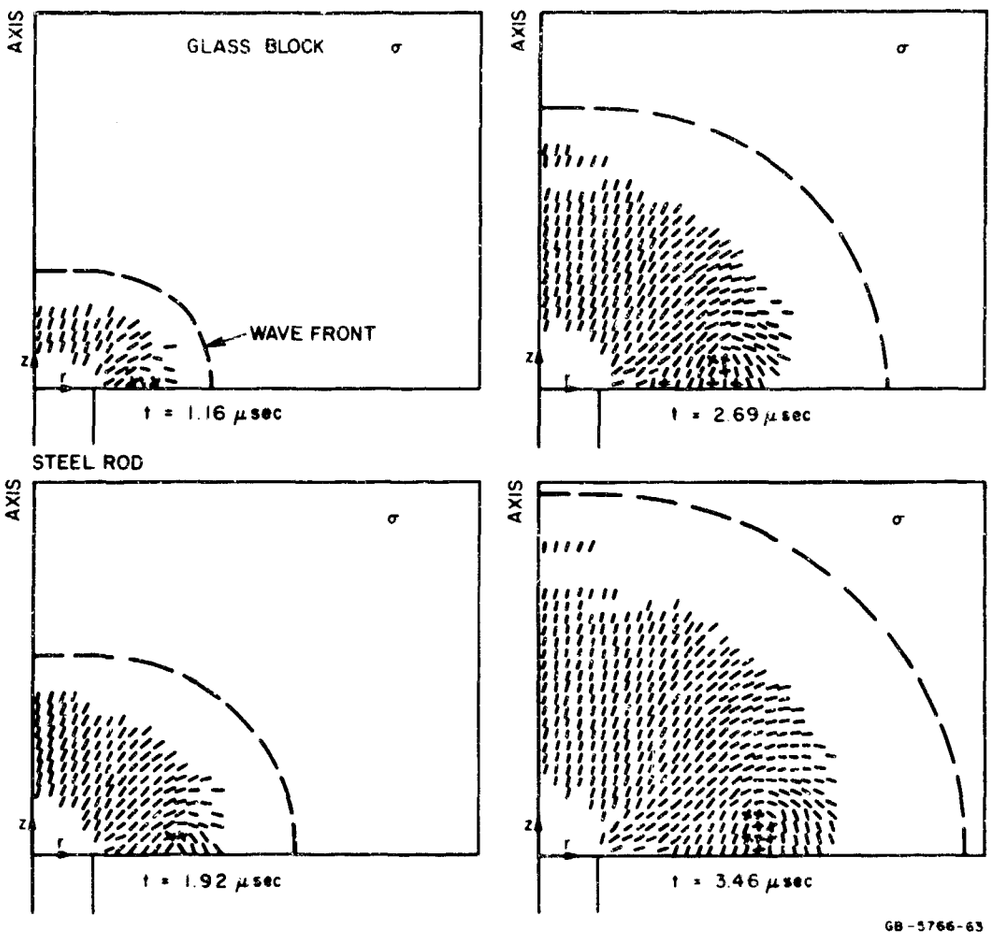

FIG. 38 FIELDS OF TENSILE PRINCIPAL STRESS IN A GLASS BLOCK
(σ = 2000 lb/in^2 – impact velocity 94 ft/sec)

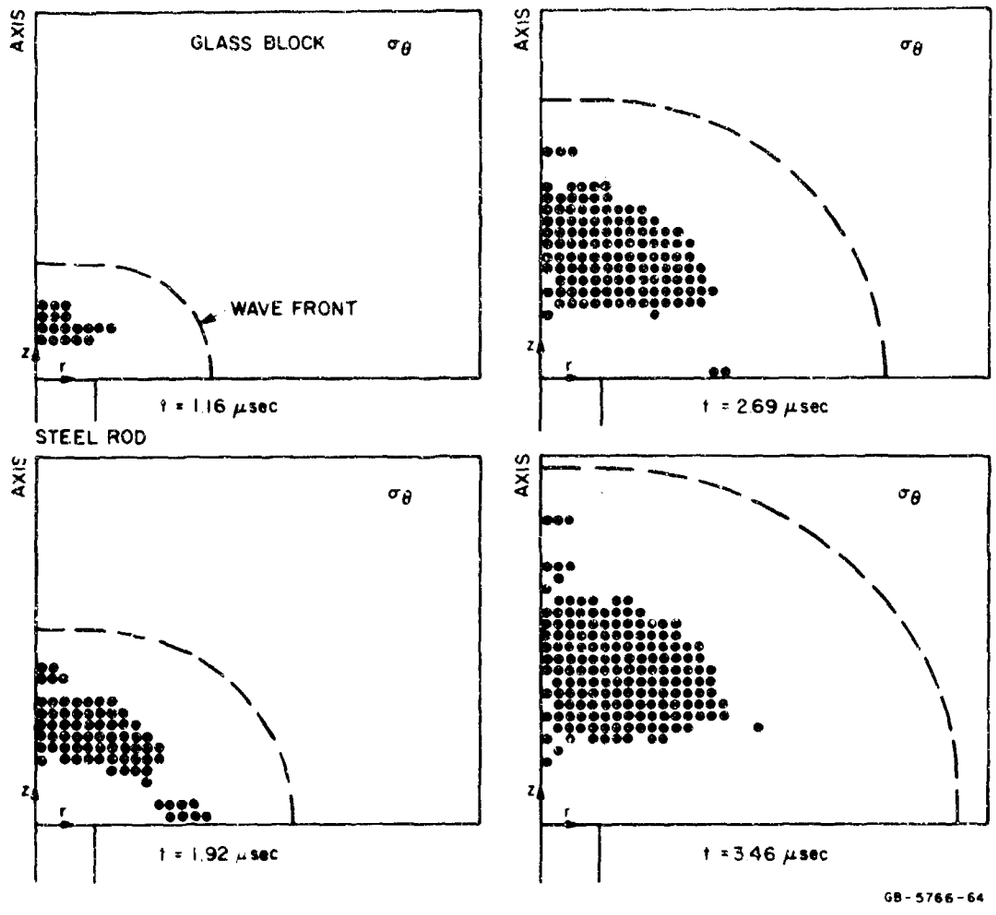

FIG. 39 FIELDS OF TENSILE HOOP STRESS IN A GLASS BLOCK
(σ_θ · 4000 lb in^2 – impact velocity 94 ft sec)

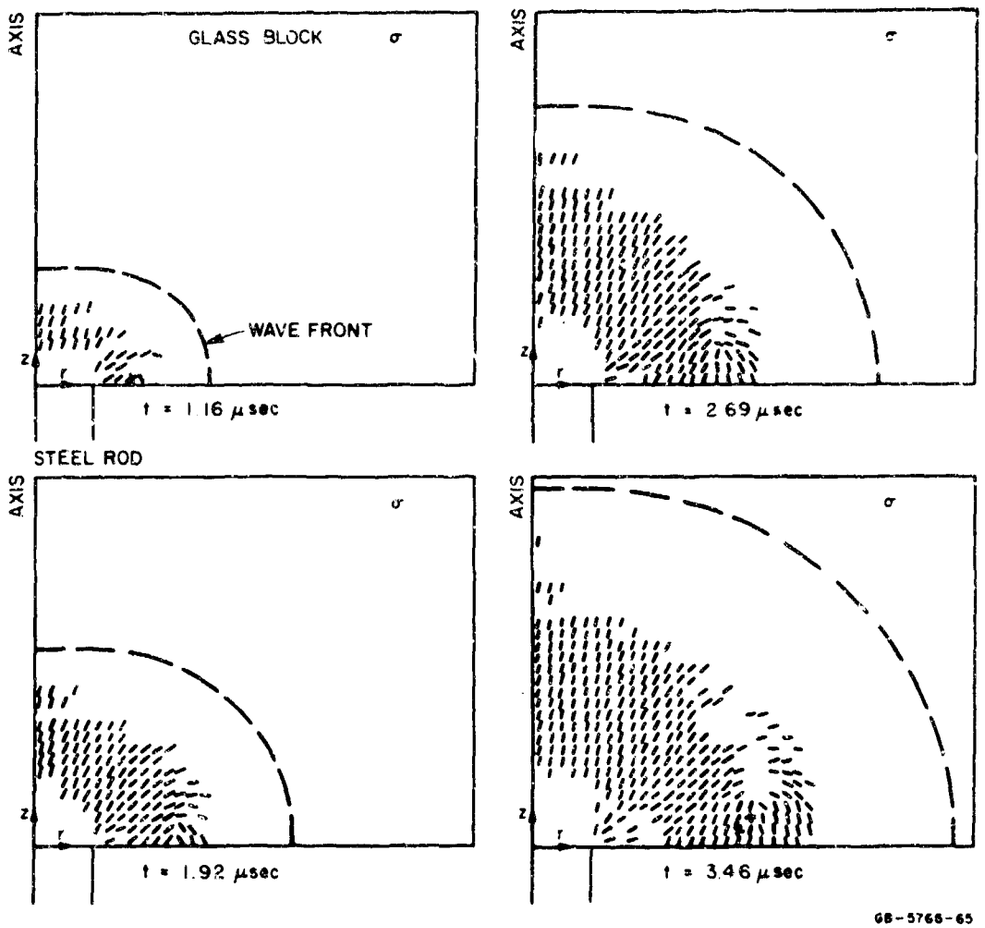

FIG. 40 FIELDS OF TENSILE PRINCIPAL STRESS IN A GLASS BLOCK
(σ · 4000 lb/in^2 – impact velocity 94 ft/sec)

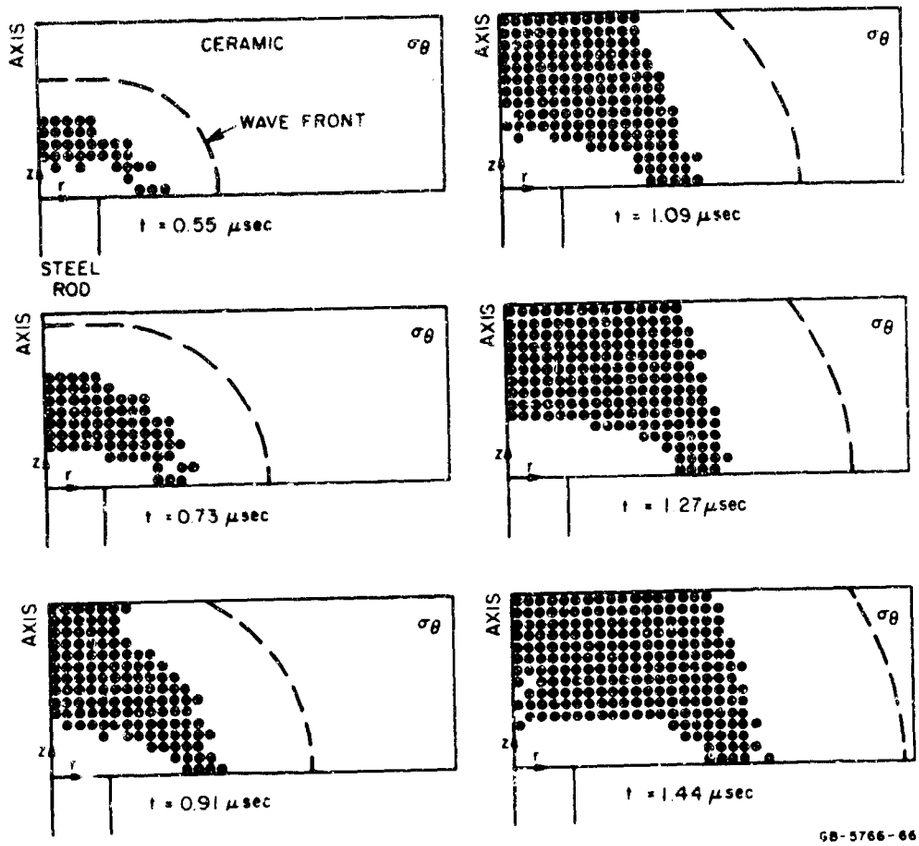

FIG. 41 FIELDS OF TENSILE HOOP STRESS IN A CERAMIC LAYER
(σ_θ - 50,000 lb in^{-2} – impact velocity 1750 ft sec)

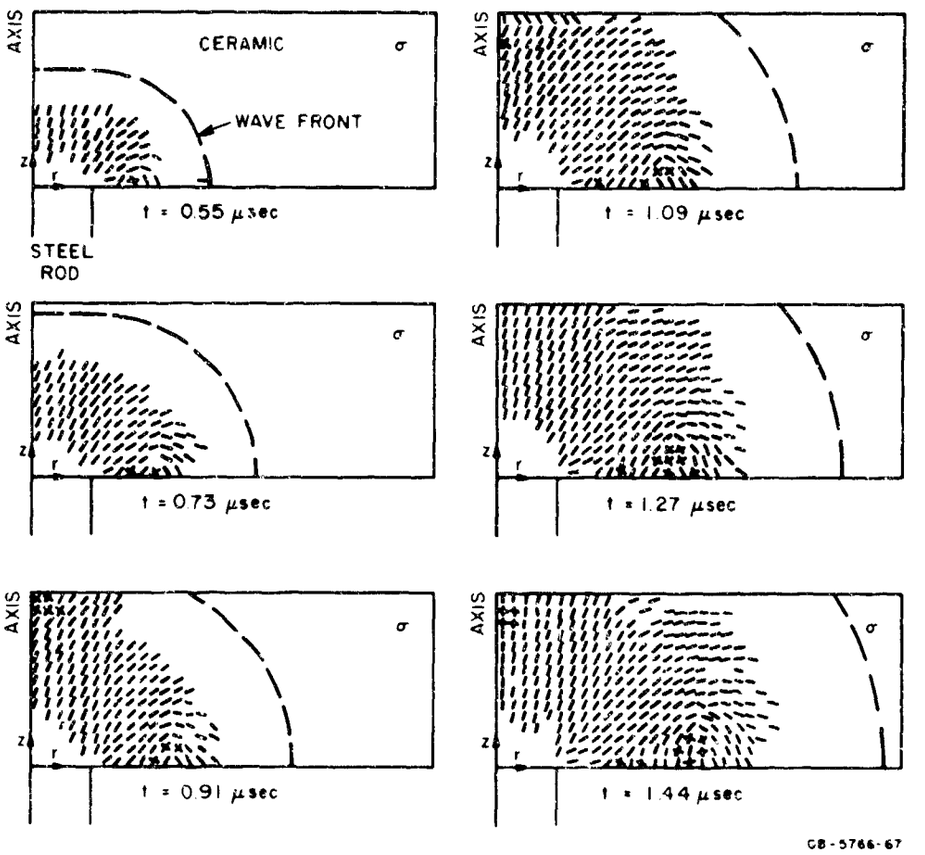

FIG. 42 FIELDS OF TENSILE PRINCIPAL STRESS IN A CERAMIC LAYER
(σ · 50,000 lb in^2 – impact velocity 1750 ft sec)

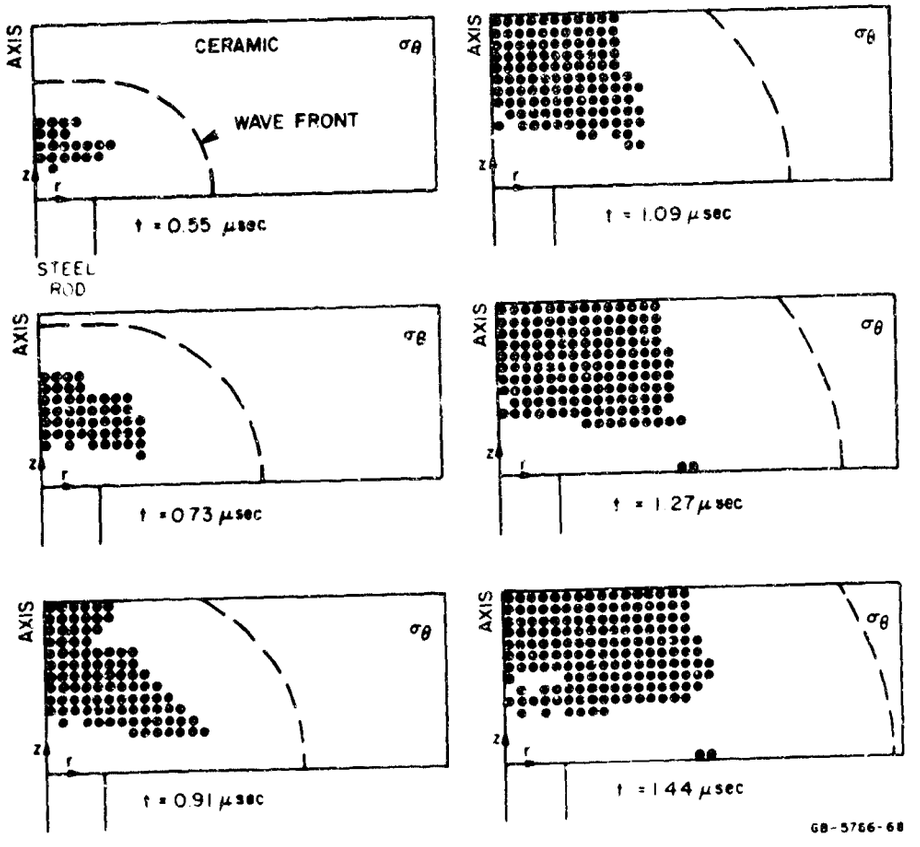

FIG. 43 FIELDS OF TENSILE HOOP STRESS IN A CERAMIC LAYER
(σ_θ · 100,000 lb in^2 – impact velocity 1800 ft sec)

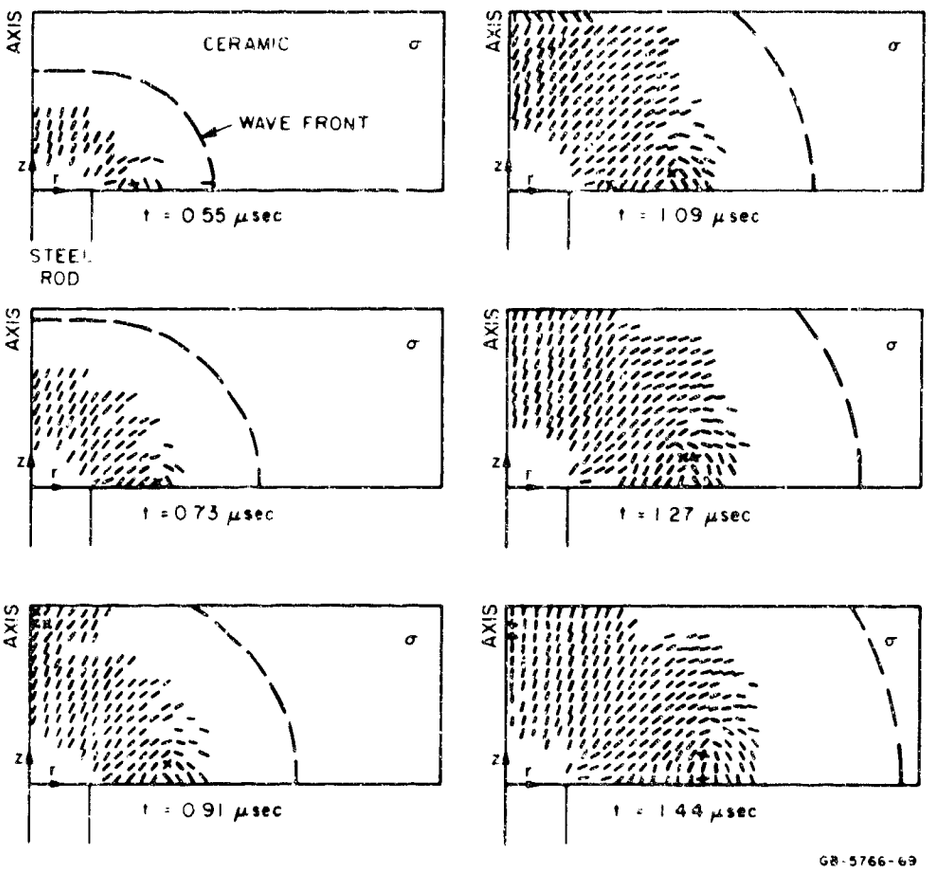

FIG. 44 FIELDS OF TENSILE PRINCIPAL STRESS IN A CERAMIC LAYER
(σ = 100,000 lb/in^2 – impact velocity 1750 ft/sec)

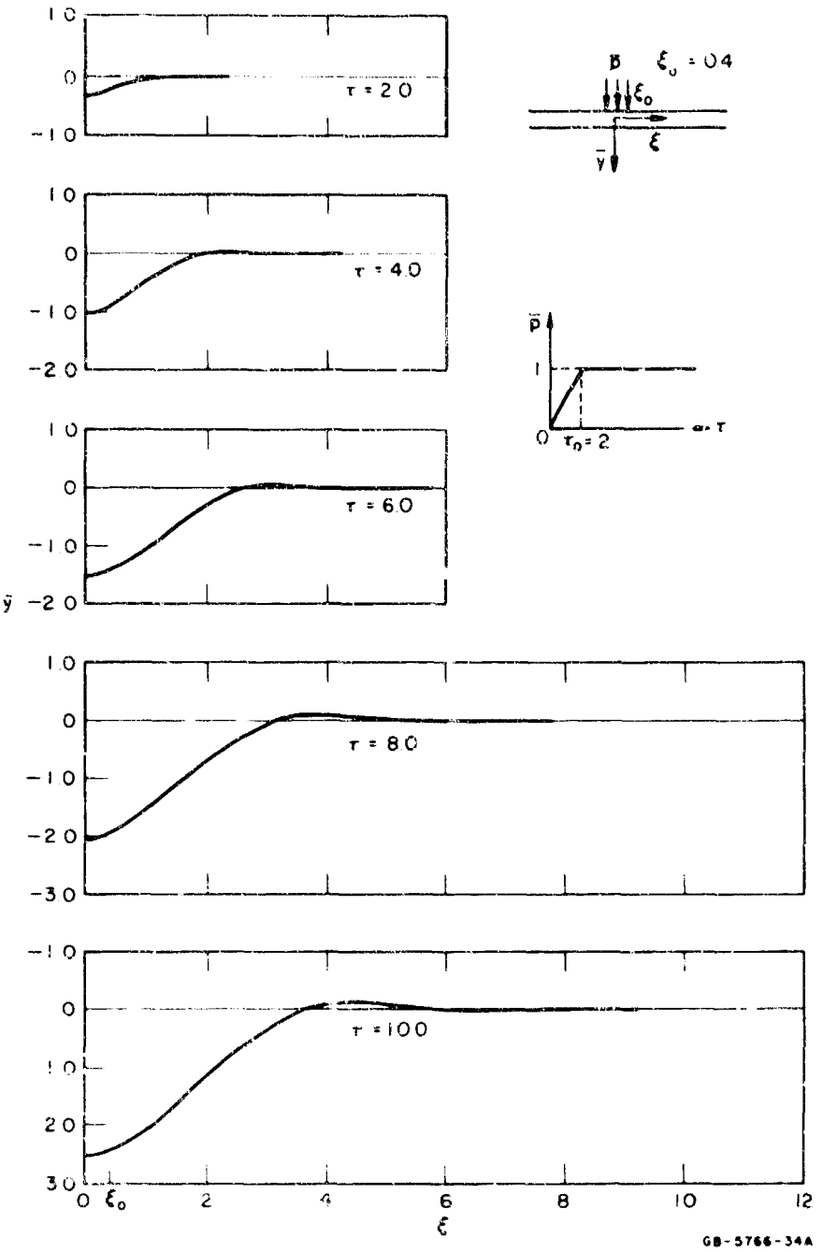

FIG. 45 DIMENSIONLESS DEFLECTION OF PLATE

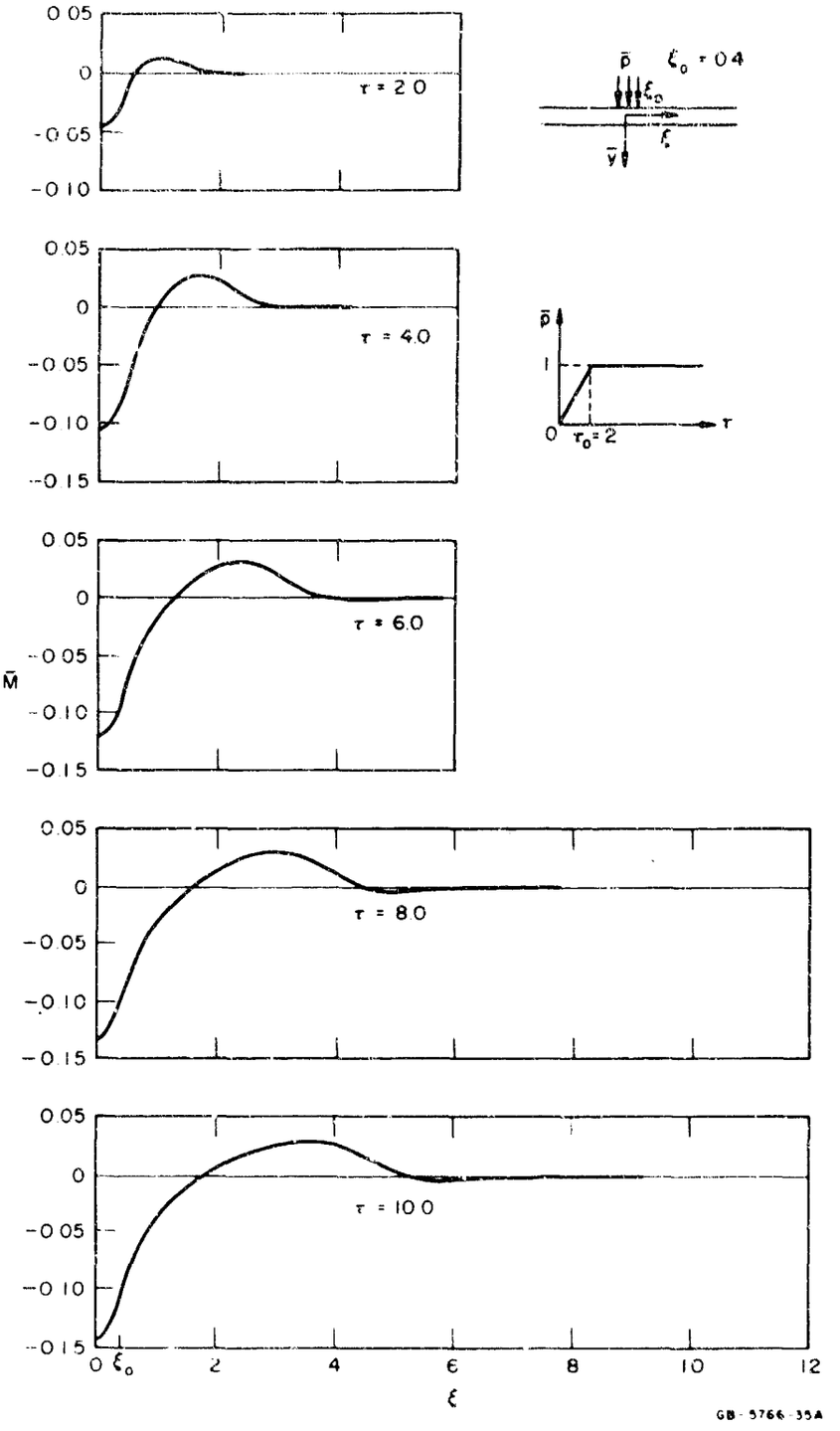

FIG. 46 DIMENSIONLESS RADIAL BENDING MOMENT OF PLATE

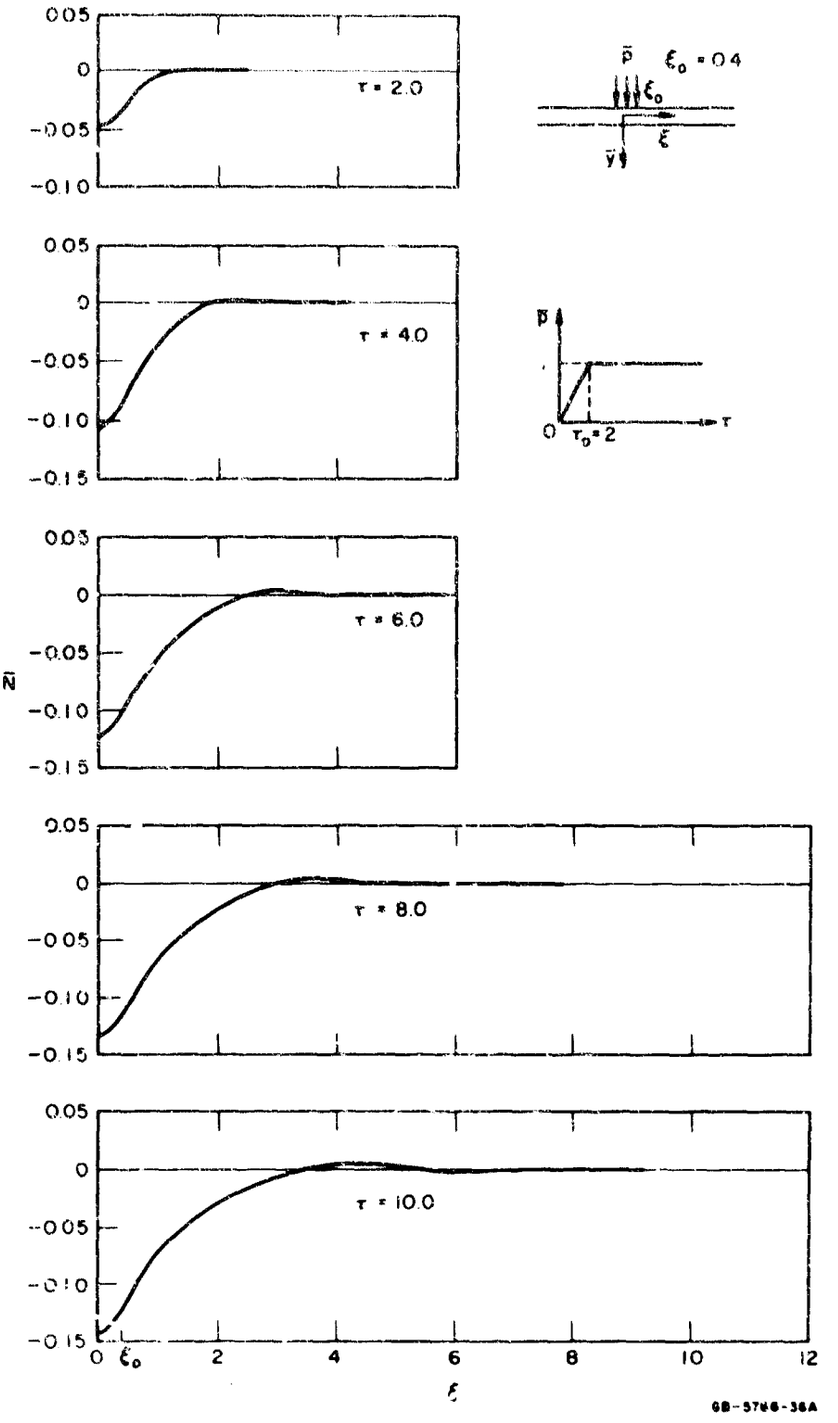

FIG. 47 DIMENSIONLESS CIRCUMFERENTIAL BENDING MOMENT OF PLATE

7. DISCUSSION AND CONCLUSIONS

This section is a discussion of the main results of the experiments of Section 4; wherever possible, results are compared qualitatively with the theoretical predictions of Section 6. Conclusions are presented which appear most reasonable at this stage of the investigation.

A. 0.458 Caliber AP Bullet Impacting Ceramic Tile

At an impact velocity of 1800 ft/sec and steel and ceramic hardness values of 700 K_{100} and 2000 K_{100}, the nose of the bullet shatters immediately. The elastic model predicts a sudden impact stress of over 100 kbar. Except for the shattered nose, the bullet appears to penetrate the tile while remaining in one piece, yet it is always recovered in a sand trap in several pieces (see Fig. 10). Hence, upon impact the bullet does fracture into several pieces but they stay together while penetrating the tile. In an oblique impact there should be some angle between the bullet trajectory and the normal to the tile above which the bullet pieces separate appreciably before the main penetration. This separation, causing a spreading of the load, would enhance armor strength.

In contrast to the behavior just described, a similar bullet striking at 1800 ft/sec a block of glass with a hardness value of 600 K_{100} remains intact.

From rear surface observations (Fig. 9) initial tile break-up appears as a set of 10 to 12 straight, equally spaced cracks radiating from a point immediately opposite the impact point and a circular crack with a diameter about four times that of the bullet or five to six times the tile thickness. In later break-up, the bullet pushes through the fractured material within this circle and some radial and circumferential cracking occurs outside this circle.

Elasticity theory predicts the development of a stress environment conducive to just the kind of fracture behavior observed. (This is discussed in the next section.)

B. 0.458 Caliber AP Bullet Impacting Ceramic-Fiber Glass Composite

The fiber glass backing plate acts mainly as a strong membrane while it contains the central fractured ceramic and the bullet (Fig. 11). The effectiveness of the backing plate depends greatly on the shear resistance at the bond layer and at the adjacent layer of weaving. During severe deformation the sample size could affect the membrane action of the fiber glass because, as separation from the ceramic occurs, the effective membrane size increases until its edge reaches that of the sample. Also, this size effect is probably influenced by the method of supporting the sample.

Terminal observations of the central damaged portion of the ceramic facing plate (Fig. 12) reveal a regular structure of radial cracks, spaced approximately 15^{o} apart at the bottom and 36^{o} at the top. Outside a 1-inch-diameter circle the ceramic at the top surface either remained in place or broke away in large pieces. Inside, the tiers of cracking generally resulted in facets sloping upwards towards the impact area at the top. Most of the central material was removed as powder. The fracture pattern just described is similar to those obtained in glass plates after impacts at low velocities; it is believed that the mechanisms are basically the same. According to the linear elasticity theory the stress environments are similar.

Many features of the fracture pattern correspond to the predictions based on the stress environments calculated from elasticity theory. These predictions include:

1. A rapid build-up of a tensile stress field (Figs. 41 through 44), with at least two components of principal stress in tension; this field creates an environment conducive to fine cracking and, near the impact zone, comminution.

2. Orientations of the principal planes in agreement with observed fracture surfaces (Figs. 42 and 44).

3. Extremely high tensile hoop and radial stresses at the surface opposite to the impact zone, which are conducive to a high density of radial and circumferential cracking.

4. Relatively low tensile hoop stresses at the impact surface away from the impact zone, which are conducive to less extensive radial cracking than at the opposite surface (Fig. 43).

C. 0.458 Caliber AP Bullet Impacting a Glass Block

For an impact velocity of 1800 ft/sec a hemispherical fracture field is formed, expanding at about 0.3 times the glass dilatational velocity (Figs. 15 and 16). As predicted by elasticity theory, the tensile stress environment of Figs. 37 through 40 corresponds quite well to the fracture field. Quantitative prediction of stress-wave fields is not yet possible because of the lack of experimental data on dynamic fracture stresses and fracture formation times.

A reflected fracture field forms which coalesces with the hemispherical incident field. After coalescence of the fields the bullet experiences little further resistance, because it is then traveling through finely fractured glass. (In fact, in penetrating the glass block the bullet velocity is reduced by only 20%.)

The bullet with a hardness of 700 K_{100} does not break up upon striking a glass block of hardness 600 K_{100}.

D. 0.458 Caliber Standard Ball-Nosed Bullet Impacting a Glass Block

For an impact of 1500 ft/sec the fracture field is formed of two parts, a quarter sphere centered at the impact point and expanding into the glass, and a central disk increasing in thickness and radius. The quarter sphere expands at about 0.3 times the dilatational velocity for the glass. The disk portion is caused by the relatively soft bullet splashing into the glass.

A reflected fracture field forms which coalesces with the quarter sphere incident field.

Unlike the AP bullet, the ball-nosed bullet does not penetrate the glass even though the entire block is fractured. Instead, the bullet flows plastically into a disk-like shape. (See Fig. 6 for construction of ball-nosed bullet.)

E. 0.3 Caliber Standard AP Bullet Impacting a Ceramic Tile

For a standard 0.3 caliber AP bullet impacting a ceramic tile at 2400 ft/sec, the conclusions of Section 7A apply qualitatively. The break-up of the facing plate and bullet is similar enough in behavior to the break-up in the corresponding experiments with 0.458 caliber AP bullets that it is justifiable to use a hard steel projectile for a fundamental study of interaction mechanics involving military bullets. A further improvement would be to use a hard steel projectile with the same diameter as the core of a military AP bullet, in this case 0.25 inch.

F. 0.3 Caliber Standard AP Bullet Impacting Ceramic-Fiber Glass Composite

For a standard 0.3 caliber AP bullet impacting a ceramic-fiber glass composite at 2400 ft/sec, the conclusions of Section 7B apply qualitatively. As noted in Section 7E, this agreement means that it is justifiable to use a hard steel projectile instead of a standard military AP bullet in the fundamental study of interaction mechanics.

G. 0.3 Caliber Standard AP Bullet Impacting a Glass Block

For a standard 0.3 caliber AP bullet impacting a glass block at 2400 ft/sec, the conclusions of Section 7C apply qualitatively. This means that the fracture fields in the glass block are not significantly affected by the soft jacket of the military AP bullet.

H. 0.5-Inch-Diameter Spall Piece Impacting Glass Block

For an impact velocity of 94 ft/sec a conoidal fracture surface forms in the glass (Figs. 31 and 32) with a front moving at about 0.3 times the dilatational velocity. The conoid originates at the edge of the impact circle, a region of high stress concentration, and its generators follow the principal planes as far as they are shown in Figs. 38 or 40. More theoretical results are required to explain the entire behavior. In particular, diagrams of the kind shown in Figs. 37 through 40 are required for much longer times.

I. 0.5-Inch-Diameter Spall Piece Impacting Glass-Micarta Composite

For an impact velocity of 54 ft/sec vertical radial cracks form below the impact point and each crack propagates at its own variable radial velocity (Fig. 23). Cracks which run ahead relieve the circumferential bending moments on either side, thus retarding or preventing the propagation of adjacent cracks. Hence only a few of the radial cracks actually propagate far from the impact point (Fig. 24). Usually, one circular crack forms with the impact point at its center, indicating little influence from the plate boundaries. This circular crack is predicted by the plate theory (Fig. 46).

Other cracks, in the form of circular arcs, form outside of the complete circular crack but are affected by the location of plate boundaries and probably by the method of supporting the plate; plate or sector modes or vibration probably come into play.

By comparison with glass-foam specimens, the Micarta backing plate makes little difference to the final crack pattern. Studies of impact response of beams supported on elastic foundations show that the foundations have to be extremely stiff before early-time fracturing moments are significantly reduced.

The crushing, radial fracturing, and formation of axisymmetric fracture surfaces in the impact region of the glass bear a strong resemblance to the central fracture pattern in the ceramic.

J. 0.5-Inch-Diameter Spall Piece Impacting Glass Plate

The main conclusions here are those described in Section 7I, because the fracture pattern is essentially the same whether the glass plate is bonded to Micarta or supported by a light foam.

K. General Conclusions and Remarks

The following general conclusions seem reasonable at the present stage of the investigation.

1. High speed photography can be used effectively to gain an understanding of the interaction of projectiles and composite armor.

2. A theoretical model based on the theory of elasticity predicts stress fields which create an environment compatible with the fracture patterns observed in the ceramic facing. The salient points of qualitative agreement are:

   a. A rapid build-up of tensile stress field (Figs. 41 through 44), with at least two of the three components of principal stress in tension; this field is conducive to fine cracking and, in the neighborhood of the impact zone, comminution (Figs. 7 and 8).

   b. Orientations of the principal planes, on which the maximum tensile stresses act, correspond to observed fracture surfaces (Figs. 42 and 44).

   c. Extremely high tensile hoop and radial stresses at the surface opposite to the impact zone, which are conducive to high density radial and circumferential cracking there (Figs. 9, 12, 22, and 26).

   d. Relatively low tensile hoop stresses at the impact surface away from the impact zone, which are conducive to less extensive radial cracking than at the opposite surface (Figs. 12, 13, 26, 41, and 43).

   e. Initial shattering of the projectile due to the extremely high impact stresses and an adjacent projectile free surface.

3. The geometry of the incident and reflected fracture fields in a glass block corresponds qualitatively to the tensile stress fields of elasticity theory (Figs. 15-17, 28, 29, 37-40).

4. Final fracture patterns in glass plates after low velocity impacts are similar to final fracture patterns in ceramic plates after high velocity impacts (Figs. 12-14 and 34).

5. The structural response predicted by the bending theory of plates (Figs. 45-47) is in qualitative agreement away from the impact zone. Vertical radial cracks propagate on the underside of the plate (Fig. 23) from the point opposite to the impact zone. Also, a circular crack forms which is several plate thicknesses in diameter (Fig. 34).

6. Use of hard steel projectiles instead of standard military projectiles is satisfactory for a basic study of projectile/armor interaction.

7. From experimental observations (Fig. 11), the flexible back-up plate behaves predominantly like a membrane restraining the broken-up ceramic and the bullet fragments.

Some remarks are appropriate concerning future quantitative correlation of theoretical predictions and experimental observations. Proceeding with the approach of the present investigation, the research topics that should be treated include:

1. Dynamic properties of materials. Some exploratory experiments for aluminum oxide are covered in Section 8, and one finding of the work is that ceramic is extremely sensitive to strain rate, gaining strength as the rate increases.

2. Interaction of stress fields due to cracking with the stress field environment.

3. Extension of equations of elasticity to include new properties.

4. Analysis of the stability and convergence of the finite-difference method.

8. DYNAMIC YIELDING OF ALUMINUM OXIDE

A. Introduction

In the previous section it was concluded that experimental observations on the ceramic facing plates are described qualitatively by a mathematical model based on elasticity theory. Because of the lack of experimental data on the mechanical properties of aluminum oxide under the large stresses and at the high strain rates associated with projectile-armor impact, the exploratory shock-wave experiments described here were carried out. The results of these experiments are presented in the form of a dynamic yield stress and a Hugoniot curve. This information serves to point out the strengths and weakenesses of the mathematical model of Section 5 and assists in pointing the way toward future refinements. The main conclusion drawn from the few experiments conducted is that the dynamic yield stress at strain rates of about 10^5 per sec is about 78 kbar, with a maximum shear stress of about 39 kbar. These values are many times the static yield or fracture stress of 3 kbar and thus extend considerably the usefulness of the elastic model.

A form of aluminum oxide called Lucalox* was chosen for its high purity, low porosity, and exceptional homogeneity. Another factor in this choice is that the elastic moduli under hydrostatic pressure up to 4 kbar (58,000 lb/in^2) for this material have been measured with ultrasonic techniques [4,5].

The experimental method is described in detail below; it consists essentially of sending a plane shock wave through one flat face of a thin slab of aluminum oxide and measuring the shock velocity in the slab and the velocity of the opposite free surface of the slab when the shock wave arrives. Before entering the ceramic, the shock wave is sent through an

*Manufactured by General Electric Co., Lucalox Ceramic Division, Nela Park 639, Cleveland, Ohio 44112.

aluminum plate and the velocity of the exposed free surface is measured. From these three measurements the required physical quantities, the stress and density immediately behind the shock front, are calculated. Each pair of values so obtained gives one data point in the stress-density or stress-specific volume plane. A curve fitted through several such data points gives the constitutive relation or Hugoniot curve. From this Hugoniot, the Hugoniot elastic limit and hence the dynamic yield stress are determined. In view of the planar geometry of the experiment, the dynamic yield stress is found under the condition of one-dimensional compression, or in other words, uniaxial strain. By using explosives to generate the plane shock waves, stresses of over 350 kbar are produced in the ceramic specimen; this stress level is well above the impact stresses of about 300 kbar currently encountered in impacts of hard steel projectiles and ceramic armor.

B. Shock Wave Theory

In this section the shock wave theory pertinent to the experiments is outlined. As mentioned above, the curve through stress-specific volume data points is the Hugoniot. This curve is the locus of states a material may achieve by a shock transition; each state is defined by the stress σ normal to the shock front, the volume V per unit mass (or the density $\rho = 1/V$), and by e, the internal energy per unit mass.

In Fig. 48, ABCD represents a Hugoniot curve in the plane of σ and V/V_o, where V_o is the specific volume when the material is free of stress. The curve in Fig. 48 anticipates the results for Lucalox, but the general shape is typical of many materials. AB is the elastic range of the Hugoniot and BD is the deformational (post-elastic) range; the stress σ_e at B is called the Hugoniot elastic limit. For shock stresses at or below σ_e, the shock process is closely approximated by a finite one-dimensional adiabatic compression, with shock velocities closely approximated by the zero-pressure longitudinal elastic wave velocity (dilatational velocity). The point C is the intersection of the deformation portion of the Hugoniot with the projection of the straight line AB, the elastic portion. States with stresses between σ_e and σ_c, such as

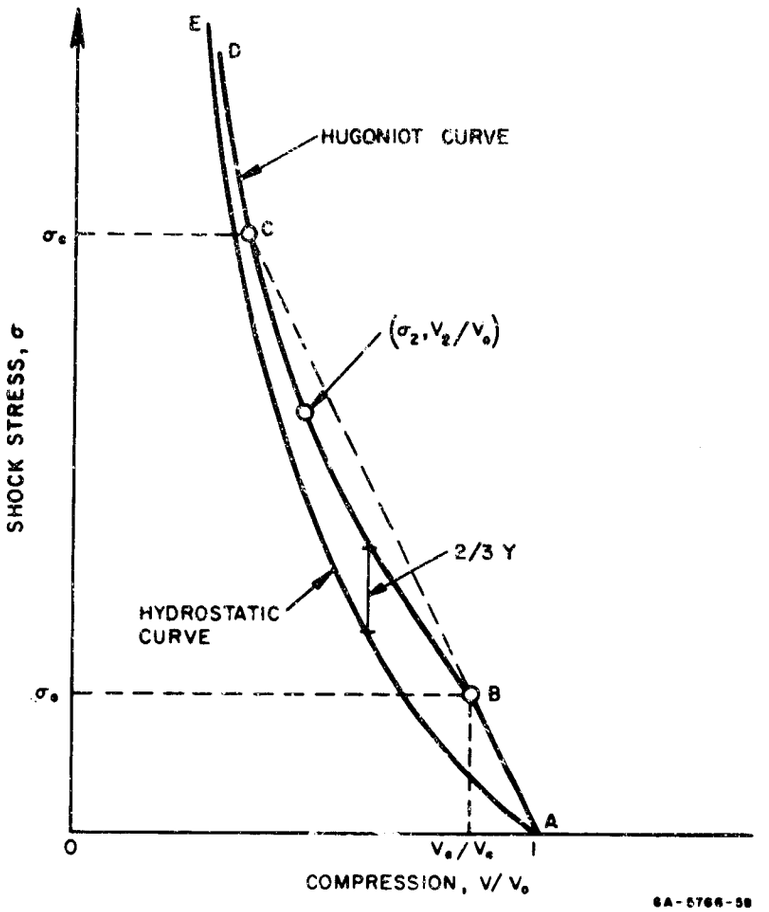

FIG. 48 HUGONIOT AND HYDROSTATIC CURVES
(elastic portion AB, deformational portion BCD)

state $(\sigma_2, V_2/V_o)$, are achieved experimentally through a double shock process in which an elastic shock bringing the material from the ambient state to state $(\sigma_e, V_e/V_o)$ precedes a second shock which transforms the material further to the state $(\sigma_2, V_2/V_o)$. This occurs in the Lucalox experiments. For shock stresses equal to or greater than σ_c, only a deformational shock forms in the material.

The Hugoniot elastic limit represents the maximum normal stress that the material can withstand under one-dimensional compression without permanent internal rearrangement, such as plastic flow or brittle fracture,

taking place at the shock front. Thus the deformational portion of the Hugoniot represents states in which internal rearrangement occurs. In Fig. 48, the Hugoniot curve can be seen in relation to the hydrostatic curve.

Consider a plane shock wave traveling at a velocity U (Fig. 49) in a material with an initial particle velocity, stress, and density state (u_o, σ_o, ρ_o). In traversing the material, the shock transforms the state to (u_1, σ_1, ρ_1). Conservation of mass and momentum across the shock front requires

$$\rho_o(U - u_o) = \rho_1(U - u_1) \tag{16}$$

$$\sigma_1 - \sigma_o = \rho_1(U - u_1)(u_1 - u_o) \tag{17}$$

Thus, from the state (u_o, σ_o, ρ_o) immediately before the shock arrives, the shock velocity U, and the particle velocity u_1 immediately after the shock has passed, the values of σ_1 and ρ_1 can be determined by the jump conditions (16) and (17), thereby providing a point on the Hugoniot curve.

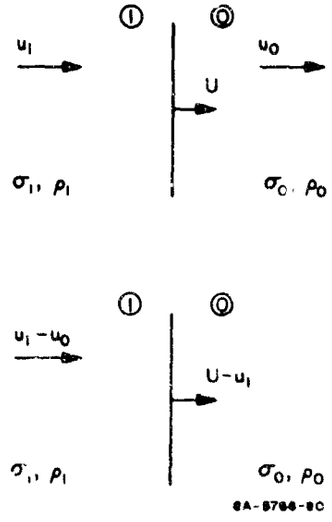

FIG. 49 STATES IN FRONT OF AND BEHIND SHOCK WAVE

In the experiments, the plane shock wave splits into two shock waves upon entering the ceramic specimen. The faster wave, the precursor, is an elastic wave of amplitude σ_1 moving into material of known density ρ_o and at rest and stress-free ($u_o = \rho_o = 0$). Hence from (16) and (17)

$$\sigma_1 = \rho_o u_1 U \qquad \rho_1 = \rho_o U/(U - u_1) \tag{18}$$

The shock velocity U is determined by measuring the transit time $t_1 - t_o$ and, for a ceramic thickness d, setting $U = d/(t_1 - t_o)$. The particle velocity u_1 is determined by recording the free-surface velocity u_{1fs} and assuming that $u_1 \approx 1/2\ u_{1fs}$. This approximation is an equality for an infinitesimal elastic wave, but if the gain in entropy produced by the elastic wave is small, as in the present case, the approximation is valid [6]. Substituting U and u_1 into (18) gives σ_1 and ρ_1 for one point on the Hugoniot.

The deformational wave following the elastic wave moves into ceramic material already shocked to the state (u_1, σ_1, ρ_1). Furthermore, upon reflection from the free surface of the ceramic specimen the precursor returns to meet the deformational wave, reflects off it, and again proceeds toward the free surface. Thus reverberations are set up and some simplifications are required to enable the unknowns to be readily determined.

Referring to Fig. 50, which shows the wave fronts in the distance-time (x-t) plane, let U_1, U_2, U_1', and U_2' be the velocities of the incident elastic wave, the incident deformation wave, the reflected elastic wave, and the deformational wave after collision with the reflected elastic wave. The effects of further reflections and dispersion of the reflected elastic wave are neglected. Then, from Fig. 50,

$$U_2 = (x_1' - x_o)/(t_1' - t_o) \qquad U_1' = (x_1 - x_1')/(t_1' - t_1)$$

$$U_2' = (x_2 - x_1')/(t_2 - t_1')$$

which, after eliminating x_1' and t_1', give for the deformation wave velocity,

$$U_2 = [U_1'(x_2 - x_o) + U_2'(x_1 - x_o) - U_1'U_2'(t_2 - t_1)]/[U_1'(t_1 - t_o) + U_2'(t_2 - t_o) - (x_2 - x_1)] \tag{19}$$

In (19), x_o, x_1, t_o, t_1, and t_2 are recorded, $x_1 - x_o$ being the specimen thickness d, and x_2 is calculated from $x_2 - x_1 = u_{1fs}(t_2 - t_1)$. The velocities U_1' and U_2' are assumed to be the same as the elastic velocity, so that

$$U_1' = U_1 - u_1 \qquad U_2' = U_1 + u_{1fs} = U_1 + 2u_1 \tag{20}$$

Thus, when U_1' and U_2' from (20) are substituted into (19), the deformational shock velocity U_2 is determined. In general, if U_1 and U_2 are of comparable magnitude the value of U_2 is not very sensitive to the particular assumptions employed to obtain U_1' and U_2'. Such is the case in the present experiments.

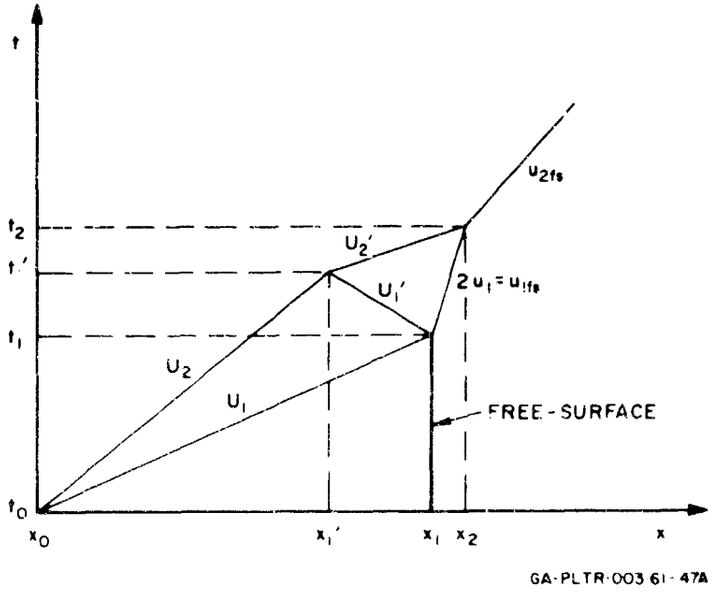

FIG. 50 SHOCK WAVE PATHS IN (x-t) PLANE

To preserve the notation of (16) and (17), let U be the deformational wave velocity instead of U_2 and let the states in front of and behind the shock front be denoted by subscripts 1 and 2. Then the required stress and density are

$$\sigma_2 = \sigma_1 + \rho_1(U - u_1)(u_2 - u_1) \qquad \rho_2 = \rho_1(U - u_1)/(U - u_2) \qquad (21)$$

With $U = U_2$ given by (19), the particle velocity u_2 is the remaining quantity to be found before σ_2 and ρ_2 can be determined by (21).

In the stress-particle velocity plane of Fig. 51, the known point A represents the state (u_1, σ_1) behind the incident elastic wave, and the as yet unknown point B represents the state (u_2, σ_2) behind the incident deformational wave. According to the first equation of (21), B lies on a straight line AC passing through A of known slope $\rho_1(U - u_1)$.

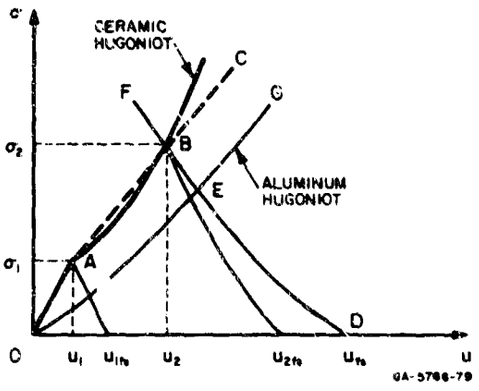

FIG. 51 STRESS-PARTICLE VELOCITY CURVES FOR FINDING STATE B

In the experiments, the plane shock wave generated by the explosive passes through a plate of 2024 aluminum, the "driver" plate, before entering the ceramic specimen. The free-surface velocity u_{fs} of the driver plate is recorded and fixes point D. The Hugoniot curve for 2024 aluminum is well established and, in the σ-u plane of Fig. 51, is represented by OG; the corresponding cross curve DF, assumed to be the reflection of OG, intersects OG at E. Curve DF is the locus of states that may exist at the driver plate-specimen interface when the driver plate is shocked initially to state E. The state that exists at the interface is the state behind the deformational wave represented by B. Hence B is the intersection of the cross-curve DEF and the straight line AC. With u_2 and σ_2 now determined, ρ_2 follows from (21), thereby providing a data point for

for the Hugoniot. Note that each specimen provides two data points, (σ_1, ρ_1) and (σ_2, ρ_2).

Fixing the x-axis of the Cartesian axes (x, y, z) perpendicular to the wave fronts, the stresses for uniaxial strain ($\epsilon_y = \epsilon_z = 0$) in the elastic regime AB of Fig. 48 are

$$\sigma_y = \sigma_z = [\nu/(1 - \nu)]\sigma_x \tag{22}$$

where ν is Poisson's ratio for aluminum oxide. Also, the maximum shear stress in the stress field of (22) is

$$\tau = (\sigma_x - \sigma_y)/2 = [(1 - 2\nu)/(1 - \nu)]\sigma_x/2 \tag{23}$$

The von Mises yield criterion may be expressed in the form

$$(\sigma_x + p)^2 + (\sigma_y + p)^2 + (\sigma_z + p)^2 = 2Y^2/3 \tag{24}$$

where $p = -(\sigma_x + \sigma_y + \sigma_z)/3$ is the "hydrostatic" pressure and Y is the yield stress. Using the stress relation (22), (24) reduces to

$$Y = [(1 - 2\nu)/(1 - \nu)]\sigma_x \tag{25}$$

From the experimental results, a Hugoniot curve of the form shown in Fig. 48 is determined, with a maximum elastic stress $\sigma_x = \sigma_e$ (at point B), the Hugoniot elastic limit. Setting $\sigma_x = \sigma_e$ in (25) and (23) gives the dynamic yield stress and maximum shear stress τ_{max} under a condition of one-dimensional compression. Considering the deformational portion of the Hugoniot curve as representing an elastic-plastic behavior, (24) gives

$$-\sigma_x = [illegible] 2Y/3 \tag{26}$$

Hence, the vertical offset of the deformational portion of the Hugoniot curve from the hydrostatic curve, as shown in Fig. 48, is 2Y/3. Numerical values from the experiments are presented later.

C. Description of Experiments

Figure 52 displays the essential features of the experimental setup. A plane wave generator, consisting of Baratol and Composition B-3 explosive, is initiated to send a plane detonation wave into an explosive pad of Composition B-3 or Baratol. Upon reaching a driver plate of 2024 aluminum this detonation wave produces a plane shock wave. The driver plate is used to produce a shock profile more flat-topped than that produced by explosives alone and to prevent explosive gases from interfering with the optical system. Aluminum 2024 was chosen because its equation of state is well established.

After traversing the driver plate, the shock wave enters a ceramic specimen having a smaller area than the driver plate. When the shock wave in the driver plate reaches the free surface of the aluminum outside the ceramic area, it impacts an inclined mirror mounted on the surface. Meanwhile the shock wave produced in the ceramic specimen splits to form an elastic and a deformational wave, denoted by S_1 and S_2 in Fig. 52. After traversing the ceramic, the waves S_1 and S_2 cause the free surface to impact an inclined mirror mounted on the free surface.

During these events light from an explosive-argon source reflects from the mirrors and through a slit onto the rotating mirror of a streak camera. The mirror rotates at a known rate (the writing rate) across a stationary arc of film. On the arrival of the shock waves at the inclined mirrors, an abrupt decrease in reflectivity occurs, causing a corresponding decrease in film exposure, as indicated in Fig. 52. Film records from three ceramic specimens labeled A, B, and C, and from one driver plate to which they were adhered, are shown in Fig. 53; the assembly from which these records were obtained is shown in Fig. 54. From the rate of impaction of the inclined mirrors, the free-surface velocities u_{fs} of the driver plate and the two free-surface velocities u_{1fs} and u_{2fs} of each specimen are calculated. If α is the angle of inclination of

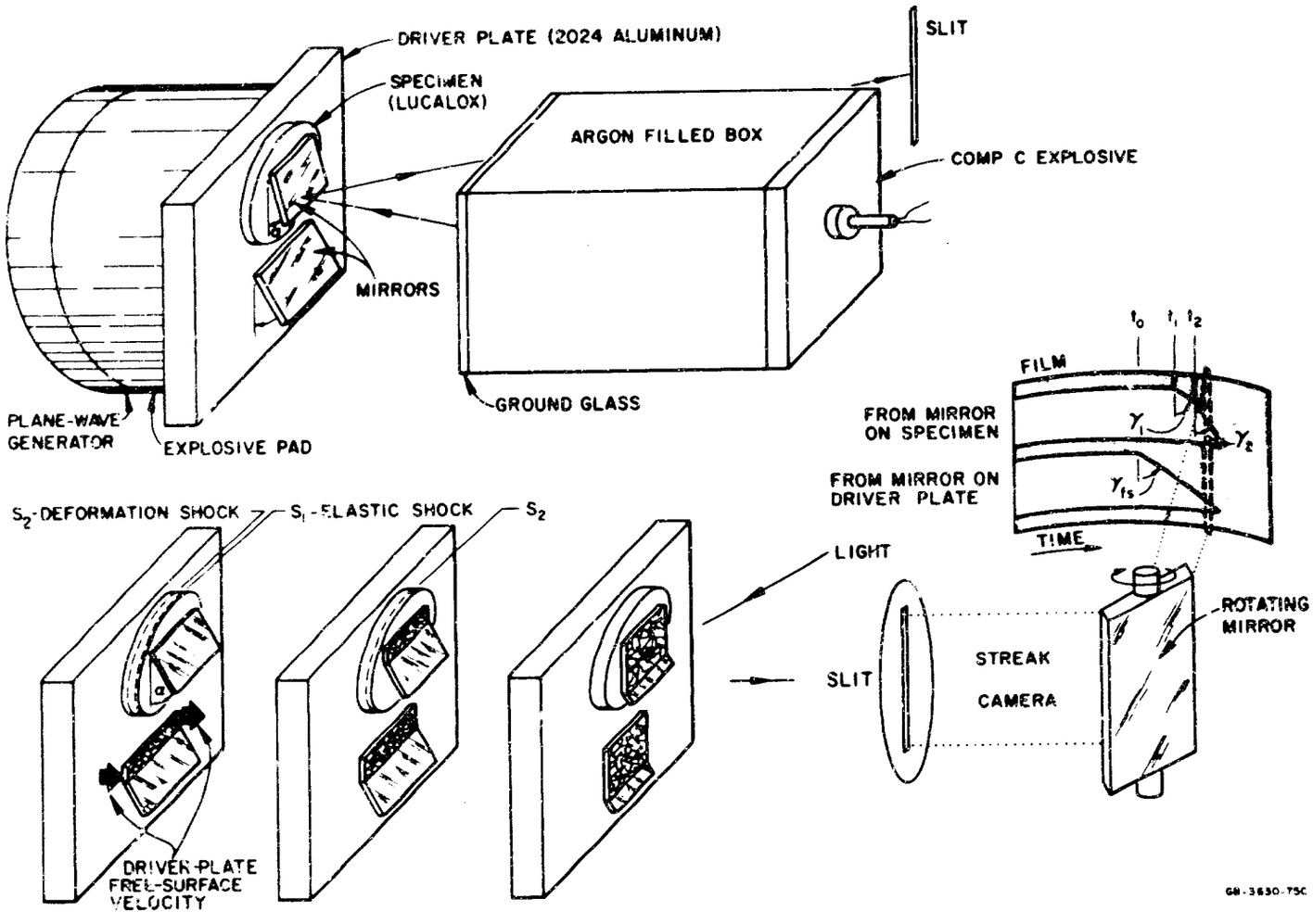

FIG. 52 DIAGRAMMATIC VIEW OF PLANE WAVE — INCLINED MIRROR EXPERIMENT

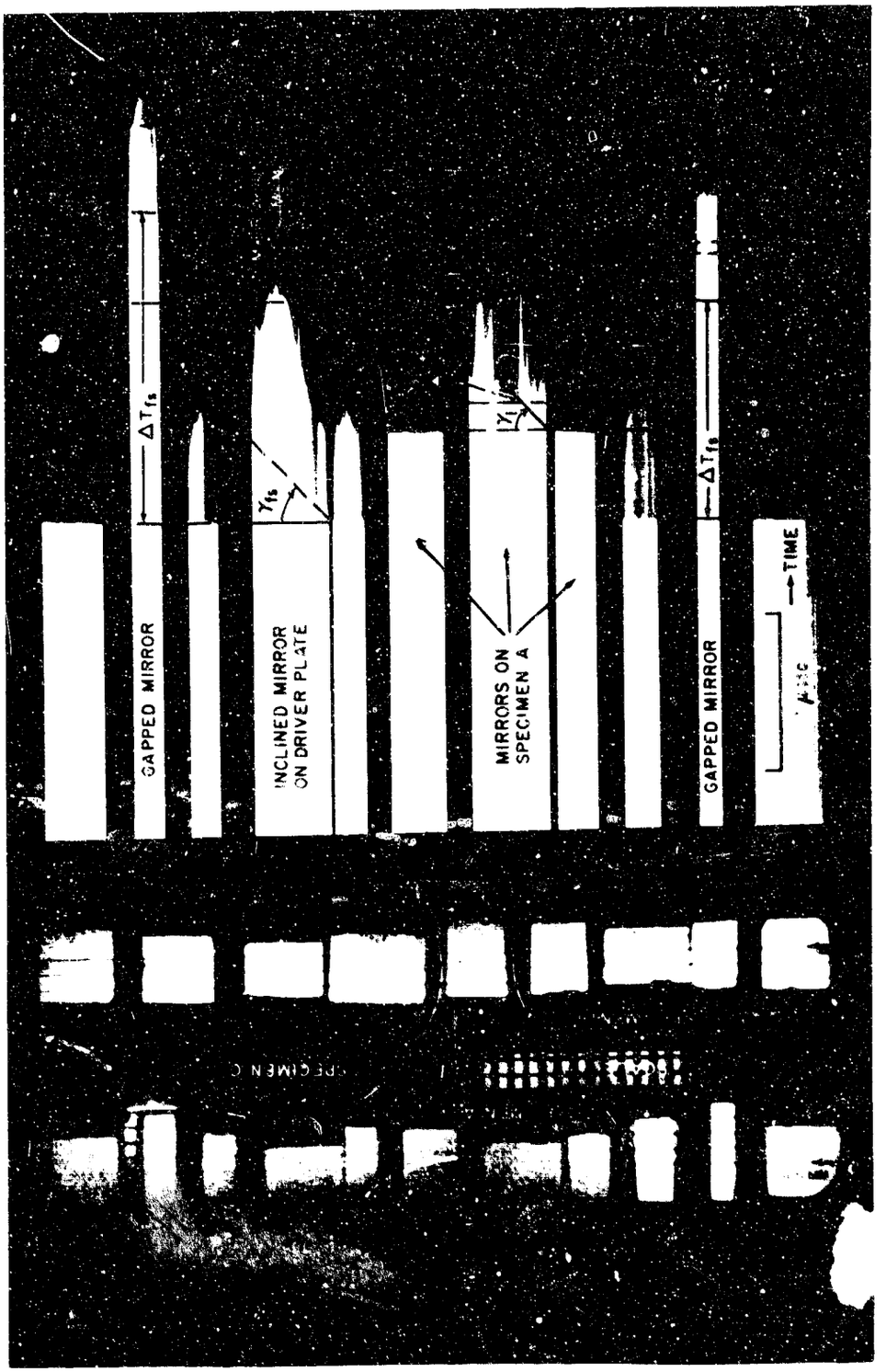

FIG. 53 STREAK CAMERA RECORDS FOR SHOT 12,136

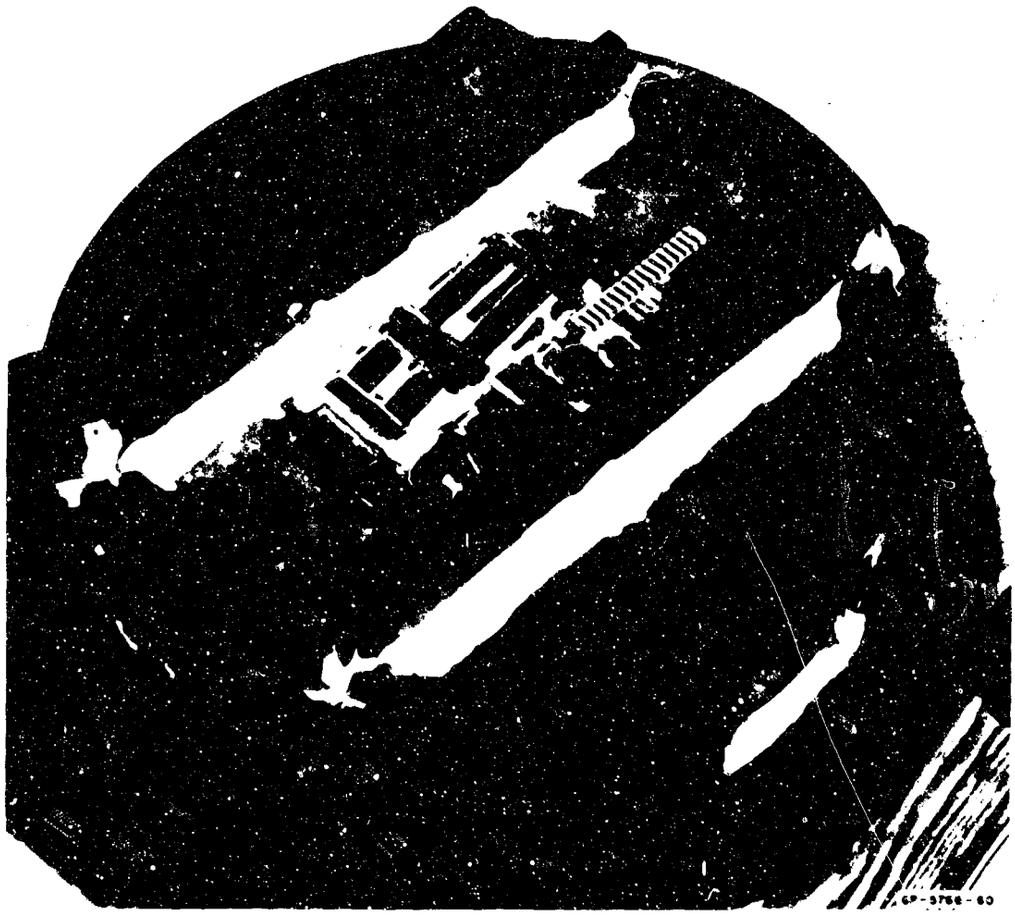

FIG. 54 EXPERIMENTAL ASSEMBLY

the mirrors to the free surfaces, the free-surface velocities are

$$u_{fs} = W \tan\alpha/M \tan\gamma_{fs}$$

$$u_{1fs} = W \tan\alpha/M \tan\gamma_{1}$$

$$u_{2fs} = W \tan\alpha/M \tan\gamma_{2}$$

where γ_{fs}, γ_1, and γ_2 are the light cutoff angles on the film (Figs. 52 and 53), and W and M are the streak camera writing rate and magnification. In practice, mirror corrections are required to account for deviations from ideal geometry, such as a small angle of obliquity of an incident shock. The times t_o, t_1, and t_2 at which sudden decreases in reflectivity occur permit the transit times, $t_1 - t_o$ and $t_2 - t_o$, of the waves S_1 and S_2 to be calculated. However, only the velocity U_1 of S_1 is immediately obtainable from $U_1 = d/(t_1 - t_o)$, where d is the specimen thickness. The velocity U_2 of S_2 has to be calculated using (19) and (20).

The Lucalox specimens were sawn from rods of 1- to 2-inch diameter to thicknesses ranging from 3 to 13 mm. They were ground flat and parallel to a tolerance of ±0.002 inch. In addition to inclined mirrors, flat mirrors were cemented to the free surfaces to provide precise records of wave arrival times (Fig. 53). Thin steel shims (0.004 or 0.006 inch thick) protected the inclined mirrors from a premature loss of reflectivity (believed due to small-scale jetting at the free surface) and eliminated air shocks produced by rapidly moving free surfaces.

D. Results and Conclusions

The Hugoniot data obtained from two shots involving a total of five specimens are presented in Table 2 and are plotted in relation to other available Hugoniot and hydrostatic data in Fig. 55. Uncertainties in measurements of the particle velocity u_1 just behind the elastic wave front are less than ±4%; the uncertainties for the deformation shock and particle velocities U_2 and u_2 are less than ±1 and ±3%, respectively.

In Fig. 55 it can be seen that the data agree with the data of McQueen and Marsh [7] at higher stresses for aluminum oxide in single crystalline (sapphire) and ceramic form.

Table 2

HUGONIOT DATA, LUCALOX[a] (Aluminum Oxide)

Shot[b] No.	Specimen Thickness (mm)	Driver Free Surface Velocity (mm/μsec)	First (Elastic) Shock State					Second (Deformational) Shock State					
			Shock Velocity U_1 (mm/μsec)	Particle Velocity u_1 (mm/μsec)	Shock Stress σ_1 (kbar)	Density ρ_1 (g/cm^3)	Volume V_1 (cm^3/g)	Apparent Velocity $\bar{U}_2$ (mm/μsec)	Shock Velocity U_2 (mm/μsec)	Free Surface Velocity u_{fs_2} (mm/μsec)	Shock Stress σ_2 (kbar)	Particle Velocity u_2 (mm/μsec)	Volume V_2 (cm^3 g)
12138	6.365	2.694	10.98	0.253	111	4.074	0.2455	9.719	9.604	1.67	369	0.93	0.2277
	12.687	2.694	10.88	0.228	99	4.065	0.2460	9.496	9.362	1.57	363	0.94	0.2268
12136	3.167	1.543	10.98	(0.368)[c]	(161)	4.118	0.2428	9.079	8.805	1.174	199	0.475	0.2398
	6.375	1.543	10.98	0.262	114	4.078	0.2452	9.039	8.798	0.944	195	0.495	0.2385
	12.705	1.543	10.90	0.284	123	4.086	0.2447	8.829	8.530	0.957	195	0.495	0.2385

[a] Initial density, $\rho_0 = 3.98$ g/cm^3.

[b] Explosive System: Shot 12138 - P80 (Plane Wave Lens) + 1-1/2" Comp B-3 + 3/4" 2024 Al.

Shot 12136 - P80 (Plane Wave Lens) + 2" Baratol + 1" 2024 Al.

[c] Less certain data.

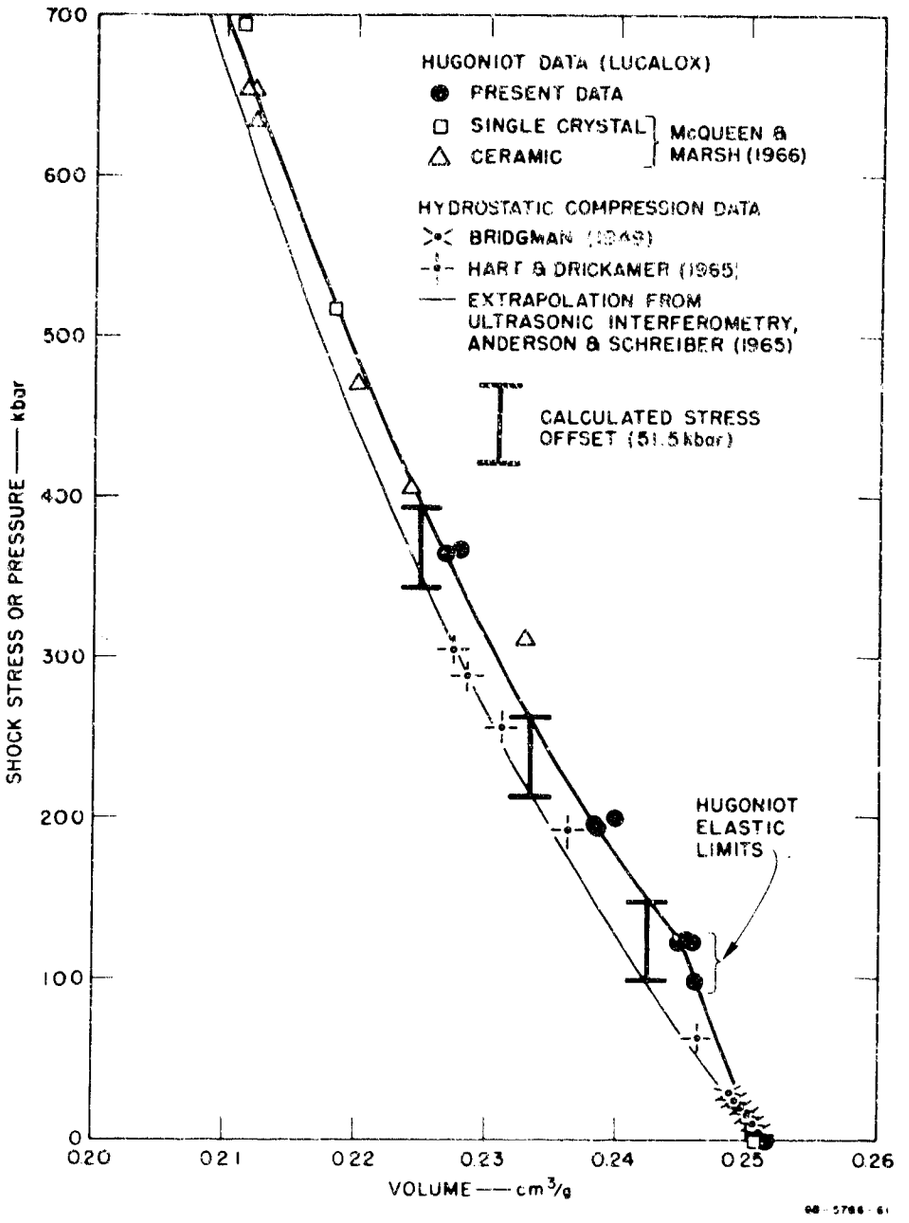

FIG. 55 HUGONIOT AND HYDROSTATIC DATA AND CURVES

The elastic shock velocities U_1 listed in Table 2 are in the range 10.88 and 10.98 mm/μsec and are within 1-1/2% of the elastic dilatational wave velocity of 10.845 mm/μsec measured by Anderson and Schreiber [4,5] for Lucalox.

In four of the five specimens the Hugoniot elastic limit σ_e is 112 ± 13 kbar. This is lower than the values obtained by Brook and Graham [8] for single crystal material (sapphire), which vary from 150 to 200 kbar, depending on the crystallographic orientation.

Using the value σ_e = 112 kbar and ν = 0.2363 for Poisson's ratio [4,5], relations (22), (23), (25), and (26) lead to the results σ_y = σ_z = 34.5 kbar for the stress components parallel to the wave front, τ_{max} = 38.8 kbar for the maximum shear stress, Y = 77.5 kbar for the dynamic yield stress, and 2Y/3 = 51.7 kbar for the offset of the Hugoniot curve from the hydrostatic curve.

The hydrostatic curve in Fig. 55 is a fit of existing data up to 4 kbar, from ultrasonic velocity measurements [4,5], by using a Murnaghan logarithmic equation [9]. The data points of Hart and Drickamer [10] with stress levels up to 300 kbar lie close to this curve. It can be seen that the stress offset value of 51.7 kbar calculated from the present experiments is in agreement with existing data.

Associated with the maximum shear stress and yield stress values of 38.8 and 77.5 kbar is a strain rate of approximately 2 x 10^5/sec, calculated by dividing the uniaxial strain (~ 0.02) at the Hugoniot elastic limit by the rise time of the elastic shock (~ 10^{-7} sec). In previous experiments with ceramics [3, 11, 12] at strain rates varying from 10^{-3} to 10^3/sec and in different geometries, the shear and yield stress values were at least an order of magnitude lower, thereby indicating great sensitivity of ceramic to strain rate (geometry is probably not such an important factor).

Although the value $\tau_{max} \approx 39$ kbar or $Y \approx 78$ kbar does not define a yield surface in σ_x, σ_y, σ_z space, it does represent a definite constraint on possible models for describing the yielding of aluminum oxide and indicates that the yield surface depends strongly on strain rate.

9. MICROSCOPIC EXAMINATION OF FRACTURED ALUMINUM OXIDE

It is of considerable interest to know the mode of fracture of ceramic armor. If the fractures in a given ceramic are primarily intergranular, improvement might be effected by a strength modification of the same basic ceramic material. For example, the tensile strength of magnesium oxide ceramic varies from about 11,000 lb/in^2 for a polycrystalline material of 99.7% crystal density with 50 micron grain size, to about 28,000 lb/in^2 for a fully dense polycrystalline material with 20 micron grain size. Single crystal MgO may have a tensile strength as high as 140,000 lb/in^2 [13]. If the fractures are primarily transgranular, improvement in performance would probably require a change in the basic ceramic composition. For example, boron carbide ceramics could be tried for a possible improvement over aluminum oxide ceramics in armor application.

The fracture surfaces of one aluminum oxide specimen (AD94) were examined by reflected light microscopy. For the most part the fracture surfaces were irregular, on a scale approximately the grain size. Only a few flat reflecting regions, about 20 microns in diameter, could be observed. Although these regions could have been transgranular fractures they accounted for only a small portion of the observed fracture surface. It is tentatively concluded that most of the fracture surface was intergranular, with only a few transgranular fractures of larger grains. Because of the high magnification (400x) necessary to resolve details of the fracture surface, the depth of focus of the microscope was too shallow to permit meaningful photographs. It would probably be preferable to use shadowed plastic replicas of the fracture surface in an electron microscopic study.

As another approach toward establishing the mode of fracture, petrographic thin sections of the fractured pieces were studied; these sections were about 30 microns thick. Inasmuch as it did not seem possible to reliably preserve edge detail, a search was made for internal closed fractures which could be studied. One such fracture was found (Fig. 56); it

FIG. 56 PHOTOMICROGRAPH OF CERAMIC (AD94) SHOWING FRACTURE

is irregular, on about the scale of the grain size (2 to 30 microns). Examination of this fracture in polarized light turned up no evidence of transgranular fracture. The grain size of the sample is somewhat small for study by normal petrographic techniques because, ideally, a section should be much thinner than the average grain diameter. An extension of this exploratory study could involve ultrathin sections prepared by special techniques.

REFERENCES

1. Wilkins, M. L., "Calculation of Elastic-Plastic Flow," Methods in Computational Physics, Vol. 3, Academic Press, New York, 1964, pp. 211-263.

2. Mindlin, R. D., "Influence of Rotary Inertia and Shear on Flexural Motions of Isotropic, Elastic Plates," J. Appl. Mech. 73, 31-38 (March 1951).

3. Sedlacek, R., "Tensile Strength of Brittle Materials," Stanford Research Institute Technical Report, Air Force Materials Laboratory, Research and Technology Division, Air Force Systems Command, Wright-Patterson Air Force Base, Ohio, AFML-TR-65-129, Contract AF 33(657)-10600, April 1965.

4. Anderson, O. L. and E. Schreiber, "Measurement of P and S Sound Velocities under Pressure on Laboratory Models of the Earth's Mantle," Lamont Geological Observatory, Columbia University, Final Report, Contract AF-AFOSR 49(638)-1355, December 16, 1965.

5. Schreiber, E. and O. L. Anderson, "The Pressure Derivatives of the Sound Velocities of Polycrystalline Alumina (Lucalox)," J. Am. Ceram. Soc. (in press).

6. Rice, M. H., R. G. McQueen, and J. M. Walsh, "Compression of Solids by Strong Shock Waves," Solid State Physics 6, ed. F. Seitz and D. Turnbull, Academic Press, New York, 1958, pp. 1-63.

7. McQueen, R. G. and H. M. Marsh, Handbook of Physical Constants, Rev. Ed., ed. S. P. Clark, Jr., Geological Soc. of America, New York, 1966.

8. Brook, W. P. and R. A. Graham, "Shock Wave Compression of Sapphire," Bull. Am. Phys. Soc. II, 11, 414 (1966).

9. Anderson, O. L., "Two Methods for Estimating Compression and Sound Velocity at Very High Pressures," Proc. Nat. Acad. Sci. 54, 667-673 (1965).

10. Hart, M. V. and H. G. Drickamer, "Effect of High Pressure on the Lattice Parameters of Al_2O_3," J. Chem. Phys. 43, 2265-2266 (1965).

11. Matheson, R. R., "G.E.'s Lamp Research Leads to Unique Ceramic Material," Ceramic Age, June 1963.

12. ITT Research Institute Technical Document Report No. ASD-TR-61-628, Part III, Air Force Materials Laboratory, June 1964.

13. Stokes, R. J., "Correlation of Mechanical Properties with Microstructure," Microstructure of Ceramic Materials, Nat. Bu. Standards Miscellaneous Publication No. 257.

2. Comminution and fine cracking of the ceramic facing material spreads from the impact zone due to an expanding hemispherical field of large tensile stresses; this field follows a compressive wave front and has a strong "hydrostatic" tensile behavior. Ceramic powder is ejected from the region around the bullet.

3. Cracking at the face opposite to the impact zone develops rapidly. This cracking is predominantly radial, because the expanding tensile stress field has large circumferential stress components leading other stress components.

4. Density of cracking decreases away from the impact zone, due to attenuation of the tensile stress field.

5. A membrane, or stretching action of the flexible backing plate restrains the central region of crushed ceramic and fragmented projectile.

General conclusions at this stage of the investigation are:

1. High speed photography can be used effectively to gain a qualitative understanding of the interaction of projectiles and composite armor.

2. Theoretical models based entirely on elastic response predict stress and bending moment distributions compatible with the fracture patterns observed in ceramic facing plates.

3. Aluminum oxide has a fracture stress which increases significantly with rate of strain and the material behaves elastically at stresses below the fracture stress.

Future research should provide for the determination of dynamic mechanical properties of ceramics and incorporation of these properties into a theoretical model. This information is needed because of the high sensitivity of the fracture stress to strain rate. Future research should also include a study of the interaction of the stress fields caused by fracture with the environmental stress fields. This interaction, not taken into account in the present work, may be significant.

UNCLASSIFIED

Security Classification

DOCUMENT CONTROL DATA · R&D

(Security classification of title, body of abstract and indexing annotation must be entered when the overall report is classified)

1 ORIGINATING ACTIVITY (Corporate author)	2a REPORT SECURITY CLASSIFICATION
Stanford Research Institute Menlo Park, California 94025	Unclassified
	2b GROUP

3 REPORT TITLE

INTERACTION OF PROJECTILES AND COMPOSITE ARMOR

4 DESCRIPTIVE NOTES *(Type of report and inclusive dates)*

Final Report, November 15, 1965 - January 15, 1967

5 AUTHOR(S) *(Last name, first name, initial)*

Florence, A. L. and Ahrens, T. J.

6 REPORT DATE	7a TOTAL NO OF PAGES	7b NO OF REFS
January 31, 1967	138	13

8a CONTRACT OR GRANT NO	9a ORIGINATOR'S REPORT NUMBER(S)
DA-04-200-AMC-1381(X) b PROJECT NO D/A 1C024401A110 c AMCS Code 5011-11-855 d	AMRA CR 67-05(F) 9b OTHER REPORT NO(S) *(Any other numbers that may be assigned this report)*

10 AVAILABILITY/LIMITATION NOTICES

Distribution of this document is unlimited

11 SUPPLEMENTARY NOTES	12 SPONSORING MILITARY ACTIVITY
	U.S. Army Materials Research Agency Watertown, Massachusetts 02172

13 ABSTRACT

~~This~~ report describes basic experimental and theoretical work on the interaction of projectiles and lightweight composite armor. The armor of interest consists of a very hard and inflexible facing plate (ceramic) bonded to a flexible backing plate (fiber glass). Attention has been focused on the mechanism of interaction between a facing plate and a hard projectile (steel).

Experimental results consist of high speed camera photographs of the projectile-armor interaction and observations of the final state of the projectile and armor. Theoretical analyses, based on the theory of elasticity, were used to establish stress fields in the facing plate during the initial stages of impact and to determine deflections and bending moments during the later stages. In addition to this work on the mechanics of projectile-armor interaction, exploratory experiments were undertaken with a view toward establishing the dynamic mechanical properties of aluminum oxide, an important facing material.

On the basis of these experimental observations and theoretical predictions, the following sequence of events occurs when a hard steel projectile strikes composite armor having a ceramic facing plate:

1. The tip of the projectile is shattered into many very small (1 mm) fragments. This occurs because, due to the proximity of the steel free surface, tensile stresses greatly exceeding the fracture stress are immediately set up at the tip. The remainder of the steel projectile fractures into a few pieces (the largest being the rear portion) which remain together during penetration of the facing plate.

DD FORM 1473

UNCLASSIFIED

Security Classification